Vapour-Deposited Hybrid Metal-Halide Perovskite Thin Films for Photovoltaic Applications



Jay B. Patel

Lincoln College

University of Oxford

A thesis submitted for the degree of

Doctor of Philosophy

Trinity 2018

Abstract

Hybrid metal-halide perovskite semiconductors have recently shown to be excellent photoabsorbers for photovoltaic devices. There are a variety of techniques that can be used to fabricate hybrid metal-halide thin films, from facile low

temperature solution processing methods to vapour deposition methods. Physical vapour deposition, in particular thermal evaporation, is one such technique, which is easily up-scalable and widely used in industry. Additionally, vapour deposition is a solvent-free technique that yields smooth, uniform and pin-hole free thin films.

This thesis reports an investigation of hybrid metal-halide perovskite, $CH_3NH_3PbI_3$ ($MAPbI_3$) thin films, and their subsequent implementation in photovoltaic devices. The initial investigation follows the formation dynamics of the $MAPbI_3$ thin films from sequentially depositing the precursors, PbI_2 and CH_3NH_3I (MAI), whilst keeping the substrates at 273 K. Upon heating the substrates to room temperature, the MAI diffused into the PbI_2. The diffusion is tracked using Fourier transform infrared spectroscopy (FTIR) and x-ray crystal diffraction analysis. The results show that exposing the films to moist air facilitates the diffusion and aids in creating a crystalline perovskite thin film.

Dual-source vapour deposition is a technique whereupon both the precursors are evaporated at the same time, yielding a perovskite thin film immediately. An investigation on how different substrates influence the perovskite thin film, was carried out. It is found that perovskite growth on TiO_2 induces regions of amorphous perovskite at the interface. The presence of amorphous perovskite explains why photovoltaic devices which have a TiO_2/$MAPbI_3$ interface show current-voltage hysteresis. However, incorporating a layer of continuous fullerene thin film on the substrate leads to the formation of crystalline perovskite at the interface, and the corresponding photovoltaic devices show no hysteresis.

$MAPbI_3$ photovoltaic devices were carefully investigated at low-temperatures (15 K – 350 K) using Fourier transform photocurrent spectroscopy (FTPS). The photocurrent spectra of $MAPbI_3$ devices showed that the excess PbI_2 usually found in $MAPbI_3$ thin films contributes to the photocurrent. Furthermore, a lower limit of the exciton binding energy of 9.1 meV was extracted for $MAPbI_3$ by comparing the low temperature absorption spectra with the photocurrent spectra.

Finally, organic bulk heterojunction photovoltaic devices were investigated. The effect of UV light on the devices for 18 hours was carefully tracked using FTPS. Initially, the results show a decrease in external quantum efficiency (EQE) at high photon energies. A closer look at the EQE spectra reveal a change in the sub-band gap absorption, indicative of a change in the micromorphology of the bulk heterojunction. These findings indicate the need to find non-fullerene acceptors.

List of publications

Formation Dynamics of $CH_3NH_3PbI_3$ Perovskite Following Two-Step Layer Deposition

J. B. Patel, R. L. Milot, A. D. Wright, L. M. Herz, M. B. Johnston

J. Phys. Chem. Lett., 2016, 7 (1), pp 96–102

Influence of Interface Morphology on Hysteresis in Vapor-Deposited Perovskite Solar Cells

J. B. Patel, J. Wong-Leung, S. Van Reenen, N. Sakai, J. Tse W Wang, E. S. Parrott, M. Liu, H. J. Snaith, L. M. Herz, M. B. Johnston

Adv. Electron. Mater. 2017, 3, 1600470.

Photocurrent Spectroscopy of Perovskite Solar Cells over a Wide Temperature Range from 15 to 350 K

J. B. Patel, Q. Lin, O. Zadvorna, C. L. Davies, L. M. Herz, M. B. Johnston

J. Phys. Chem. Lett., 2018, 9 (1), pp 263–268

The Effect of Ultraviolet Radiation on Organic Photovoltaic Devices

J. B. Patel, P. Tiwana, N. Seidler, G. E. Morse, O. R. Lozman M. B. Johnston, L. M. Herz

ACS Appl. Mater. Interfaces 2019 (11) pp 21543-21551

Conference proceedings

21st Merck CASE Conference *2015*	***Oral***
22nd Merck CASE Conference *2016*	***Oral***
International Conference on Hybrid and Organic Photovoltaics (HOPV) *2016*	***Poster***
23rd Merck CASE Conference *2017*	***Oral***
International Conference on Perovskite Solar Cells and Optoelectronics (PSCO) *2017*	***Poster***
Asia & Pacific Hybrid Organic Photovoltaic Conference (AP-HOPV) *2018*	***Oral***
Materials Research Society Spring Meeting (MRS) *2018*	***Oral***

List of Collaborative Publications

Photon Re-Absorption Masks Intrinsic Bimolecular Charge-Carrier Recombination in $CH_3NH_3PbI_3$ Perovskite properties
T Crothers, RL Milot, **JB Patel**, E Parrott, J Schlipf, P Muller-Buschbaum, MB Johnston, LM Herz
Nano Lett., 2017, 17 (9), pp 5782–5789

Photovoltaic Mixed-Cation Lead Mixed-Halide Perovskites: Links Between Crystallinity, Photo-Stability and Electronic Properties
W Rehman, DP McMeekin, **JB Patel**, RL Milot, MB Johnston, HJ Snaith, LM Herz
Energy Environ. Sci., 2017, 10, 361-369

Bimolecular Recombination in Methylammonium Lead Triiodide Perovskite Is An Inverse Absorption Process
CL Davies, MR Filip, **JB Patel**, TW. Crothers, C Verdi, AD Wright, RL Milot, F Giustino, MB Johnston LM Herz
Nat Comms 2018 9, 293

Highly Crystalline Methylammonium Lead Tribromide Perovskite Films for Efficient Photovoltaic Devices
NK Noel, B Wenger, SN Habisreutinger, **JB Patel**, T Crothers, Z Wang, RJ Nicholas, MB Johnston, LM Herz, HJ Snaith
ACS Energy Letters 2018, 3 (6), 1233-1240

Near-Infrared and Short-Wavelength Infrared Photodiodes Based on Dye–Perovskite Composites
Q Lin, Z Wang, M Young, **JB Patel**, RL Milot, L. Martinez Maestro, RR Lunt, HJ Snaith, MB Johnston, LM Herz,
Adv. Funct. Mater. 2017 27 1702485.

Vibrational Properties of the Organic–Inorganic Halide Perovskite $CH_3NH_3PbI_3$ From Theory and Experiment: Factor Group Analysis, First-Principles Calculations, and Low-Temperature Infrared Spectra
MA Pérez-Osorio, RL Milot, MR Filip, **JB Patel**, LM Herz, MB Johnston, F Giustino
J. Phys. Chem. C 2015 119 (46), 25703-25718

Perovskite-Perovskite Tandem Photovoltaics with Optimized Band Gaps
GE Eperon, T Leijtens, KA Bush, R Prasanna, T Green, J Wang, DP McMeekin, G Volonakis, RL Milot, R May, A Palmstrom, DJ Slotcavage, RA Belisle, **JB Patel**, ES Parrott, RJ Sutton, W Ma, F Moghadam, B Conings, A Babayigit, H Boyen, S Bent, F Giustino, LM Herz, MB Johnston, MD McGehee, HJ Snaith
Science, 2016, 354 (6314) 861-865

Acknowledgements

I would like to thank my supervisor, Professor Laura Herz, for her mentoring, endless encouragement and giving me investigative freedom to pursue a variety of projects. I would equally like to thank Professor Michael Johnston, for enthusiastically letting me be part of his various scientific projects, including designing new experimental equipment and expanding current techniques. I would also like to thank Professor Henry Snaith, for his fruitful discussions and enthusiastically promoting collaborative science. I am thankful for the support from my industrial supervisor Dr Priti Tiwana, throughout my DPhil. I would like to express my thanks to Professor Jenny Wong-Leung, for her help with high resolution microscopy and critical analysis of it. I am very grateful for the funding provided by EPSRC UK and the Merck Group. I have had the privilege of having the support of many talented humans throughout this DPhil and therefore would like to thank:

Herz Group and Johnston Group and in Particular
- Dr Mingzhen Liu
- Dr Christopher Davies
- Dr Rebecca Milot
- Dr Adam Wright
- Dr Qianqian Lin
- Dr James Ball
- Timothy, Olia, Alexander, Chelsea and Kilian

Snaith Group and in Particular
- Dr Nobuya Sakai
- Dr David Mcmeekin
- Dr Nakita Noel
- Dr Severin Habisreutinger
- Dr Jongchul Lim
- Martina, Alba, Federico, Jonny and Olivia

Staff at Lincoln College for Providing Food and Shelter
- Adil, Sue, Lucy, Scouts

My Friends & Fellow Vegetarians
- Dr James Harris & Dr Kathy Keown
- Dr Andre Nemeth
- Mr Henry-Martin Demasco
- Dr Alistair Inglis (v)
- Ms Joana Clemens (v)
- Purvil (v), Aynkkaran and Dillon

My Family
- Nikita (v), Ami (v), Hinal (v), Shiv (v)
- Aasar, Kavish, Sohum, Viraj
- Janki (v)
- Mother (v) & Father (v)

Contents

Chapter 1 1
Renewable Energy - Photovoltaics 1
Chapter 2 8
Theory & Background 8
2.1 Molecular Structure 9
2.1.1 Atomic Orbitals 9
2.1.2 Vibrational Spectroscopy 11
2.1.3 Molecular Orbitals 14
2.2 Electronic Properties 16
2.2.1 Band Structure 16
2.2.2 Semiconductors 19
2.3 Photovoltaic Devices 22
2.3.1 Bias Dependence in the Dark 22
2.3.2 Photogeneration 23
2.3.3 Photocurrent & Voltage 25
2.3.4 Series and Shunt Resistance 26
2.3.5 Power Conversion Efficiency 28
2.3.6 Temperature-Dependence of Voltage 29
2.3.7 Urbach Energy 31
2.4 Hybrid Metal-Halide Perovskite Photovoltaics 35
2.5 Organic Photovoltaics 40
Chapter 3 44
Experimental Methods 44
3.1 Vapour Deposition 45
3.1.1 Sequential Deposition 46
3.1.2 Co-Deposition 47
3.2. Thin-Film Characterisation 48
3.2.1 Ultraviolet-Visible Spectroscopy 48
3.2.2 X-ray Diffraction 51
3.3 Device Fabrication 52
3.3.1 Substrate Cleaning 52
3.3.2 Depositing Charge Transport Layers 52
3.3.3 Evaporation of Metal Contacts 54

3.4 Device Characterisation 55
3.4.1 Current-Voltage Characterisation 55
3.4.2 Fourier Transform Photocurrent Spectroscopy (FTPS) 56
3.4.3 Electroluminescence Spectroscopy 60
3.4.4 Scanning Electron Microscopy 60
3.4.5 Transmission Electron Microscopy 60
Chapter 4 61
Formation Dynamics of $CH_3NH_3PbI_3$ Perovskite Thin Films 61
4.1 Introduction 62
4.2 Results and Discussion 64
4.3 Summary 78
Chapter 5 80
Interface Morphology in Perovskite Photovoltaic Devices 80
5.1 Introduction 81
5.2 Results and Discussion 82
5.3 Summary 93
Chapter 6 94
Photocurrent Spectroscopy of Perovskite Photovoltaic Devices 94
6.1 Introduction 95
6.2 Results and Discussion 96
6.3 Summary 108
Chapter 7 110
The Effect of Ultraviolet Radiation on Organic Photovoltaic Devices 110
7.1 Introduction 111
7.2 Results and Discussion 114
7.3 Summary 128
Chapter 8 130
Conclusions and Outlook 130
Chapter 9 133
References 133

Chapter 1

Renewable Energy - Photovoltaics

As the world energy demand increases along with growing concerns associated with global warming, it is essential for us to develop low-cost and innovative technologies to harvest energy from renewable sources. Harvesting solar energy with photovoltaic (PV) devices is a clean and efficient method to extract and convert some of the 1366.1 W m^{-2} of solar irradiance upon the earth into electricity. [1]

Since 2007, the proportionate contribution of solar PV to the total power output from renewable energy sources has increased significantly, as shown in Figure 1.1.[2,3] Silicon-based PV devices are currently the dominant PV technology employed around the world. Initially the processing cost of crystalline silicon was expensive. However, in recent years, due to a large increase in demand, prices of PV modules have decreased significantly, making silicon PV a viable alternative to other renewable energy resources such as wind energy.

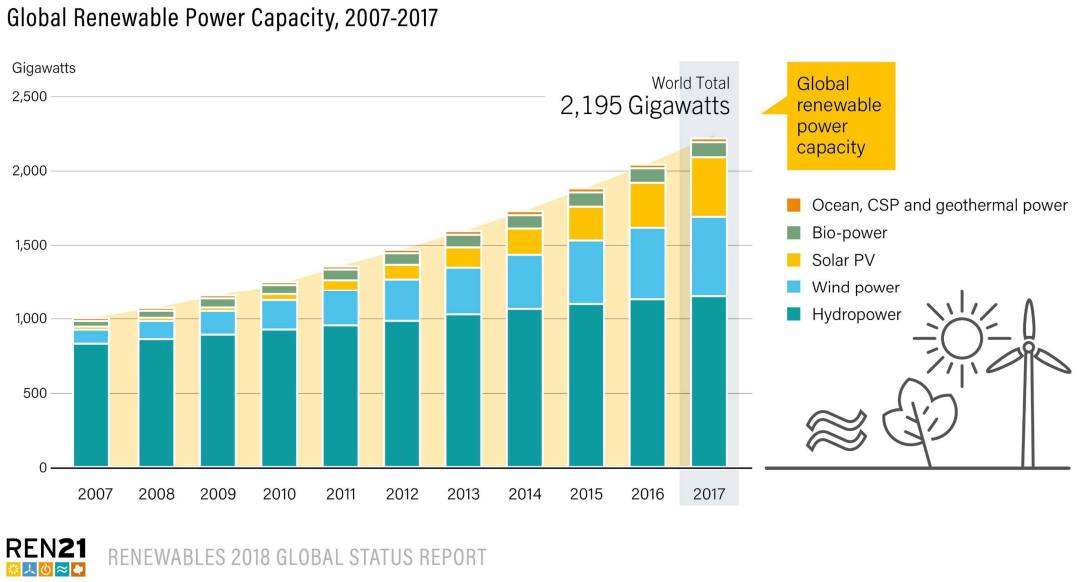


Figure 1.1: The rise in solar photovoltaic (PV) capacity within the global renewable energy power capacity over the past 10 years. As efficiencies and price per module decreases, solar PV technology will continue to increase. Reproduced with permission from REN21, 2018, Renewables 2018 Global Status Report, (Paris: REN21 Secretariat) [4]

Figure 1.2 shows that the cost of silicon PV (Si-PV) module has become cheaper since 2010, mainly because of the strong decrease in the cost of silicon.[5] However, the fabrication of the PV modules is still an energy intensive process. Therefore the energy payback time (EPBT), i.e. the amount of time it will take to generate the energy that was lost in creating the module, is higher for silicon modules than for thin film technologies such as cadmium telluride based photovoltaic modules.[6,7]

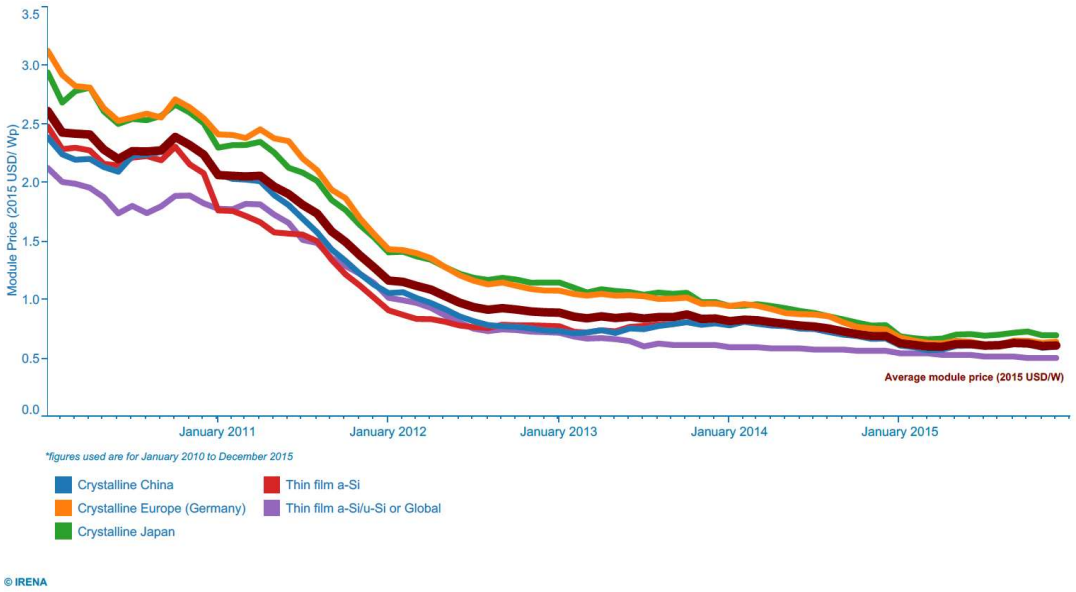


Figure 1.2: The price per watt of silicon photovoltaic modules. Reproduced with permission from IRENA© 2016 [8]

On the other hand, there are nascent PV technologies which have been investigated for applications that silicon modules cannot fulfil, for example; PV modules that are lightweight and flexible for use in vehicles, semi-transparent modules for integration into buildings and modules that have low cost processing techniques. In the midst of ongoing investigations on the dye-sensitized PV technology, metal-halide perovskite semiconductors showed favourable optoelectronic properties to be used as a photoabsorber in a solid state thin film style PV device.[9]

Since the discovery of hybrid metal-halide perovskite semiconductors as a suitable photoabsorber, intense research has shed light on the intrinsic material, optoelectronic and device properties, particularly for thin films fabricated using solution-processing methods.[10–12] Physical vapour deposition, in particular, thermal evaporation, is the dominant thin-film fabrication

technique used in industry. [13] The first planar-heterojunction perovskite device consisted of a $CH_3NH_3PbI_{3-x}Cl_x$ photoabsorber and yielded a power conversion efficiency of 15.4%.[14] The current record for vapour-deposited perovskite thin films is 20.3%,[15] approaching the PCE's of commercial Silicon PV modules and other thin film photovoltaic technologies such as CdTe and CIGS.

Perovskite semiconductors can be deposited on an existing silicon module to increase the PCE of the device.[16] Monolithic tandem devices are two solar cells, each of which absorb different parts of the solar spectrum, stacked on top of each other series connected, which will in return increase both the power conversion efficiency and the absolute potential efficiency of the PV device. The main advantage of vapour deposition is that perovskite thin films can be deposited on a variety of different substrates, as the technique requires no use of solvents and yields uniform and pin-hole free thin films. Therefore, vapour deposition is an ideal fabrication technique to deposited metal-halide perovskite thin films on silicon for high PCE monolithic tandem device. However, there has been little understanding on the mechanism by which the perovskite forms in the solid-state, especially when it is fabricated through vapour deposition. Moreover, the device architectures used previously have shown significant hysteresis between the forward and reverse current voltage sweeps, making the origin of the hysteretic device behaviour critical to understand.

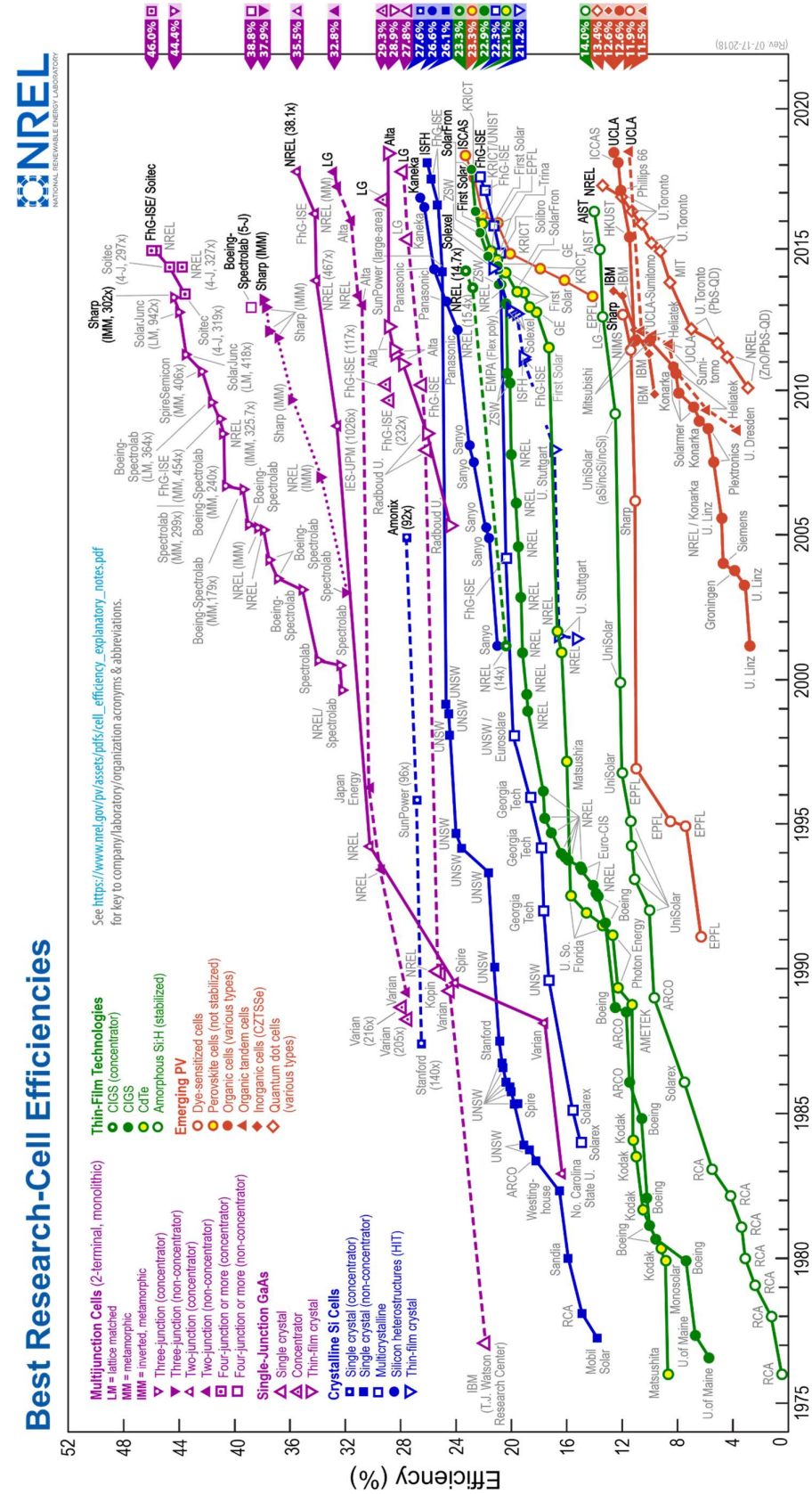


Figure 1.3: A graph showing the variety of different PV technologies and their power conversion efficiency (PCE) progression over time. This thesis reports on investigations of an emerging PV technology, metal-halide perovskite semiconductors (red-yellow circles). Reproduced from NREL 2018 [17]

The work presented in this thesis provides an understanding of the formation of the hybrid metal-halide perovskites at the molecular level, elucidating the perovskite structure in the microscopic level and the subsequent effect of microscopic features on the power conversion efficiency. Furthermore, a hybrid metal-halide perovskite device, fabricated using vapour deposition, is characterised using optical and electrical spectroscopic techniques to reveal the viability of hybrid metal-halide perovskite PV devices for space applications. The final investigation examines the effect of ultraviolet light from simulated solar light in organic photovoltaic devices.

This thesis structure is as follows. **Chapter 2** gives a broad overview of the molecular orbital theory, and the formation of semiconductors by the linear combination of atomic orbitals. A brief theoretical explanation is given on vibrational and electronic spectroscopy. Thereafter the chapter explains the device physics of a photovoltaic device. Lastly, a literature review is given on the main material investigated in this thesis; $CH_3NH_3PbI_3$. **Chapter 3** provides experimental details of the techniques used to fabricate and characterise vapour-deposited perovskite thin films. The latter half of the chapter explains the device characterisation techniques used, such as photocurrent spectroscopy, current-voltage measurements and electroluminescence spectroscopy.

Next, the thesis presents findings of four investigations, where each chapter includes a detailed literature review relevant to the investigation, followed by presentation of the results, discussion and a summary.

The investigation presented in **Chapter 4** surrounds the two-step vapour deposition process, where the results show the importance of moisture during the initial crystallisation process of the perovskite. **Chapter 5** examines seven

device architectures employing a variety of different charge extraction layers in tandem with co-evaporated $CH_3NH_3PbI_3$ thin films. Using current-voltage analysis and microscopy, the results exemplify the importance of perovskite morphology, at the interface with other materials, on device performance. **Chapter 6** inspects the temperature-dependence of key device characteristics (J_{sc} and V_{oc}) and the photocurrent spectra of $CH_3NH_3PbI_3$ devices. With the results from chapter 5 exemplifying the need to use organic semiconductors in vapour-deposited perovskite solar cells, **Chapter 7** displays the effect of ultraviolet light on bulk heterojunction organic solar cells. Finally, the thesis concludes with a summary of the investigations and an outlook on future experiments which may allow for greater understanding of vapour-deposited hybrid metal-halide perovskites and the implementation of them in industrial processes.

Chapter 2

Theory & Background

This chapter explains how molecular orbitals determine the electronic properties of a solid and why semiconductors can be used in photovoltaic devices. Finally, the physics of photovoltaic devices will be described followed by an introduction to hybrid metal-halide perovskite-based photovoltaics.

2.1 Molecular Structure

The electronic properties of a material are principally governed by the bonding profile between the various atoms in the material. This section gives a brief overview on what an atomic orbital symbolises and how each orbital's spatial configuration has a definite energy. From atomic orbitals in an atom, a molecular orbital is formed when two or more atoms chemically interact to form ionic or covalent bonds. Along with the electronic configuration of the atoms, the extent of overlap between different atomic orbitals in polyatomic structures determines their band structure and whether the material is an insulator, metal or a semiconductor.

2.1.1 Atomic Orbitals

The electronic properties of a material are governed by electrons. The time-independent Schrodinger equation,

$$\mathrm{E}\psi = -\frac{\hbar^2}{2\mu}\nabla^2\psi - \frac{Ze^2}{4\pi\varepsilon_0 r}\psi \tag{2.1}$$

where $\hbar$ is the reduced Planck constant, μ is the reduced mass, ε_0 is the vacuum permittivity, r is the distance between two charges, Z is nuclear charge and e is the elementary charge can be used to determine the one-electron wavefunction of an electron in an atom. The potential energy of the system is centrosymmetric around the centre of mass and therefore the one-electron wavefunction can be solved, yielding two distinct parts, one representing the radial wavefunction R(r) and the other the angular wavefunction Y(θ,ϕ):[18]

$$\psi_{n,l,m_l}(r,\theta,\phi) = R_{n,l,}(r)\, Y_{l,m_l}(\theta,\phi) \tag{2.2}$$

An atomic orbital is described by three quantum numbers, n, l, and m_l of the electron wavefunction (ψ) where n is the principle quantum number, l is the orbital angular quantum number and m_l is the magnetic quantum number. Different n, l and m_l values will yield a spatial profile of the atomic orbitals. The principle quantum number, n, has the energy,

$$E_n = \frac{hcR_N Z^2}{n^2} \tag{2.3}$$

R_N is the Rydberg constant, c is the speed of light and atomic number Z. Figure 2.1 shows the spatial profile of the atomic orbitals for up to $n \leq 3$. Essentially, an atomic orbital represents the probability of finding an electron in that given space. Atomic orbitals are filled, starting with the lowest energy orbital, with two electrons of opposing spin (as per Pauli exclusion principle) occupying each orbital. The electrons in the highest energy orbitals, and unfilled orbitals, can interact with neighbouring atomic orbitals of other atoms to form a chemical bond.

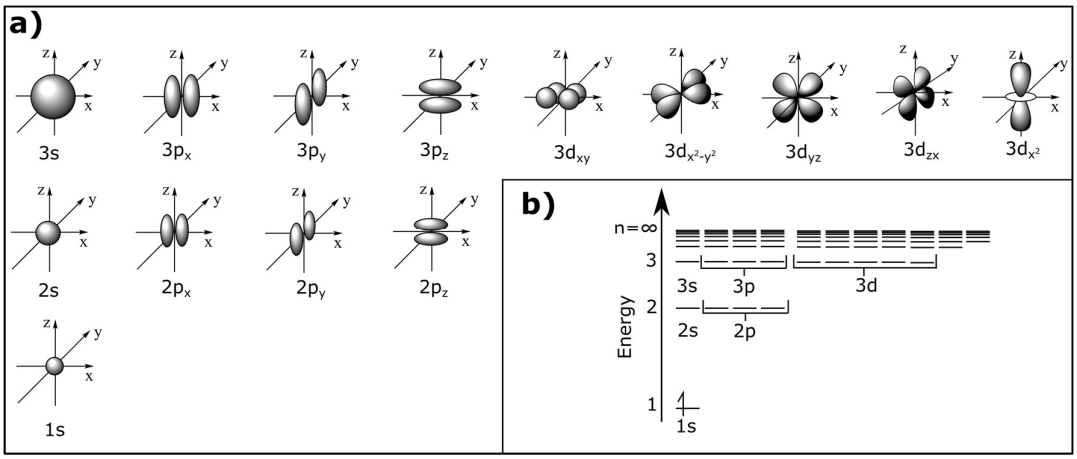


Figure 2.1: a) The spatial profile of the s, p and d subshells in different shells (n). The lowest value of n represents the shell closest to the nucleus. **b)** The electronic configuration of a hydrogen atom. The sole electron is occupying the lowest orbital which is the spherical 1s, orbital. The rest of the unoccupied orbitals form the continuum states or unbound states of the atom. A photon with energy greater than the difference between an unbound orbital and bound orbital can excite the electron to the higher energy state, however there are selection rules as described in the main text. The figure was adapted from[19].

2.1.2 Vibrational Spectroscopy

The bond between two atoms is elastic, and constantly vibrates around a mean position. The vibrations are due to the periodic stretching and compression of the bond because of attractive and repelling forces between electrons and the nuclei of each atom. The vibrational motion can be interpreted as a harmonic oscillator. The frequency at which the vibrations occur are of the order 10^{13}-10^{14} Hz. With the absorption of electromagnetic radiation, in the infrared region (300-4000 cm^{-1}),[18] the lowest energy vibration (v_0) can be excited into higher energy vibrational states (v_i). Therefore, based on the Schrödinger time-

independent equation, the energy E_v of the vibrational energy levels can be approximated as [20]

$$E_v = \left(v + \frac{1}{2}\right)\hbar\tilde{\nu} \qquad \tilde{\nu} = \frac{1}{2\pi c}\left(\frac{k}{\mu}\right)^{\frac{1}{2}} \qquad v = 0, 1, 2 \ldots \tag{2.4}$$

where $\tilde{\nu}$ is the frequency in wavenumber, k is the force constant and μ is the reduced mass. In most molecules, bonds are not homogenous and cannot stretch infinitely, hence with enough energy the bond will eventually dissociate, introducing anharmonicity at higher vibrational states as shown in Figure 2.2. The molecular potential energy curve takes the form of the Morse function[20]

$$E_v = \left(v + \frac{1}{2}\right)\hbar\tilde{\nu} - \left(v + \frac{1}{2}\right)^2 \hbar\tilde{\nu}x_e \qquad v = 0, 1, 2 \ldots \tag{2.5}$$

where x_e is the anharmonicity constant. For a transition to occur the selection rule applies

$$\Delta v = \pm 1, \pm 2, \pm 3 \tag{2.6}$$

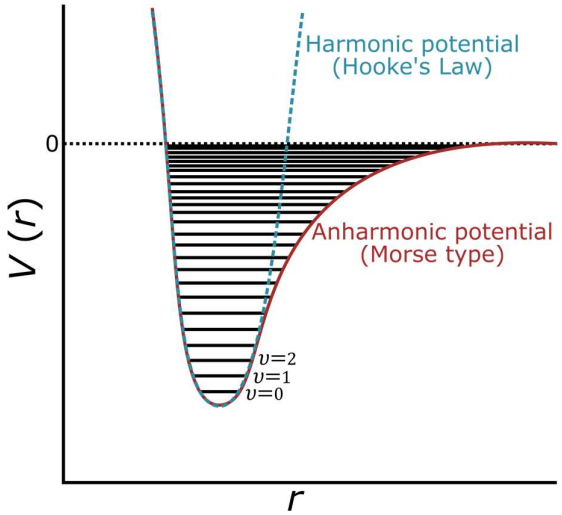


Figure 2.2. The potential energy V(r) curve for a harmonic oscillator represented by Hooke's law and the potential energy V(r) for anharmonic oscillator potential curve represented by Morse function. At low energies, the displacement between two atoms can be approximated by harmonic type oscillation, however at higher energy due to anharmonicity, the vibrations are more accurately reflected as an anharmonic oscillator. The figure was adapted from[21]

The absorption of an IR photon only occurs if there is an uneven charge distribution in the molecule i.e. if the atoms are polar with respect to each other. The electric field generated by infrared radiation will displace the vibrational motion of the molecule, thus exciting the molecule to a higher vibrational state. Homonuclear diatomic molecules (H_2 for example) are infrared *inactive*, as the dipole moment does not change between stretching and contracting oscillations in the molecule. In a heteronuclear molecule (CH_4) the dipole moment changes as the bonds oscillate, allowing for absorption of a photon and a transition into a higher energy vibration state, making the bonds in the molecule infrared *active*. Infrared spectroscopy allows for a spectrum of the infrared active vibrational transitions of chemical bonds in a material to be recorded. As each molecular bond has different ground state vibrational frequencies, excitation of the vibration via infrared radiation will result in absorption of the infrared light at corresponding frequencies of each bonds. For a polyatomic molecule which consists of many bonds there are *3N* degrees of freedom; these include vibrational, rotational and translational movements. The number of fundamental vibrations or vibrational modes that a molecule can have are:

$$3N - 6 \qquad \text{Non-linear Molecule} \qquad (2.7)$$

$$3N - 5 \qquad \text{Linear Molecule}$$

Neighbouring molecules can dampen or increase the vibrational frequency of a bond, resulting in a shift in the infrared absorption spectrum. Electrostatic, van der Waals, and hydrogen bonding interactions between molecules can induce a small but detectable change in frequency.[22,23] Thus, infrared spectroscopy allows the deduction of the molecular composition of a material and may also be

utilised to carefully track chemical changes that may occur in a material due to the introduction of new molecules to the host material.

2.1.3 Molecular Orbitals

When atoms form bonds, the description of the resulting orbital can be described using molecular orbital theory (MO theory). When atom A and atom B form a bond, consequently forming a molecule, the bonding electron in atom A could be found in any orbital of atom A (ψ_A) and B(ψ_B), and vice versa for the bonding electron from atom B. Therefore, the approximate overall wavefunction of the diatomic molecular orbital is a superposition of ψ_A and ψ_B which is termed as a linear combination of atomic orbitals (LCAO)

$$\psi_{\pm} = N_{\pm}(\psi_A \pm \psi_B). \tag{2.8}$$

From the combination of two atomic orbitals, the wavefunction can symbolise the electron density in two ways, one in which it is prominent between the two nuclei of the atoms (bonding MO) and another where the electron density is concentrated towards its respective nucleus (anti-bonding MO).

In a polyatomic molecule, such as semiconductors, there can be many different elements and hence there are important factors such as electronegativity of an element, which would lead to a polar bond, and the energy of the different atomic orbitals that take part in creating a chemical bond. Therefore, the wavefunction for polyatomic molecular orbital (LCAO-MO) includes a coefficient c, which accounts for the differences in electronegativity, and energy of the orbitals in atoms of different elements.

$$\psi = \sum_i c_i \psi_i \tag{2.9}$$

The LCAO approach can be used to calculate the electronic structure of solids, in particular crystals. A crystal is when atoms are tightly packed together in a repeating regular array.[24] For a crystalline solid, the electronic properties can be understood by analysing one repeating unit, 'a unit cell'. Figure 2.3 shows the formation of density of allowed states that arise in a polyatomic solid.

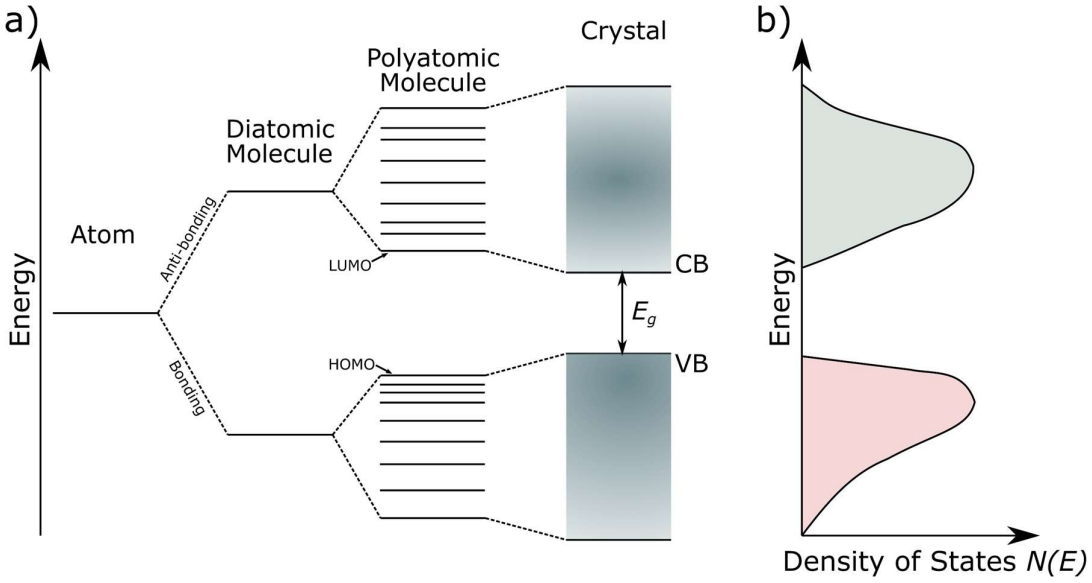


Figure 2.3. a) A schematic of the formation of different energy states from a single atom to a crystal containing '*N*' atoms. The band structure of the crystal can result in a bandgap (E_g) between the conduction (CB) and valence band (VB) as described in 2.2.1 **b)** In a solid, the overlap of orbitals of different energies and crystal imperfections lead to a continuum of states. Therefore, in a volume of solid, the total allowed energy states per energy is termed the density of states. The figure was adapted from[25].

2.2 Electronic Properties

This section describes the origins of band structure and how the band structure can aid classing materials as metals, insulators or semiconductors. Thereafter the formation and resulting properties of a *p-i-n* junction is explained. The section is based on the textbooks; 'The Oxford Solid State Basics' by Steven H. Simon and 'Physics of solar cells' by Jenny Nelson.

2.2.1 Band Structure

A unit cell is described as the smallest possible configuration of atoms in a lattice that when repeated infinitely in a three-dimensional lattice, results in a crystal. The periodicity introduced in the lattice by the infinite repetition of unit cells, allows for a simplification of the behaviour and properties of electrons in a crystal. A Bloch function describes the wavefunction of a particle in a periodic potential

$$\psi(\mathrm{k},\mathrm{r}) = \upsilon_{jk}(\mathrm{r})e^{i\mathrm{k}.\mathrm{r}} \qquad 2.10$$

where k is the wavevector, υ_{jk} (r) is the periodic function and $e^{ik.r}$ represents the wavefunction of an electron (atomic orbital). Combining the LCAO approximation in equation 2.9 with the Bloch function results in a band structure diagram with respect to the different points in the unit cell. Figure 2.4 shows a basic band diagram representing a linear monoatomic chain. As the amount and type of atoms vary, the band structure will increase in complexity, to reflect the possible eigenstates in the unit cell.

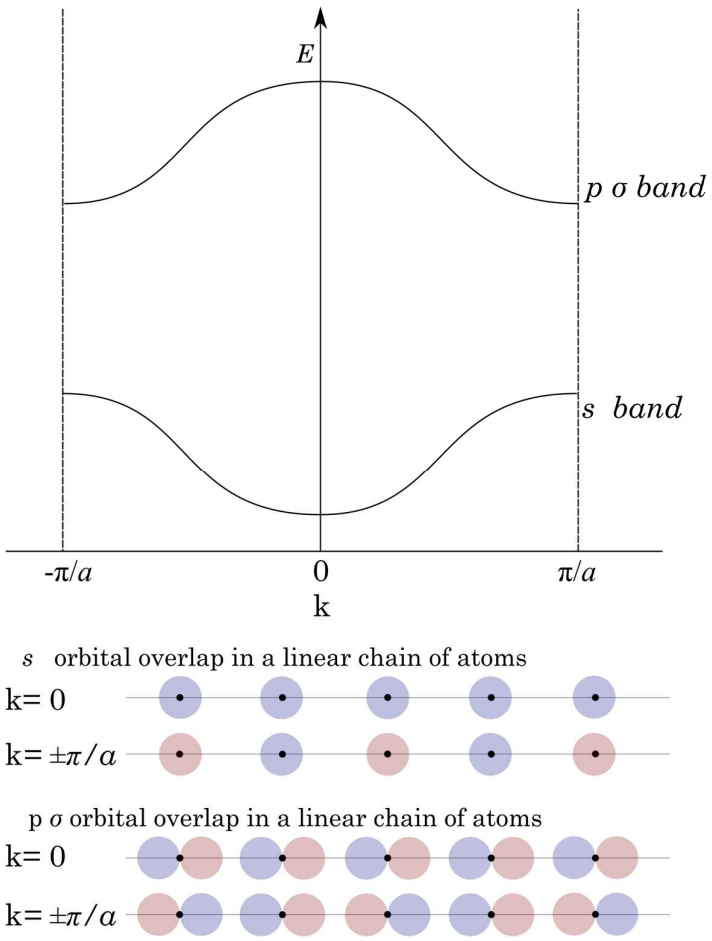


Figure 2.4. A band structure diagram of atoms in a 1-dimensional linear chain. The energy *E* as a function of wavevector k. The schematic of the linear chain shows the orbital overlap of the s and p σ orbitals along different directions of wavevector k. This figure was adapted from [25].

The electronic configuration of the atoms that constitute a unit cell determine the energy of the bands. The lower energy filled band is termed the valence band (VB) and the unfilled higher energy bands are termed the conduction band (CB). Figure 2.5 shows how the relative energy of the valence and conduction band determines whether a material is an insulator, semiconductor or a metal.

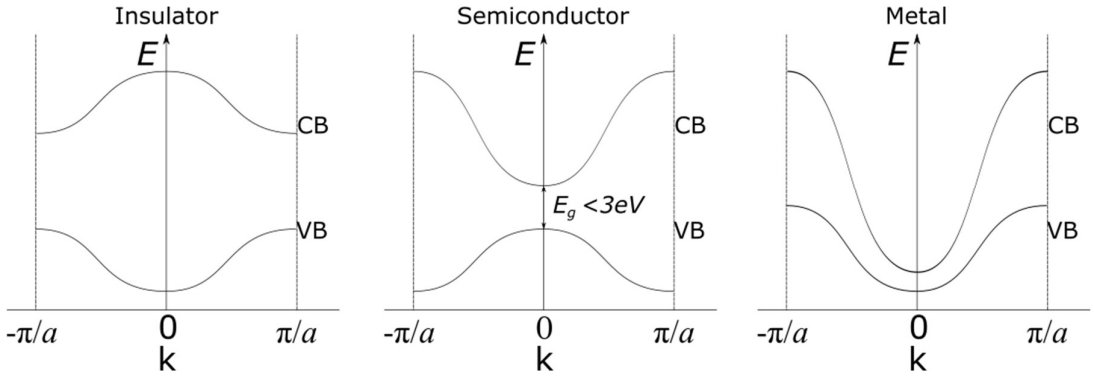


Figure 2.5. A simplified band structure diagram showing how the energy of the conduction band (CB) and the valence band (VB) determine whether a material is an insulator, semiconductor or metal.

A purely metallic solid is tightly packed, allowing for strong overlap between neighbouring atoms. The tightly packed nature of the atoms and the fact that there are empty orbitals of the same energy levels, allows a network of unoccupied states, i.e. the conduction band, to overlap with the valence band. Therefore, the valence electrons are delocalised throughout the material.

On the other hand, as shown in Figure 2.5, the band structure of a material may result in an energy gap (E_g) between the valence band (VB), and the conduction band (CB). In molecular solids, such as polymers, the energy gap (E_g) is the difference between the highest occupied molecular orbital (HOMO) and the lowest occupied molecular orbital (LUMO). The magnitude of E_g can determine whether the material is a semiconductor or an insulator. At T=0 K non-metallic solids, without any dopants, will act as an insulator. However as soon as there is thermal energy, and the band gap is sufficiently small (0.5 eV – 3 eV),[26] electrons can be excited into the conduction band, and conduct electricity; these materials are considered semiconductors. However even with considerable

amount of thermal energy (for e.g. T=295 K), if the E_g is too large (>3 eV), there will not be electrical conduction. Hence, the material would be considered an insulator.

2.2.2 Semiconductors

As mentioned in the section 2.2.1. at T=0 K all the electrons occupy the states of the valence band and the conduction band is empty. As the temperature of the semiconductor increases, electrons are thermally excited into the conduction band from the valence band, leaving behind a positively charged vacancy in the valence band. This vacancy is termed as a 'hole'. In a thermal equilibrium, the distribution of electrons in the valence band and the conduction band of a semiconductor is described by Fermi-Dirac statistics. The Fermi-Dirac distribution function represents the probability of occupied states of energy, E, at a temperature T. The Fermi Dirac distribution is:

$$f(E, E_F, T) = \frac{1}{e^{(E-E_F)/k_B T}+1} \tag{2.11}$$

where E_f is the Fermi level energy, T is temperature and k_B is the Boltzmann constant.

It is common to represent the various physical quantities associated with the band gap of the semiconductor with an energy band diagram as shown in Figure 2.6. The electron affinity, χ, is the amount of energy released when an electron from free space (vacuum) is added into the LUMO of a molecule or CB of a semiconductor.[26] E_{vac} is the vacuum level, the energy at which the electron is in free space, directly outside of the material. The ionisation potential is the amount of energy required to remove (ionise) an electron from the HOMO of a molecule or the VB of a material into free space.

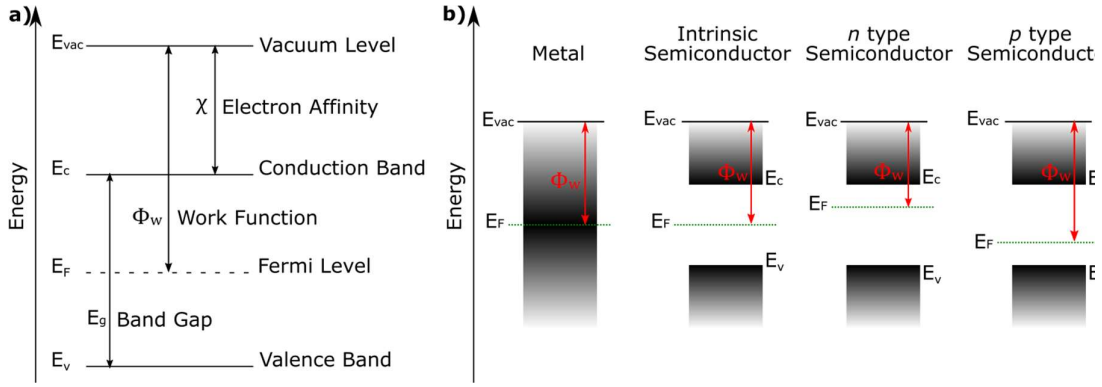


Figure 2.6: a) Band energy diagram of a material with the corresponding terms. **b)** Band diagram showing the changes in Fermi level (E_f) and work function (Φ_w) induced by extrinsic of donor (n-type) and acceptor (p-type) impurities or by introducing native point defects.

Introducing dopants into a semiconductor can alter the Fermi-level in the semiconductor, as shown by Figure 2.6. Donor atoms can be added to the intrinsic semiconductor to increase the electron density in the material, which will consequently result in the Fermi-level to shift closer to the conduction band, E_c. Introducing acceptor atoms to an intrinsic semiconductor, results in a decrease in the electron density in the intrinsic semiconductor, effectively creating holes in the valence band, resulting in a downward shift of the E_F.

The work function of a material is defined as the potential required to remove the least tightly bound electron[26]

$$\Phi_w = (E_{vac} - E_F) \tag{2.12}$$

In metals,

$$\chi = E_F = \Phi_w \tag{2.13}$$

When two materials are brought in contact (Figure 2.7), for example a metal and a semiconductor or a n-type semiconductor and a p-type semiconductor, there will be an electrostatic potential difference between the two materials.

Since the E_F is constant in thermal equilibrium, the Fermi-level will align with the other material it is in contact with, creating an internal field which is utilised in a working photovoltaic device.

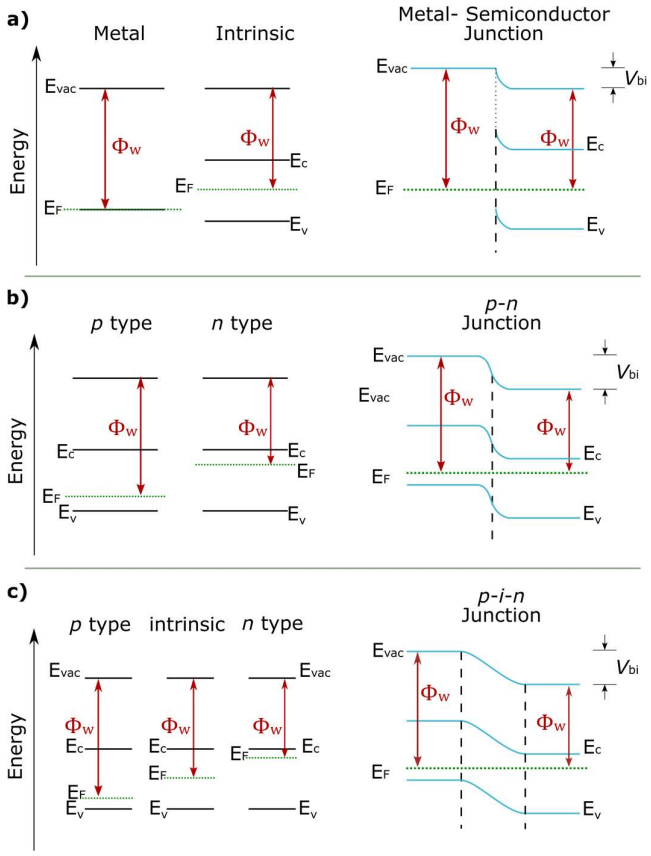


Figure 2.7. a) The band diagram of a metal and an intrinsic semiconductor when brought into contact and the subsequent alignment of Fermi-levels of each material at the junction, which induces a Schottky barrier **b)** When a p-type and a n-type semiconductor are contacted, the corresponding interface will result in charge-carriers to diffuse to the other side and this will result in a depletion layer. The effect of depletion layer is a built-in field (V_{bi}) between the two semiconductors. **c)** An intrinsic semiconductor sandwiched between p- and n-type semiconductors. The intrinsic semiconductor is important to generate photocurrent, so the thickness should be appropriate in ensuring maximising absorption, but thin enough for the generated charge-carriers can diffuse to interface for extraction.

2.3 Photovoltaic Devices

The following section will discuss how *p-i-n* diodes behave under electrical and light biasing. The section ends with a literature review of the temperature-dependence of the open circuit voltage in a photovoltaic device and discuss the origin of the Urbach tail in absorption onset of semiconductors.

2.3.1 Bias Dependence in the Dark

In a *p-i-n* diode the intrinsic semiconductor is effectively an extended depletion layer influenced by the p- and n- type semiconductors at each interface. The depletion layer generates the internal built-in field (V_{bi}). In the case of a *p-i-n* diode, when the different semiconductors come in contact, the electrons from the n-type semiconductor flow towards the p-type semiconductor through the intrinsic semiconductor. Such diffusion occurs until the Fermi levels across each of the three semiconductors are aligned, as shown in Figure 2.8. The built-in field generated by the depletion region will result in rectification. Rectification is when the current will flow easily through the junction in forward bias than in reverse bias. In reverse bias there will be very high resistance because of the increased length of the depletion region. Figure 2.8 shows the rectifying behaviour that occurs in a typical p-i-n junction when a photovoltaic device is placed under forward and reverse bias in the dark.

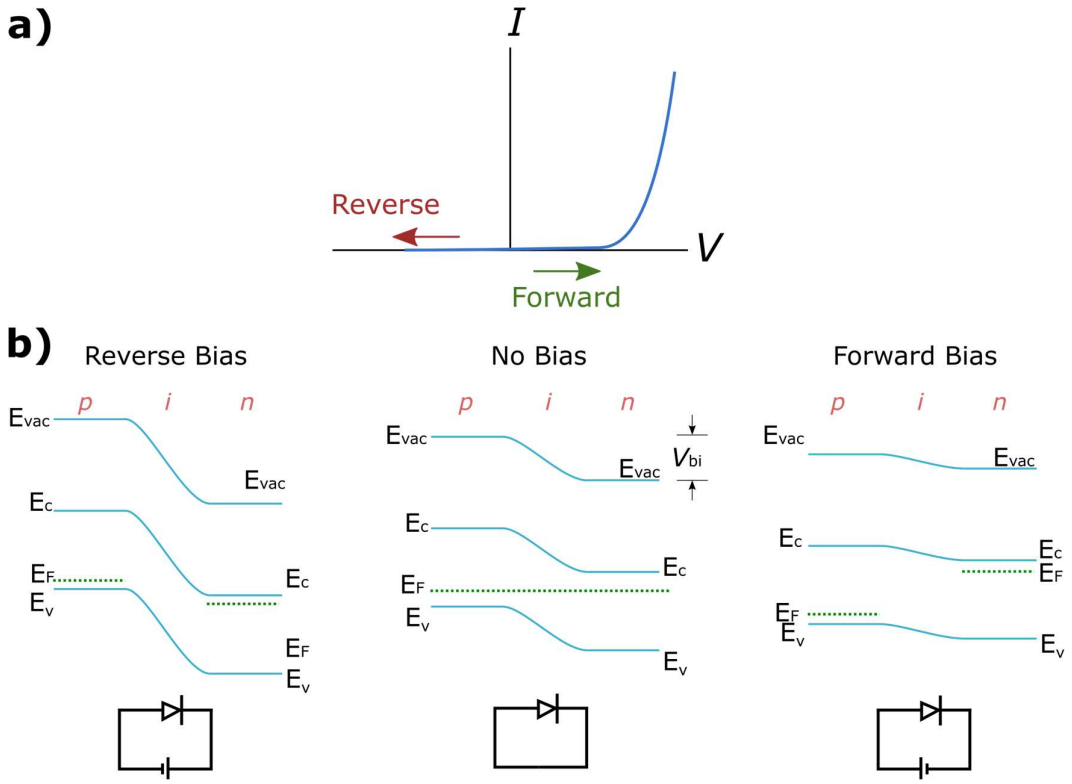


Figure 2.8. a) Current-voltage (*J*-*V*) sweep of a semiconductor displaying rectifying behaviour. **b)** The band energy diagram for a *p*-*i*-*n* junction under different biasing conditions.

2.3.2 Photogeneration

When an incident photon of energy greater than the E_g of the semiconductor is absorbed, an electron in the VB is excited to the CB; this is called photogeneration of charge-carriers. In semiconductors where the Columbic interaction between the electron and hole is strong, photoexcitation will lead to a generation of an exciton at room temperature. An exciton has an energy lower than the value of E_g. The difference in energy between the E_g and the excitonic energy at 0 K yields the exciton binding energy, E_b.[26] In most semiconductors, the value of E_b is lower than k_BT, hence excitons dissociate at room temperature. However, in organic semiconductors, electrons and holes are strongly localised, leading to $E_b > k_BT$ at room temperature.

Without any inbuilt field or external bias, a photoexcited electron will relax back down to the ground state. The relaxation occurs via a radiative or non-radiative recombination process. In a photovoltaic device, photogeneration of charge-carriers is followed by a competing process of either extraction of free charge-carriers or recombination. The external quantum efficiency (EQE) is a measure of the probability that an incident photon energy E will deliver one electron to the external circuit, with

$$EQE\ (E) = \frac{J_{SC}}{q b_S(E)} \tag{2.14}$$

where $b_s\ (E)$, is the incident photon flux, and q is the electronic charge.

As shown in Figure 2.8b, placing the device under a forward bias will result in the Fermi-levels of the n-type and p-type materials to split from the equilibrium position. Under illumination and in the low injection regime ($V<V_{oc}$), photogeneration of electrons and holes will result in quasi Fermi-level splitting in an intrinsic semiconductor, yielding a photovoltage.

Photovoltaic devices convert the incident power generated by a light source to electrical energy. Electric power is defined by

$$P = I \cdot V \tag{2.15}$$

Where P is power, I is current, and V is voltage. The photovoltage and photocurrent generated by photoexcitation of an electron in the VB, can be measured by a current-voltage (J-V) sweep measurement. The current density (J) is conventionally used as solar cell parameter rather than current (I) as it allows for comparison of devices with different pixel sizes (illumination areas). Figure 2.9 shows a typical J-V curve for a hybrid metal-halide perovskite solar cell under dark and illumination.

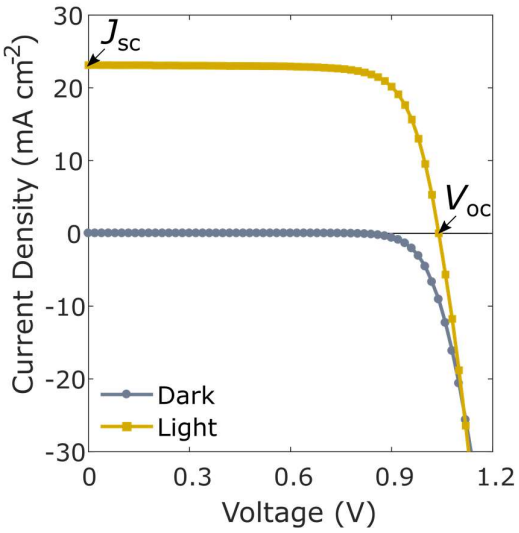


Figure 2.9. Current-voltage (*J*-*V*) curve of a perovskite solar cell, under dark and illumination (light).

2.3.3 Photocurrent & Voltage

Within a photovoltaic device, during illumination and electrical biasing there are two opposing currents of electrons and holes. A forward bias will reduce the depletion region and will result in majority carriers drifting across the *p*-i-*n* junction. This will lead to recombination of the charge-carriers, thus resulting in a net current. This current is bias dependent and termed the dark current density (J_{dark}). The dark current density in an ideal diode is

$$J_{dark}(V) = J_o(e^{\frac{qV}{k_BT}} - 1) \qquad (2.16)$$

where, J_o is the reverse saturation current, which is strongly influenced by recombination mechanisms within the diode. In short circuit conditions, i.e. when there is no external load (no bias), photogenerated charge-carriers will separate and diffuse to the electrode. The photocurrent is directly dependent on the size of E_g and the intensity of the light. The lower the value of E_g the higher the total photocurrent, as there will be more photons with $E > E_g$ when the device

is illuminated with AM 1.5 spectrum light. The total current therefore generated by the device is

$$J(V) = J_{ph} - J_{dark} \ . \tag{2.17}$$

Thus, for an ideal diode under illumination the equation becomes

$$J = J_{ph} - J_o(e^{\frac{qV}{k_B T}} - 1) \ . \tag{2.18}$$

The device is in an open circuit configuration, when the contacts are isolated. Measuring the voltage under illumination with a voltmeter, will show the open circuit voltage. When the device is put under a load, the open circuit voltage (V_{oc}) is the point at which the dark current and photocurrent yields no net current. The V_{oc} for an ideal diode is therefore when J=0, yielding

$$V_{oc} = \frac{kT}{q} ln\left(\frac{J_{sc}}{J_0} + 1\right) \ . \tag{2.19}$$

2.3.4 Series and Shunt Resistance

During electrical conduction in a photovoltaic device, the device experiences two main types of resistance. Series resistance (R_s) is the overall resistance induced by the different contacts in the device, for example metal-metal, metal-semiconductor and semiconductor-semiconductor contacts and the bulk resistance of each layer. A photovoltaic device may have many such interfaces which would induce such resistance. In an ideal diode, the R_s should be infinitely small. As R_s>0, the gradient of the slope of the J-V curve decreases at higher voltages lowering the voltage at the maximum power point as shown in Figure 2.10a. Shunt resistance or parallel resistance R_{sh} can arise because of a leakage of the current (around the V_{oc}) across the junction or because two materials with vastly different polarities come in contact with each other. Ideally the R_{sh} should be infinitely large. As the R_{sh} decreases, the gradient of the slope increases,

lowering the current at the maximum power point, as shown in Figure 2.10b. Any such changes described above will directly influence the fill factor (FF) as the maximum power point will change, and consequently the power conversion efficiency (PCE). Both the FF and PCE are described in Section 2.3.5. The ideal diode equation which takes into consideration different resistances acting in a photovoltaic device, is given by

$$J = J_{sc} - J_o\left(e^{q\left(\frac{V+JAR_S}{kT}\right)} - 1\right) - \frac{V+JAR_S}{R_{sh}} \tag{2.20}$$

where A is the area of the device. R_s can be a more difficult problem to overcome in a multijunction device due to different conductivities of the layers and the quality of the interface formed between the different layers.

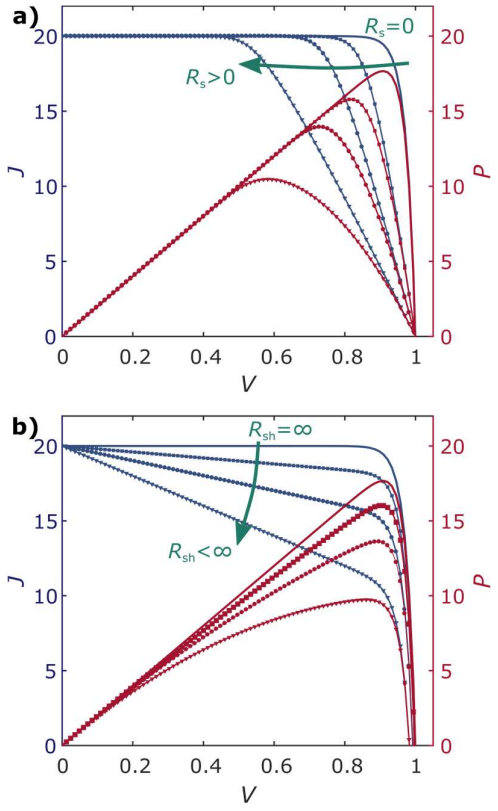


Figure 2.10. a) Current-voltage (J-V) curve as the series resistance (R_s) increases which brings about a decrease in power density (P). **b)** J-V curve as the shunt resistance (R_{sh}) decreases, which brings about a decrease in the power density (P).

2.3.5 Power Conversion Efficiency

The power conversion efficiency (PCE) of a photovoltaic device is obtained by measuring key solar cell device parameters, J_{sc}, V_{oc}, fill factor (FF) and the incident power (P_{in}).

$$PCE = \frac{J_{sc}V_{oc}FF}{P_{in}} \tag{2.21}$$

$$FF = \frac{J_{mpp}V_{mpp}}{J_{sc}V_{oc}} \tag{2.22}$$

The fill factor of the device (FF) describes the 'squareness' of the diode curve. The fill factor is significantly impacted by the different resistances that act in the device, as explained in Section 2.3.4.

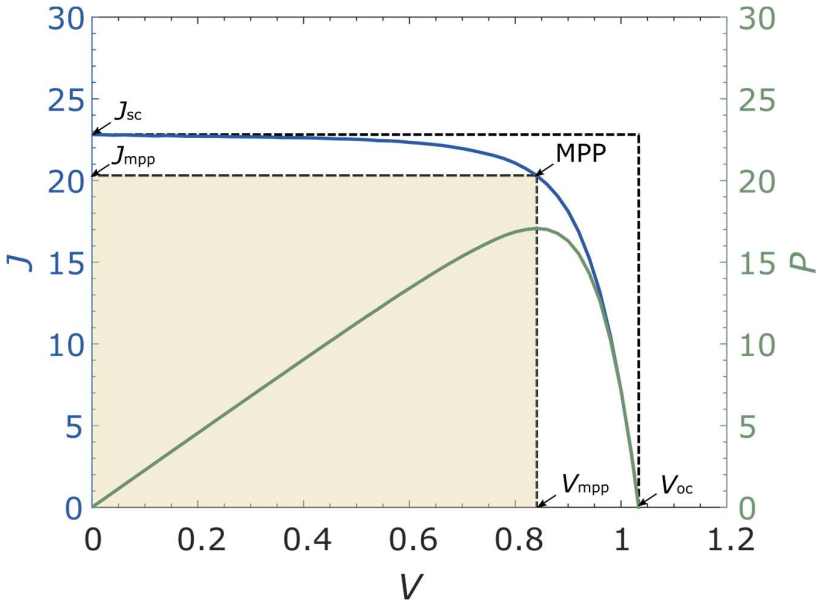


Figure 2.11. The current density, J (blue line) and the power density 'P' (green line) plotted against the voltage. The maximum power point (MPP), has a voltage (V_{mpp}) and a current density (J_{mmp}).

2.3.6 Temperature-Dependence of Voltage

The value of E_g for semiconductors, barring any phase transitions, has been experimentally shown to have the following relationship with temperature, [27]

$$E_g = E_0 - \frac{\alpha T^2}{(T+\beta)} \tag{2.23}$$

where α and ß are constants and E_0 is the energy of the bandgap at 0 K. The dominant reason for the temperature-dependence of the value of E_g is because of the temperature induced expansion or contraction of the lattice, which leads to a shift in energy of the CB and VB. The value of E_g is fundamental in determining the final V_{oc} of a photovoltaic device. As shown in Figure 2.8, under forward bias the quasi-Fermi level splits in a typical *p-i-n* heterojunction. The difference in the quasi-Fermi levels yields the final V_{oc} of the device. In a non-degenerate semiconductor above 0 K, the Fermi-Dirac distribution can be approximated using the Boltzmann distribution. [28] The temperature dependence of the V_{oc} is then given by: [29]

$$\frac{dV_{oc}}{dT} \approx \frac{dE_g/q}{dT} + \frac{V_{oc}-E_g/q}{T} \tag{2.24}$$

The broadening of the Fermi-Dirac distribution as the temperature increases effectively leads to the quasi-Fermi levels approaching each other, resulting in a lower V_{oc}. The measured temperature-dependence of V_{oc} for different inorganic and organic photovoltaic devices is shown in Figure 2.12. Photovoltaic devices fabricated solely with organic semiconductors have shown to deviate from the equation 2.24 at temperatures below 200 K, predominantly due to organic photovoltaics being excitonic and requiring a dissociative interface for generation of free charge-carriers. [30]

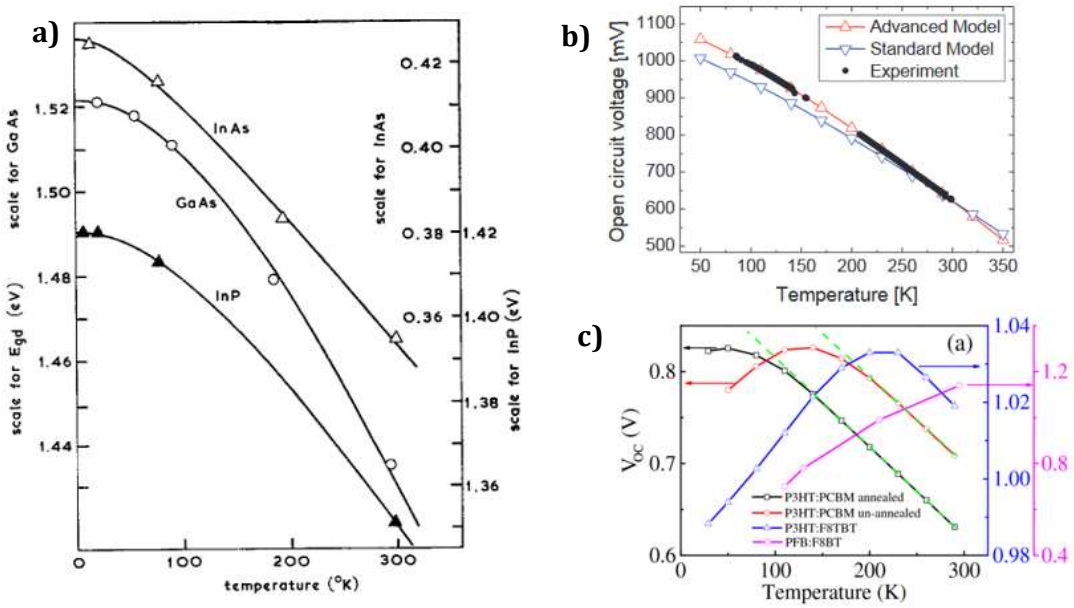


Figure 2.12. a) Experimental results showing the Varshni temperature dependence of the E_g in GaAs, InP and InAs. Reprinted with permission from Varshni, *Physica* 1967, 34 (1), copyright 1967 Elsevier B.V [27] **b)** Experimental and theoretical results showing the temperature dependence of the V_{oc} in a silicon solar cell by Löper *et al.* Reprinted with permission from Löper *et al.* , *Energy Procedia* 2012, 27 copyright 2012 Elsevier Ltd [28] **c)** Gao *et al.* observed that the V_{oc} of organic solar cells does not follow the same trend as that of the inorganic solar cell, mainly due to a decrease in charge separation at lower temperatures in organic solar cells. Reprinted with permission from Gao *et al.*, *Phys. Rev. Lett.* 2015, 114 (12). Copyright 2015 American physical society[30].

2.3.7 Urbach Energy

Whilst investigating photographic emulsions of alkali halides, Franz Urbach observed that when the absorption coefficient (α) was plotted on a logarithmic scale, the resulting slope had a ~$1/k_BT$ relationship as shown in Figure 2.13.[31]

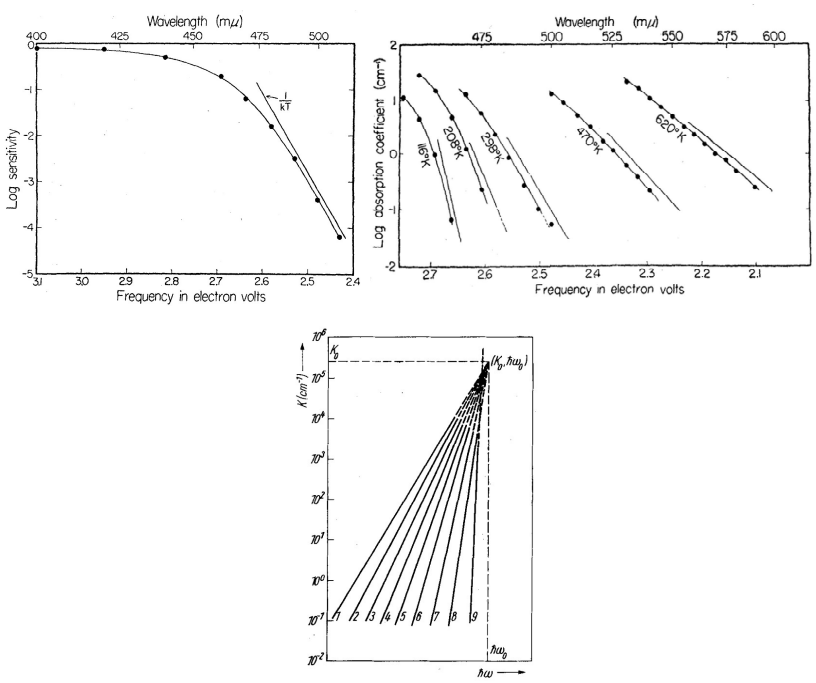


Figure 2.13. a) Franz Urbach's first observation of the log absorption onset vs frequency followed a $1/k_BT$ linear relationship. Reprinted with permission from Urbach, *Phys. Rev.* 1953, 92 (5). Copyright 1953 American physical society[31] **b)** Urbach's second observation was a temperature dependence of the gradient of the linear regime of the logarithmic absorption coefficient. Reprinted with permission from Urbach, *Phys. Rev.* 1953, 92 (5). Copyright 1953 American physical society[31] **c)** The point at which the two constants α_0 and E_0 meet is the Urbach bundle as shown by Kurik. Reprinted with permission from Kurik, *Phys. Status Solidi* 1971, 8 (1). Copyright 1971 WILEY-VCH Verlag GmbH & Co. KGaA [32]

The dependence between the absorption coefficient and the photon energy and temperature yields:

$$\alpha(h\nu, T) = \alpha_0 \cdot exp\left[\frac{\sigma(h\nu - E_0}{k_B T}\right] = \alpha_0 \cdot exp\left[\frac{h\nu - E_0}{E_U}\right] \quad (2.25)$$

The extension of the linear fits of the absorption spectra at different temperatures converge to form a 'Urbach bundle' at the coordinates α_0 and E_0 as shown in Figure 2.13c. To determine whether a particular solid follows the Urbach rule, there should be a 'definite relation between the exponential parameters and the absorption temperature-dependence.[32] Correctly investigating both the exponential tail and its temperature-dependence, will allow an understanding of the reason behind absorption edge smearing, i.e. the Urbach tail. Cody has described the Urbach tail as being between the onset, where the optical transition is from a state deep in the bandgap, and the excitation of the VB electrons to the CB.[33] Figure 2.14a, shows how an electron in the VB, with the assistance of a phonon, can be excited by a photon with energy less the bandgap energy to the CB. Thomas *et al.* calculated and observed that the absorption of a phonon by an electron is based on the strength of electron-phonon (lattice vibrations) interaction. [18] Therefore, the number of possible combinations that will allow excitation of electrons from the VB to the CB will result in a change in the gradient of the Urbach tail. [34–38] The interaction between the electron and phonon and its determination of the Urbach Tail explains and holds with many different material systems and also explains the temperature-dependence of the E_u. [32,33,36,37,39] An increase in the local disorder in a lattice will lead to a formation of spatially separated local band-gaps throughout the lattice (Figure 2.14b),[40] and such changes will increase the absorption edge smear, leading to an increase in the value of E_u.

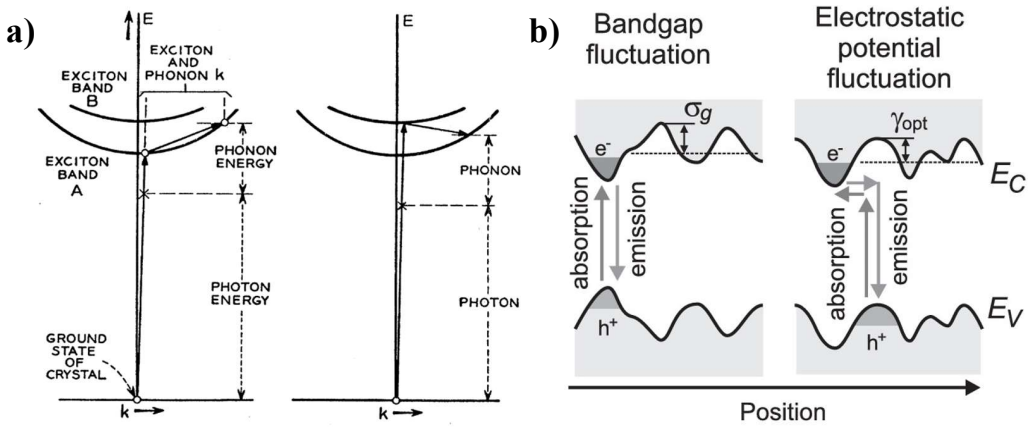


Figure 2.14: a) The excitation of an electron from the ground state to the 1st excited state via absorption of both a photon and a phonon. Reprinted with permission from Thomas *et al. Phys. Rev.* 119, 570 (1960) Copyright 1960 American Physical Society[34] **b)** The spatial bandgap fluctuations in a crystal due to disorder in a lattice. Reprinted with permission from Gokmen *et al. Appl. Phys. Lett.* **103**, 103506 (2013). Copyright 2013 AIP Publishing [40]

There are three main types of disorder in a solid: [41] temperature disordering, due to thermal lattice vibrations, [42–44] structural disordering induced by defects, vacancies, dislocations, stoichiometric imbalance, crystallinity[42,45] and compositional disordering [46,47] whereupon a change in composition induces a change in the E_u. At phase transitions, a significant change in the crystal structure of a semiconductor may occur. Around the phase transition temperature, the expansion or contraction of the lattice will lead to a significant disorder and stress throughout the lattice, hence the value of E_u will abruptly increase. [48,49] Figure 2.15 shows the effect of the different disorder types on the E_u.

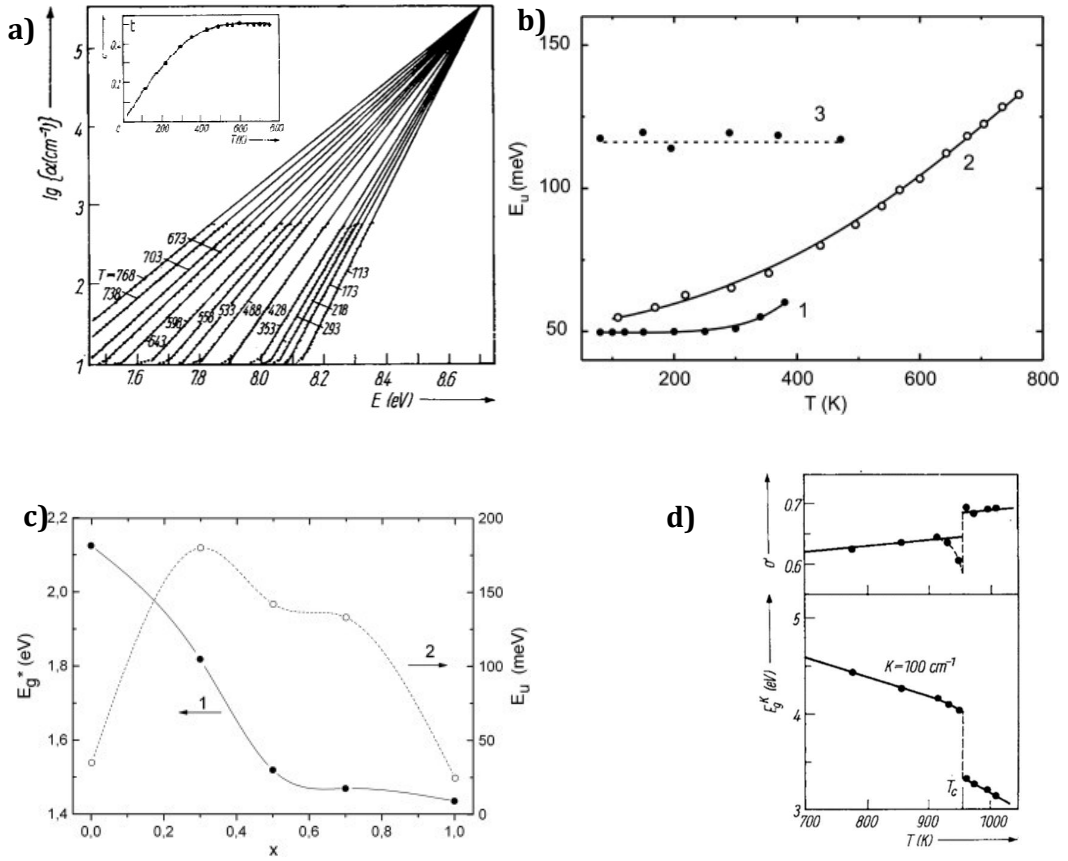


Figure 2.15 a) The temperature-dependent change in the Urbach energy of vitreous SiO_2 as observed by Godmanis *et al.* The inset shows the Urbach energy vs temperature. Reprinted with permission from Godmanis *et al. Phys. status solidi* 1983, 116 (1). Copyright 1983 WILEY-VCH Verlag GmbH & Co. KGaA [50] **b)** Changes in E_u due to materials with different static and dynamic disordering in 1) glassy As_2S_3 2) SiO_2 3) $20PbO{\cdot}80SiO_2$. Reprinted with permission from Kranjčec *et al. J. Non. Cryst. Solids* 2009, 355 (1), Copyright 2009 Elsevier B.V. [51] **c)** The change in chemical composition of $Cu_7Ge(S_{1-x}Se_x)_5I$ and the change in E_u. Reprinted with permission from Studenyak *et al. Solid-State Ionics* 2010, 181 (35–36). Copyright 2010 Elsevier B.V. [47] **d)** During a phase change induced by temperature the Urbach energy has shown a sudden jump in potassium iodide (KI). Reprinted with permission from Zametin, *Phys. status solidi 1984*, 124 (2). Copyright 1984 WILEY-VCH Verlag GmbH & Co. KGaA. [48]

2.4 Hybrid Metal-Halide Perovskite Photovoltaics

Hybrid metal-halide perovskites were first synthesised in 1978 by Dieter Weber, whose characterisation of the compound showed that the $CH_3NH_3PbI_3$ was a cubic perovskite structure (shown in Figure 2.16) with 'an intense color'.[52] Thereafter, in the late 1980's by Yamada *et al.* elucidated the crystal structure in more detail with a series of structural characterisation experiments. [53–55] Subsequently, in the 1990's Mitzi *et al.* explored the electrical properties of a variety of hybrid metal-halide perovskites and found that they exhibited properties akin to semiconductors. [56–59] In 1991, the versatility in fabrication techniques of hybrid metal-halide semiconductors and their desirable electrical properties allowed Kagan *et al.* to implement $(C_6H_5C_2H_4NH_3)_2SnI_4$ in field-effect transistors, the first such use of hybrid metal-halide perovskites semiconductors in an electrical device.[60] The first use of hybrid metal-halide perovskites semiconductors in a photovoltaic device was by Kojima *et al.*, where they used methyl ammonium lead triiodide ($MAPbI_3$) as a photoabsorbing layer in a dye sensitised solar cell. [9] Devices employing a mesoporous TiO_2 electron extractor layer yielded higher efficiencies of 12%,[61] leading to a realisation amongst scientists that methyl ammonium lead triiodide may be a suitable intrinsic semiconductor for photovoltaic devices. A breakthrough for perovskite based photovoltaic devices came by Lee *et al.* who discovered that $MAPbI_{3-x}Cl_x$ has charge-carrier transport properties that allow a device configuration without an n-type extractor layer. [10]

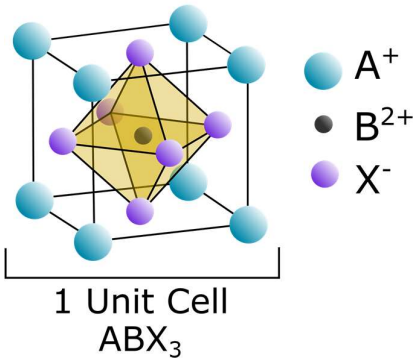


Figure 2.16 A unit cell of a perovskite crystal structure of the form ABX_3. Hybrid metal-halide perovskite semiconductors usually consist of an organic 'A site' cation, a Pb based 'B site' metal cation and a I and/or Br 'X site' halide anion. The hybrid metal-halide structure investigated in this thesis consists of $CH_3NH_3^+$ 'A site' cation, Pb 'B site' metal cation and I^- 'X site' anion. $CH_3NH_3PbI_3$, methyl ammonium lead triiodide perovskite, has a band gap of ~1.58 eV which is favourable for photovoltaic applications.

In 2013, Ball *et al.* first showed that $MAPbI_{3-x}Cl_x$ can be implemented into a planar heterojunction format, highlighting that the perovskite absorber was efficient at transporting both electron and holes to the respective n- and p- type contacts.[12] In 2014, Liu *et al.*, yielded a top PCE of 15.4% for a planar heterojunction device, using the technique of dual-source vapour deposition. [14] As a result of the facile solution processing required to create $MAPbI_3$ thin films, many investigators around the world have been able to investigate the photophysical properties of $MAPbI_3$. $MAPbI_3$ exhibits long charge-carrier diffusion length, relatively high charge carrier mobilities, long recombination lifetimes, all of which are surprising yet encouraging, considering that the thin films are processed usually in ambient conditions. [62–67] The fabrication technique used by Liu *et al*,[14,68] was vapour deposition, a technique which yields smooth and pinhole free thin films.[69,70,79–88,71–78] There are two main type of

vapour deposition techniques, the sequential method[83,84,89] and the co-evaporation method.[15,69–72,90,91] The co-evaporation method has so far yielded the highest performing $MAPbI_3$ based solar cell.[15] However, it requires very careful control of deposition rates to ensure that the final thin film consists of the correct stoichiometry. The sequential thermal evaporation method, where two precursors are deposited sequentially, whilst easier due to the step by step process, has not proved to yield the highest performing devices.[83] Understanding how $MAPbI_3$ perovskite forms from the precursors, methyl ammonium iodide and lead iodide, will allow for higher quality films with higher reproducibility both for vapour deposition techniques and solution processing techniques. In solution processed films, processing the perovskite film in the presence of different environmental conditions can lead to an increase in device PCE, however the precise influence of moisture compared to the solvent used in solution processing on the crystallisation process could not be deconvoluted. [92]

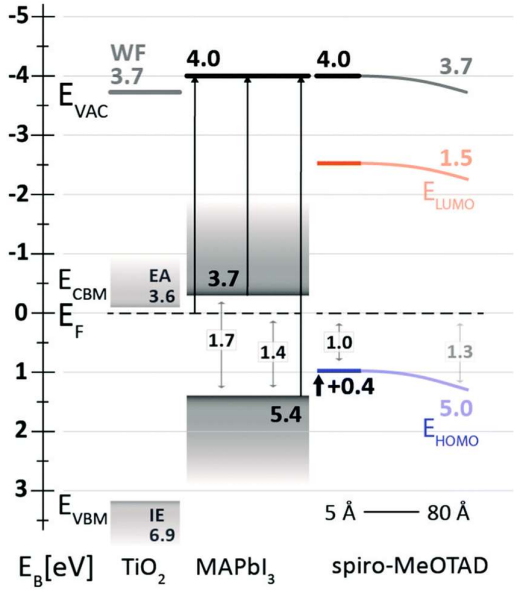


Figure 2.17. The interface energetics of the common semiconductors used in a $MAPbI_3$ *n-i-p* photovoltaic device. Reprinted with permission from Schulz *et al. Energy Environ. Sci.* 2014, 7 (4). Copyright (2014) Royal Society of Chemistry[93]

Early hybrid metal-halide devices suffered from current-voltage hysteresis, for which *J-V* curves showed different device characteristics if the device was biased from $J_{sc} \rightarrow V_{oc}$ (forward scan) and $V_{oc} \rightarrow J_{sc}$ (reverse scan).[94] Van Reenen *et al.* proposed a model and showed simulations on how a combination of both ion migration and defect density at the interface leads to hysteresis being observed in perovskite solar cells (Figure 2.18).[95] Van Reenen's model importantly highlighted that without any interfacial defects, hysteresis in the devices would not be observed. Calado *et al* proved it was important to have both mobile ions and trap sites at the interface of the perovskite thin film, for a device to show hysteretic behaviour.[96] The main results for ion migration under bias points towards iodine interstitials/vacancies as being the prime reason for migration of iodine when an electric field is applied.[97–101]

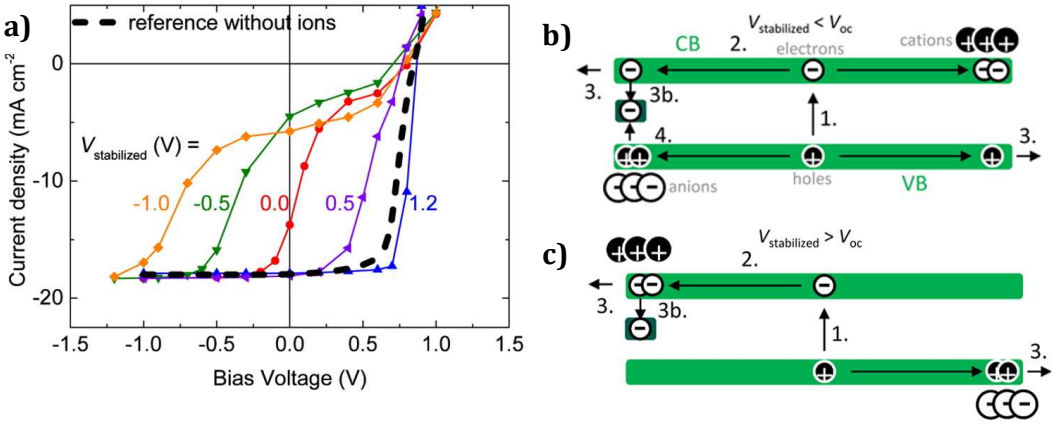


Figure 2.18: a) The effect of stabilising the device at different voltages, followed by a fast J-V sweep. The presence of trap sites at the interface leads to charge carried being trapped. **b)** When the anions have built up at the n-type extractor layer, leading to photogenerated holes diffusing towards them and allowing for recombination with trapped electrons **c)** The cations have moved towards the n-type layer, thus there is no effect in the photocurrent, as seen in the J-V curve. Reprinted with permission from van Reenen *et al. J. Phys. Chem. Lett.* 2015, 6 (19) Copyright (2015) American Chemical Society. [95]

Perovskite thin films can be deposited on an array of different substrates, such as flexible polymers, especially with thermal evaporation.[102] This makes perovskite thin films ideal for lightweight photovoltaic modules for use in extreme climates, such as space or vehicles. Moreover, Milot *et al.* have observed that the charge carrier-mobility of $MAPbI_3$ increases with decreasing temperature,[103] providing a further reason for $MAPbI_3$ as a suitable photoabsorber in lightweight solar cells for space applications where the required operating temperature is 173 K – 398 K. [104]

Over the past 4 years, the main change in the multilayer perovskite photovoltaic device has been the incorporation of organic charge transport layers. Fullerenes have proven to be vital in yield-high PCE perovskite devices as the LUMO of the fullerene has favourable energetic alignment with the CB of the $MAPbI_3$.[15,76,105–109] Furthermore the fabrication of fullerene thin films are facile and require common solvents such as chlorobenzene and have a low absorption coefficient, making them suitable to be used in both regular or inverted device architectures. [90,105] Apart from the favourable energetic alignment of fullerenes with the perovskite, little is known on the effect of organic semiconductors on the morphology of the ensuing perovskite thin film when employed in a regular device architecture compared with using metal-oxide transport layers.

2.5 Organic Photovoltaics

Another promising, albeit a more mature photovoltaic technology is based on organic semiconductors. The first application of organic molecules for use in photovoltaic devices was in 1979. Tang patented a multilayer photovoltaic device encompassing semiconducting organic molecules, which had achieved a PCE of 0.95%.[110] The planar heterojunction photovoltaic device consisted of a simple donor material copper phthalocyanine and an acceptor based on a perylene derivative. [111] The discovery of using organic semiconductors for photovoltaic materials was exciting as organic molecules can be synthesised, with fine control over their steric configuration and electronic properties.

However organic photovoltaics are exitonic at room temperature, meaning that they require both a donor material, usually the primary absorber, and an acceptor material. The interface between the donor and acceptor materials creates an energy offset allowing for the excitons to overcome the large binding energy E_b, which is of the order of ~100 meV. [112] Considering that the exciton diffusion length is of the order of 10-100 nm in organic semiconductors, a planar heterojunction architecture for organic photovoltaics is flawed as the thickness required for significant light absorption is significantly larger.[113] An architecture to overcome the limitations of a planar heterojunction architecture was pioneered by Hiramoto *et al.*[114] They created a mixture of the donor and the acceptor materials which was co-deposited onto the device as a film.

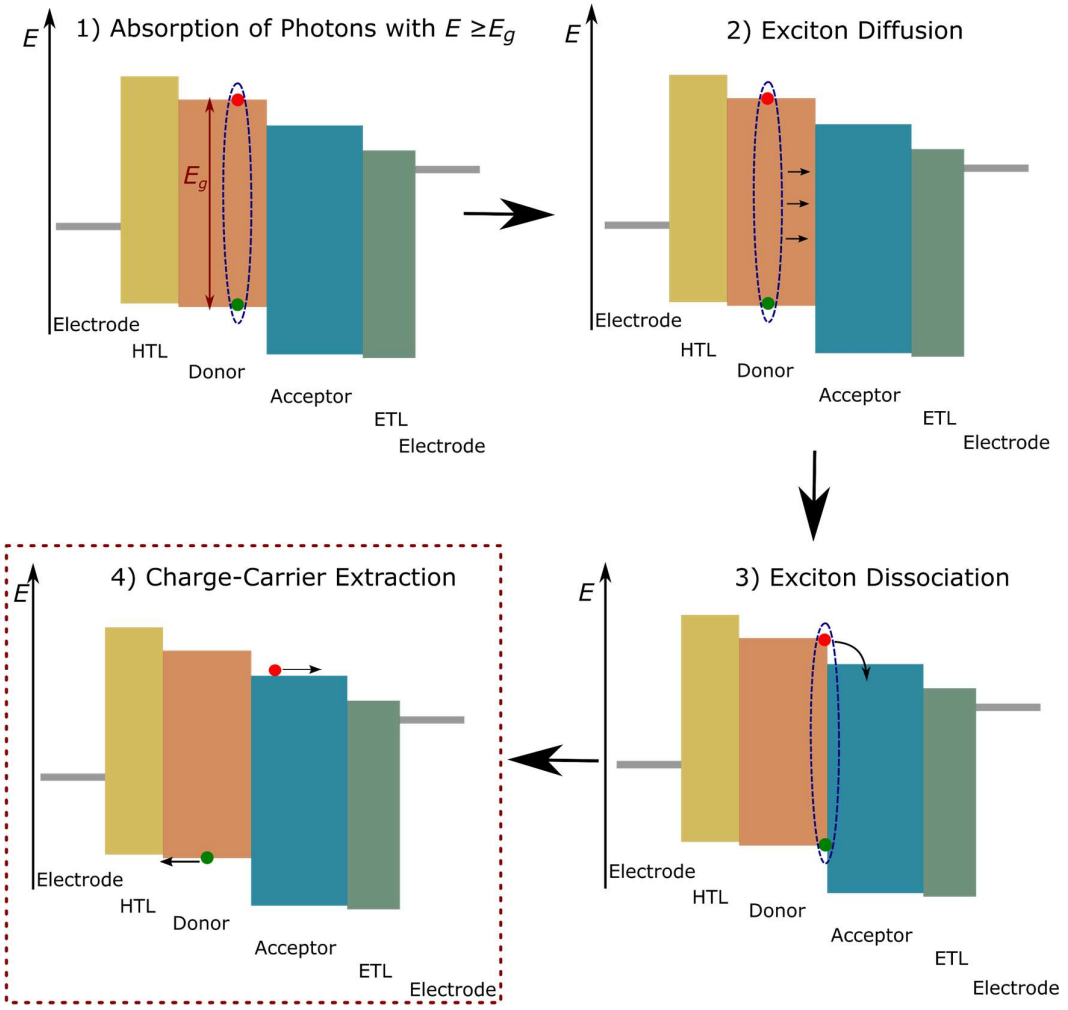


Figure 2.19. A typical energy level diagram of the various layers in an organic photovoltaic device. 1) Absorption of a photon leads to the formation of an exciton. 2) The exciton randomly diffuses in the material until reaching the heterojunction. 3) The energy offset between the donor and acceptor material is larger than the exciton binding energy, allowing the separation of the electron and hole into free charge-carriers 4) Extraction of free charge-carriers resulting in a photocurrent.

This approach started a period of research into organic semiconductor blend films, for which the acceptor and donor materials were dissolved jointly in one solution and then deposited on to the substrate to create a bulk-heterojunction film (Figure 2.20).[115,116]

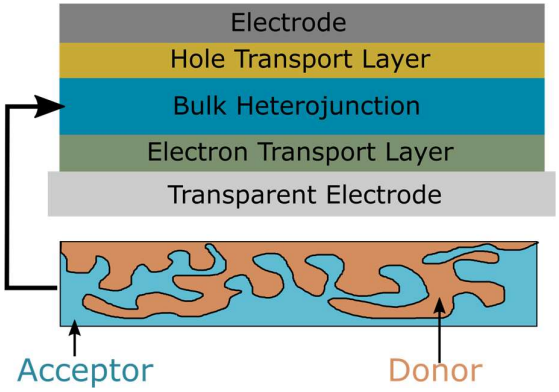


Figure 2.20. A schematic of the architecture of a prototypical bulk heterojunction device. The bulk heterojunction consists of an acceptor molecule, usually a fullerene, and a donor polymer.

Sariciftci *et al.* observed that fullerenes such as C_{60} created an ideal electron acceptor layer.[117] Fullerenes have proven to be a popular choice as an acceptor material, because of their simple processing requirements and favourable band alignment with the donor materials allowing for efficient charge transfer and maximising the open circuit voltage.[115,116] The profile of the interface between the donor and the acceptor material is crucial in a bulk heterojunction device. It allows for a large interfacial surface area, allowing excitons to be within the diffusion length of the interface.[118] In solution-processed organic photovoltaics devices, polymeric semiconductors can be synthesised and implemented in devices as the donor material based on their solubility, miscibility, absorption coefficient and band energetics. Polymers are desirable for use in industry as they can be produced in large batches with simple fabrication techniques. With side-group engineering of polymers, the morphology of the polymer in the bulk heterojunction can be controlled to maximise PCE of the photovoltaic device.[119]

The PCE of organic bulk heterojunction photovoltaics devices have shown considerable progress. Current state of the art PCE of solution process devices have reached 13%.[120] Furthermore, they have recently shown to utilise their novelty features of flexibility and semi-transparency to be used in aesthetically appealing modules in the form of solar trees.[121] However for organic photovoltaics to be key part of the long term solution to the increasing global energy demand, the stability of the devices must be improved. An advantage of utilising organic semiconductors for photovoltaics is that they can be molecularly engineered to have end/side groups that may prevent unwanted interactions and reactions with air and light. Hence it is paramount that there is a clear understanding of the degradation mechanisms of the key materials within the device to facilitate the design of new and more resilient organic semiconductors.

Chapter 3

Experimental Methods

This chapter presents the methods for fabrication and characterisation of both $MAPbI_3$ thin films and devices that have been utilised for the subsequent investigations discussed in this thesis.

3.1 Vapour Deposition

Two types of vapour deposition methods currently exist: a sequential deposition and a co-deposition method. In this thesis the sequential deposition method is reported to investigate the formation dynamics of $CH_3NH_3PbI_3$ perovskite. The second method, co-deposition, is the predominant technique used to fabricate thin films of $CH_3NH_3PbI_3$ for planar heterojunction photovoltaic devices.

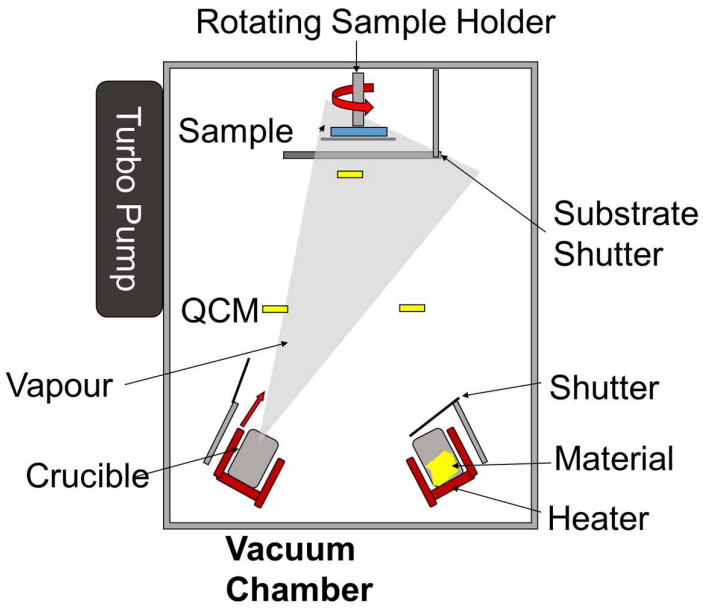


Figure 3.1 A diagram of the vacuum chamber used to fabricate the vapour-deposited $CH_3NH_3PbI_3$ and C_{60} thin films. The quartz crystal microbalance (QCM) consists of a 6MHz Quartz crystal with gold electrodes. The precursor materials are heated using a resistive heater.

The thermal evaporation chamber used for investigations reported in this thesis has two low temperature thermal sources which have their own independent shutters. There is also a third shutter covering the substrates, allowing for deposition on the substrate to occur only after the rates of evaporation have stabilised. The evaporation of materials is achieved due to the high vacuum

created in the chamber along with the heating of each precursor material in the ceramic crucibles. Figure 3.1 shows a schematic of the evaporation chamber used.

3.1.1 Sequential Deposition

A two-step thermal evaporation technique, modified to slow the reaction of PbI_2 and MAI, was used to grow bilayer films of PbI_2 and MAI on z-cut quartz, glass and KBr substrates under high vacuum. The tooling factor for the quartz crystal microbalance (QCM) was determined by deposition of the PbI_2 and MAI separately and subsequently the thickness of the individual thin films was measured using a DEKTAK 150 profiler. The QCM was also used to ensure that the final film had a 1:1 molar ratio by correlation of the density of the compounds with the thicknesses measured by an uncalibrated QCM.

300 mg of MAI and PbI_2 (ultra-dry 99.999% (metals basis), Alfa Aesar) were placed in separate crucibles, and the quartz, glass and KBr substrates were mounted on a rotating substrate holder to ensure that a uniform film was deposited. The chamber was pumped down to a base pressure of 10^{-6} mbar. The substrate temperature was kept at 21°C whilst the deposition of PbI_2 took place at a rate of 0.5 Å/s. After the desired thickness was deposited (200 nm), the substrate temperature was lowered to 0°C and kept at constant temperature for 30 minutes. To slow the reaction of PbI_2 and MAI, the substrate temperature was maintained at 0°C while MAI was deposited at a rate of 1.3 Å/s. The thickness of the layers deposited was 200 nm each, as measured by quartz crystal microbalance during the deposition. Once the deposition was completed,

the films were kept under high vacuum and at 0°C for 3 hours before being removed from the vacuum chamber.

3.1.2 Co-Deposition

The tooling factor was determined by deposition of the starting powders, PbI_2 (ultra-dry 99.999% (metals basis), Alfa Aesar) and MAI (Oxford Photovoltaics) separately, followed by measurement of the layer thicknesses with the DEKTAK surface profilometer. MAI and PbI_2 (500mg of each) were placed in separate crucibles, and the substrates were mounted on a rotating substrate holder to ensure that a uniform film was deposited. The temperature of the substrates was kept at 21°C throughout the deposition. The chamber was allowed to reach a high vacuum (10^{-6} mbar) before the PbI_2 and the MAI was heated. Once the deposition rate had stabilised along with the pressure ($3x10^{-6}$ mbar), the substrates were exposed to the vapour. The rates of both the MAI and PbI_2 were monitored using a quartz crystal microbalance to ensure a 1:1 molar ratio was achieved in the final composition of the film. The final thickness of the films was 300 nm (DEKTAK 150 profiler). Note that the excess materials left in the crucible could be used multiple times until none was left. Furthermore, QCM sensors needed to be changed every 3-4 depositions.

3.2. Thin-Film Characterisation

3.2.1 Ultraviolet-Visible Spectroscopy

Ultraviolet-visible spectroscopy (UV-vis) can illustrate the allowed electronic transitions that occur in materials with a band gap (E_g) where E_g is above ~1.6 eV. Based on the schematic in Figure 3.2, an electron in the valence band (VB) in a material or HOMO of a molecule can be excited by a photon with energy E_g to the conduction band (CB) of a material or LUMO of the molecule. When the incident photon energy is $E>E_g$, the electron can be excited to the continuum of energy states above the CB, thus yielding an absorption spectrum showing the electronic transition states in the ultraviolet-visible range.

The Beer Lambert law states the relationship between the incident intensity of radiation I_0, and the transmitted intensity I, through a thickness of a film d, is

$$I(\lambda) = I_0 10^{-\alpha(\lambda)d} \tag{3.1}$$

where α, is the absorption coefficient. A conventional method to plot the absorption of a film is using a dimensionless parameter absorbance, or optical density which is, [122]

$$A = -\log_{10}\left(\frac{I}{I_0}\right) = -\log_{10}\left(\frac{T}{1-R}\right) \tag{3.2}$$

where, A is the absorbance or optical density, T is the transmittance and R is the reflectance.

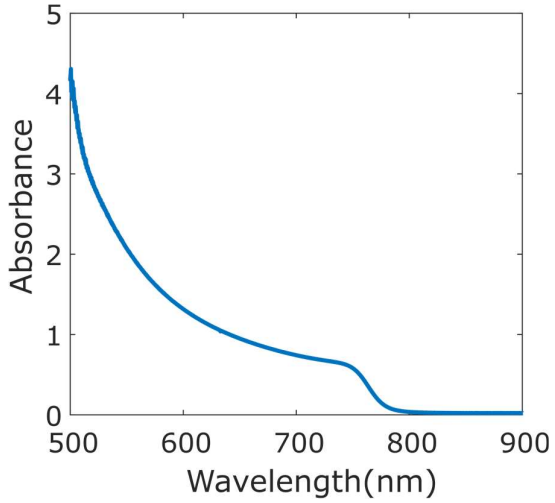


Figure 3.2. A typical visible absorption spectrum of a $CH_3NH_3PbI_3$ thin film. The onset at ~780nm corresponds to the photo excitation on an electron in the ground state to the 1st excited state, which corresponds to the E_g of the material.

Both the visible and mid-infrared spectra were measured using a Bruker Vertex 80v Fourier-transform infrared (FTIR) spectrometer fitted with a reflection/transmission accessory. Transmission and reflection measurements were taken using a Bruker Vertex 80v Fourier Transform Interferometer with a silicon diode detector and a tungsten halogen light as a near infrared source. Visible measurements were taken using a tungsten halogen lamp source and a xenon lamp was used as a UV light source with a silicon diode detector. Mid-infrared measurements were taken using a globar source and a nitrogen-cooled photovoltaic HgCdTe detector. Temperature-dependent measurements were carried out in an Oxford Instruments OptistatCF2 gas exchange helium cryostat.

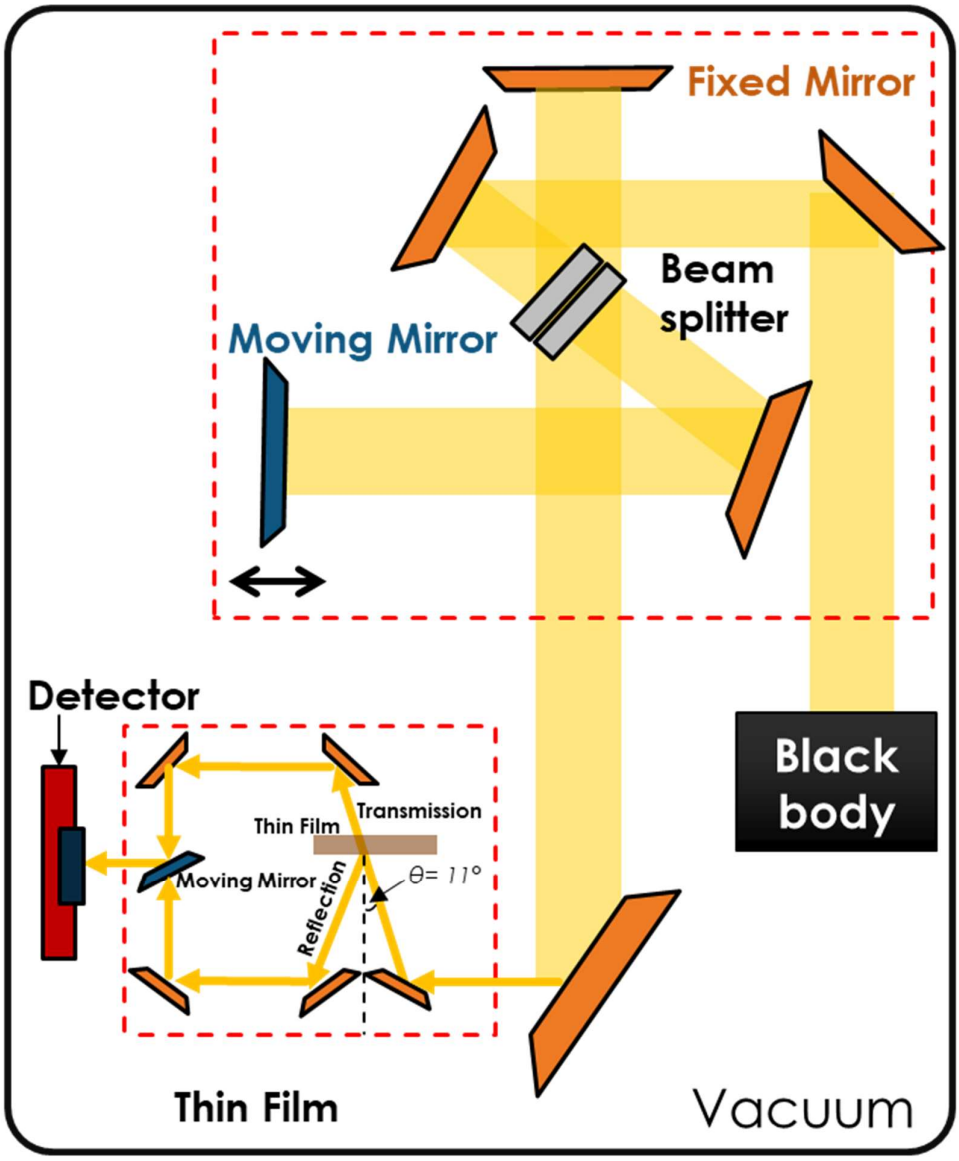


Figure 3.3. The Fourier transform Infrared spectroscopy setup to measure the transmission and reflection of thin films used in this study. The detector is changed according to the desired spectral range. (HgCdTe detector for mid-infrared measurements and Si diode for UV-visible spectral range). The angle of incidence from the normal on the sample was 11°.

3.2.2 X-ray Diffraction

X-ray diffraction involves irradiating a material with x-rays. The incident x-rays will penetrate the lattice and will be scattered because of the atoms in the unit cell. Based on the distance between lattice planes (d) the x-rays will constructively or destructively interfere. The x-rays which satisfy the Bragg's law, will constructively interfere and result in a reflection at that angle. Bragg's law states

$$n\lambda = 2d\ sin\theta \qquad 3.3$$

where θ is the diffraction angle, d is the interplanar spacing between the atoms and n is an integer. The intensity diffraction will reflect the overall crystallinity of the material. Figure 3.4 shows a schematic of the diffraction of X-rays in a crystal.

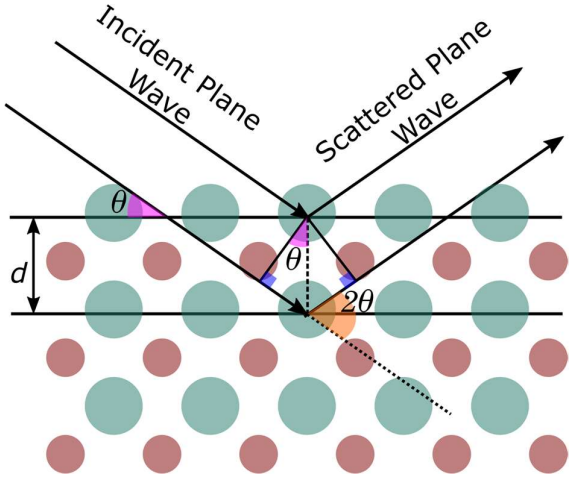


Figure 3.4. The diffraction of x-rays in crystal lattice. If the scattered waves follow Bragg's law then the waves will constructively interfere, resulting in a diffraction peak in the diffraction pattern which will correlate with the distance d and hence the size of the unit cell.

2θ measurements were performed using an X-ray diffractometer (Panalytical X'Pert Pro). The scan speed was 0.02 °/s for 30 minutes (Cu-Kα radiation

operating at 40 kV and 40 mA). The diffraction patterns were corrected against tilt using quartz as a reference peak (2θ=16.43°) and were fitted using the pseudo-Voigt profile fit function on X'pert Highscore software. The bilayer samples were kept in a polyimide seal which slowly let in ambient air and left in the same position for 30 hours to ensure that the same area of the film was characterised.

3.3 Device Fabrication

All materials were bought from Sigma Aldrich, unless stated otherwise.

3.3.1 Substrate Cleaning

Fluorine doped tin Oxide (Pilkington) substrates were cleaned with hellmanex solution, followed by a rinse with distilled water. The substrate was then twice washed with Acetone, Isopropanol, and Ethanol. Thereafter the substrates were treated in O_2 plasma for 10 minutes.

3.3.2 Depositing Charge Transport Layers

The following section describes in detail the deposition parameters used for the deposition of charge transport layers for the fabrication of the device architectures shown in Figure 3.5.

Type A

TiO_2 was prepared as reported by Liu *et al*[91]. Titanium isopropoxide was dissolved in anhydrous ethanol solution followed by a proportional addition of 0.02 mol HCl. The solution was then spin coated on the FTO substrate at 2000rpm for 45 seconds in air. This step was followed by high-temperature sintering (500°C) for 45 minutes in air. $MAPbI_3$ was deposited by thermal co-

evaporation (see below). The films were annealed at 100°C for 60 minutes. Thereafter, spiro-OMeTAD was dissolved in chlorobenzene (8%wt) with added tert-butylpiridine (tBP) and lithium bis(trifluoromethanesulfonyl)imide (Li-TFSI). The solution was spin coated at 2000 rpm for 45 seconds in a nitrogen filled glovebox.

Type B

The fullerene, C_{60}, was spin coated as reported by Wojciechowski *et al.*[105] Briefly C_{60} (Solenne b.v. 99.5%) was dissolved in 1,2-dichlorobenzene (DCB), 10mg/ml, and then spin coated at 1500 rpm in air. After drying for 2 minutes at 55 °C, the substrates were taken into the nitrogen-filled glovebox. $MAPbI_3$ was deposited by thermal co-evaporation (see above). The films were annealed at 100 °C for 15 minutes. Thereafter spiro-OMeTAD was deposited inside the glove box as mentioned above.

Type C

A stock solution of $TiCl_4$ solution was prepared by Nobuya Sakai as reported by Sakai *et al.*[123] The FTO stubstrates were immersed into a bath of 20mM aqueous $TiCl_4$ and left in an oven set at 70°C for 60 minutes. PCBM (Solenne b.v. 99.5%) was dissolved in dichlorobenzene in either a 7.5 mg/ml or 15 mg/ml solution to get thickness of 50nm or 100nm respectively. The solution was then spin coated at 2000 rpm for 45 seconds. $MAPbI_3$ was deposited by thermal co-evaporation (see above). The films were annealed at 100 °C for 15 minutes. Thereafter spiro-OMeTAD was deposited as mentioned above.

Type D

F4-TCNQ doped Poly TPD (1-material) was spin coated at 2000 rpm for 45 seconds.[124] The samples were heated for 10 minutes at 100 °C. $MAPbI_3$ was

deposited by thermal co-evaporation (see below). The films were then annealed for 60 minutes at 100 °C. PCBM was dissolved in DCB, at a concentration of 10mg/ml, followed by spin coating at 1000 rpm. The substrates were heated for 10 minutes at 100 °C. A thin buffer layer of bathocuproine (BCP) dissolved in isopropanol was spin coated at 6000 rpm.

Type E

PCBM (Solenne b.v 99.5%) was dissolved in DCB in a 7.5 mg/ml solution to obtain a 50nm thickness. The solution was then spin coated at 2000 rpm for 45 seconds. $MAPbI_3$ was deposited by thermal co-evaporation. The films were annealed at 100°C for 15 minutes. Thereafter spiro-OMeTAD was deposited as mentioned above.

Type F

Spiro-OMeTAD was dissolved in chlorobenzene (8% wt) with added tBP and Li-TFSI and spin coated at 2000 rpm for 45seconds. $MAPbI_3$ was deposited by thermal co-evaporation. The films were then annealed for 60 minutes at 100 °C PCBM dissolved in DCB, 10 mg/ml, followed by spin coating at 1000 rpm. The substrates were heated for 10 minutes at 100 °C. A thin buffer layer of bathcuproine (BCP) dissolved in isopropanol was spin coated at 6000 rpm.

3.3.3 Evaporation of Metal Contacts

Silver contacts of 70 nm thickness were thermally evaporated with the use of a shadow mask. The base pressure was allowed to reach 10^{-6} mbar before the evaporation was initiated. The evaporation rate was set 0.5 $Å s^{-1}$.

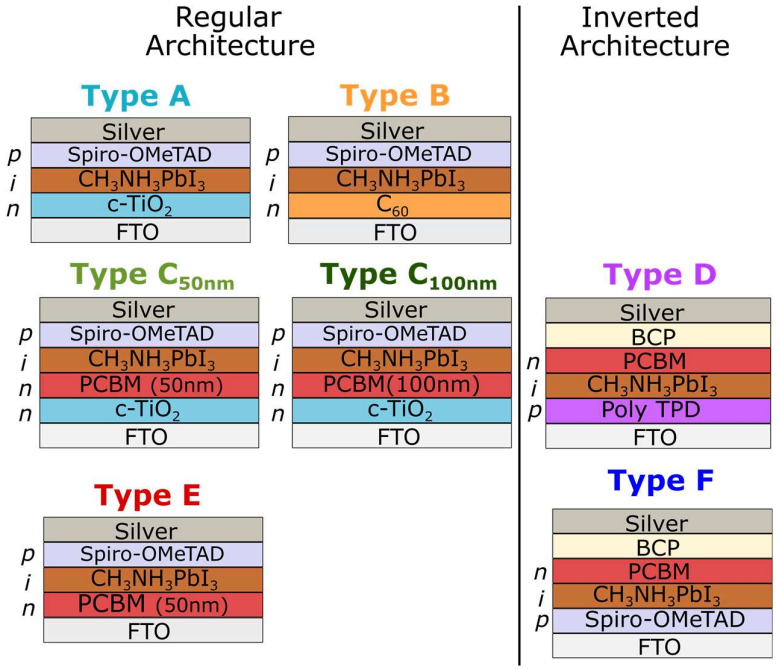


Figure 3.5. The complete set of $CH_3NH_3PbI_3$ based photovoltaic device architectures described in this thesis.

3.4 Device Characterisation

3.4.1 Current-Voltage Characterisation

The solar cells were measured under simulated AM1.5, 100mW cm^{-2} sunlight (1sun), ABET Technologies Sun 2000, and a Keithley 2400 sourcemeter in ambient conditions. The lamp was calibrated with a NREL-calibrated KG5 filtered silicon reference. The active area of each device was defined by a mask which exposed the device to a 0.0919cm^2 active area for testing of both the current-voltage measurements and the stabilised power measurements. The scan rate was 0.38 V s^{-1} for both the reverse and forward sweep for all the devices measured. The devices were kept at the voltage defined at maximum power, which was determined from the *J-V* scans, for 50 seconds to measure the SPO and current density.

3.4.2 Fourier Transform Photocurrent Spectroscopy (FTPS)

Temperature-dependent FTPS

Photocurrent was measured via a custom-built Fourier transform photocurrent spectrometer based on a Bruker Vertex 80v Fourier Transform Interferometer. Devices were illuminated with a tungsten halogen light source. The solar cells were masked with a metal aperture, with a defined active area of 0.0625 cm^2. A current preamplifier, Stanford Research 570, was used to detect low currents. For the temperature-dependent measurements, the solar cell was placed on a copper cold finger that included two sensors, one at the tip and one in the middle. This arrangement allowed for accurate recording of the temperature. All the photocurrent measurements were carried out in vacuum.

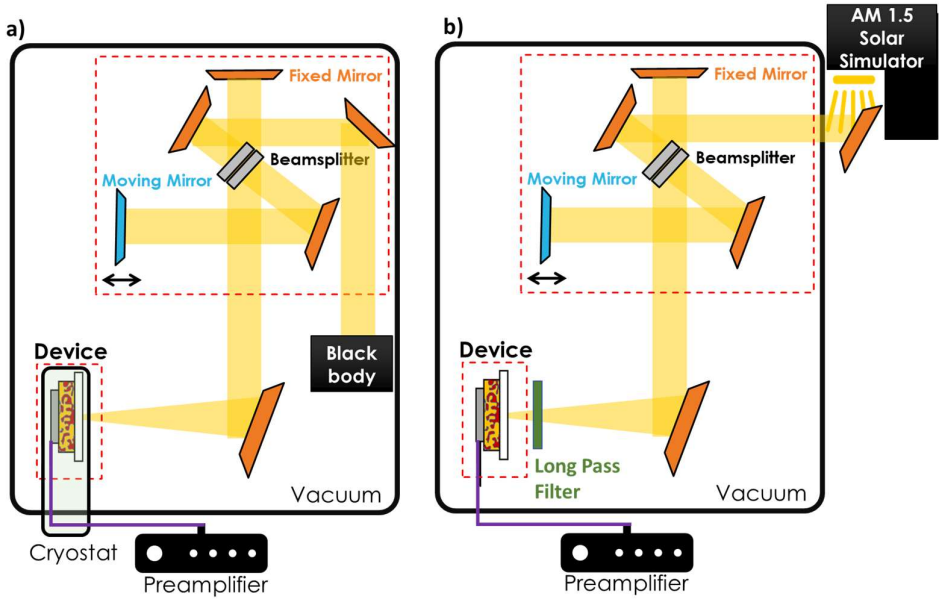


Figure 3.6 a) A schematic depicting the temperature-dependent Fourier transform photocurrent spectroscopy setup **b)** The External quantum efficiency measurement setup. The setup was used to look at the stability of the organic photovoltaic devices.

External Quantum Efficiency

The external quantum efficiency (EQE) was measured via a custom-built Fourier transform photocurrent spectrometer based on a Bruker Vertex 80v Fourier Transform Interferometer. Devices were illuminated with an 0.7 sun (70mW cm^{-2}), AM1.5 spectrum generated by an Oriel class AAA solar simulator. The solar cells were masked with a metal aperture, with a defined active area of 0.0625 cm^2. All the photocurrent measurements were carried out in vacuum. A long Pass (LP) glass filter of thickness 3 mm with onset at 331 nm (331-GY H-BaK7 Barium crown glass, Comar Optics) and a 3-mm thick LP 400 nm (GG-400 Schott glass, Thorlabs) were placed at a distance of 40 mm in front of the device to filter either UVB ($280 \leq \lambda < 315$ nm) or UVB+UVA ($315 \leq \lambda < 400$ nm) ultraviolet radiation from the AM1.5 spectrum generated by the solar simulator. The filter transmission curves and the spectrum of the solar simulator are shown in Figure 3.7. In the absence of long pass filters, the light was deemed "unfiltered" from UV light, meaning that devices were exposed to the standard AM1.5 spectrum generated by the solar simulator and the UV light this contains. To calculate the external quantum efficiency (EQE) the device photocurrent spectrum was divided by a calibrated silicon reference cell spectrum with a known EQE. The acquisition time for each spectrum was 110 seconds.

Urbach Energy

The Urbach energy was determined from the EQE which was obtained by processing the photocurrent data and using a calibrated silicon solar cell with a known EQE as a reference. A non-linear regression was performed using MATLAB to extract the Urbach energy from the EQE data. Robust fitting was

performed using a bisquared (Tukey's biweight) weighting function. We calculated a 95% confidence interval for the Urbach energy using the residuals and Jacobian of the fit.

$$\eta = \eta_0 \, e^{\frac{h\nu - E_0}{E_U}} \tag{3.1}$$

where η is the EQE, $h\nu$ is the photon energy and E_U is the Urbach energy and η_0 and E_0 are constants. Equation 3.1 shows the determination of the Urbach energy from the tail of the band edge determined by the EQE.

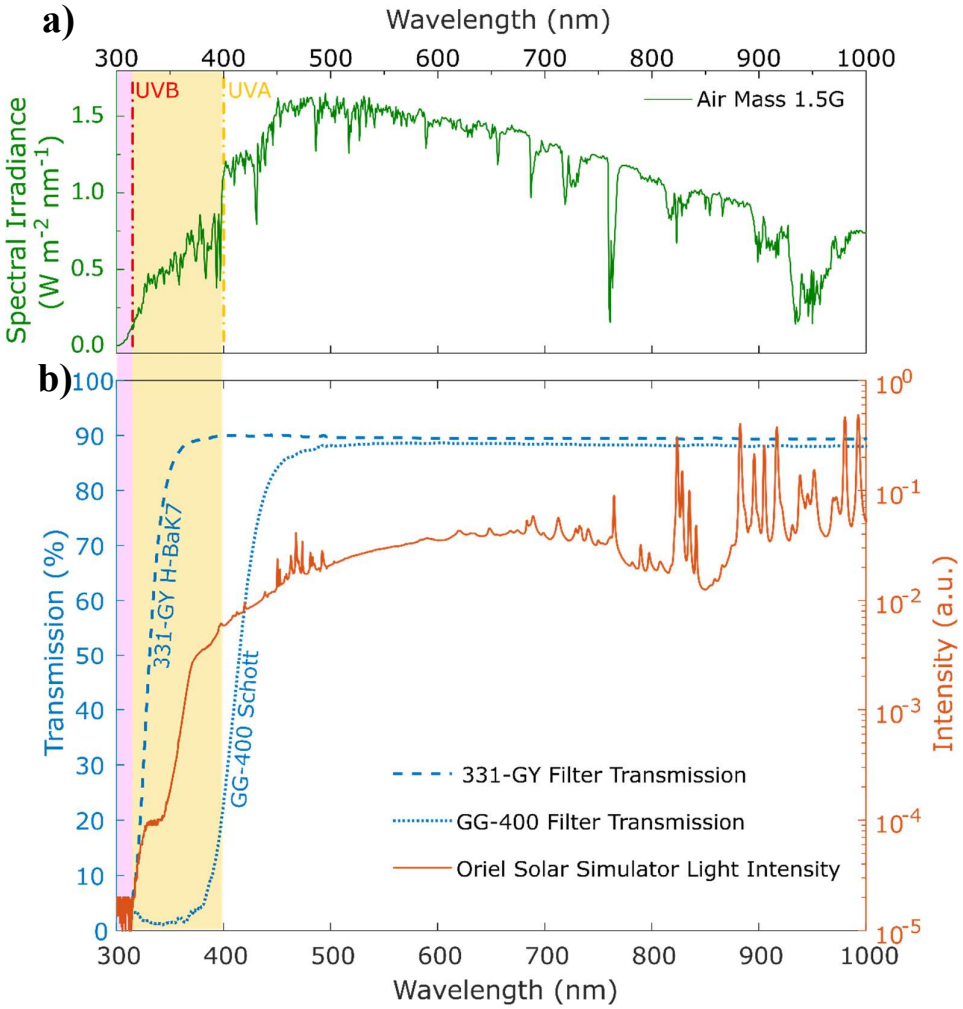


Figure 3.7 a) Air Mass 1.5G solar spectrum, plotted using data accessed from nrel.gov.[125] The dashed lines denote the cut-off for the two categories of UV radiation found in the AM 1.5 solar spectrum, UVB ($280 \leq \lambda < 315$ nm) and UVA ($315 \leq \lambda < 400$ nm) **b)** The transmission spectrum of the long pass 331nm filter (H-BaK7 331-GY, Comar optics) used in this investigation to filter UVB radiation, and the transmission spectrum of the long pass 400 nm filter (Schott Glass GG-400, Thorlabs) that was used to filter UVB +UVA radiation, together with the simulated unfiltered AM 1.5 light spectrum (red line) generated from the Oriel class AAA solar simulator with 0.7 sun ($70 mW cm^{-2}$) intensity.

3.4.3 Electroluminescence Spectroscopy

A bias voltage was applied to the photovoltaic device, using a Keithley 2450 sourcemeter. Electroluminescence was collected into an optical fibre coupled to a grating spectrometer (Princeton Instruments, SP-2558) and detected using a silicon CCD, acquiring spectra with an integration time of 60 seconds. The data was then corrected for the spectral response of the detector using a blackbody calibration lamp. The data was fitted with a Gaussian function using MATLAB.

3.4.4 Scanning Electron Microscopy

Images were taken using a Hitachi S-4300 microscope using 3kV accelerating voltage and 9 μA emission current. The substrates were coated with 3 nm of platinum using a Peltier-cooled sputter coater. The detection method used was secondary electron detection. Secondary electron detection mode involves detecting electrons which are emitted from the sample, that were initially inelastically scattered, from the sample surface by the incident electron beam.

3.4.5 Transmission Electron Microscopy

Transmission electron microscopy (TEM) of the perovskite solar cells were carried out and by *Jenny Wong-leung*. TEM samples of the devices were prepared by focused ion beam (FIB) using a Ga beam in a FEI Helios 600 NanoLab instrument. These samples were transferred onto a TEM carbon grid. TEM analysis was carried out in a JEOL2100F instrument operated at 200 keV and equipped with STEM capabilities and a silicon drift detector for EDX analysis. the sparse C intensity throughout the images are a result of the C grid used as support for the TEM sample.

Chapter 4

Formation Dynamics of $CH_3NH_3PbI_3$ Perovskite Thin Films

Little is known about the chemical transformations that occur in the initial stages of perovskite crystal formation. In the study presented in this chapter, the real-time formation dynamics of $MAPbI_3$ from a bilayer of lead iodide (PbI_2) and methylammonium iodide (MAI) deposited through a two-step thermal evaporation process is investigated. Lowering the substrate temperature during deposition initially inhibits intermixing of the two layers. Using infrared and visible light transmission, X-ray diffraction and photoluminescence lifetime measurements, the room-temperature transformations that occur in vacuum and ambient air, as MAI diffuses into the PbI_2 lattice to form $MAPbI_3$ is revealed. In vacuum, the transformation to $MAPbI_3$ is incomplete as unreacted MAI is retained in the film. However, exposure to moist air allows for conversion of the unreacted MAI to $MAPbI_3$, demonstrating that moisture is essential in making MAI more mobile and thus aiding perovskite crystallisation.

4.1 Introduction

The growth and processing conditions of the perovskite films can greatly affect the PCE of the resultant photovoltaic devices. For example, it is well-established that annealing methylammonium lead iodide ($MAPbI_3$) films causes more crystalline, uniform films, which enhances the PCE and the general stability of the film. [126] Yet recently evaporation techniques have shown that annealing is not mandatory to achieve highly crystalline films. [127] Similarly, it has been observed that thermally annealing a film in humid environments can have a positive effect on film morphology, crystallinity of the film and device performance. [128,129] However, such exposure of $MAPbI_3$ films to moisture has to be carefully balanced as prolonged periods lead to the formation of lead iodide and hence decomposition of the film.[130] Additionally, moisture in the precursor solutions and in the atmosphere can have a large influence on the crystallinity of the $MAPbI_3$ film and consequently the attainable PCEs. [131–133] Another wide parameter space is opened by sequential layer deposition, with the quality of the subsequently formed perovskite depending on temperature and fabrication conditions. [131,134]

These examples illustrate that the optimisation of $MAPbI_3$ film quality and stability crucially relies on an improved understanding of the chemical and structural transformations that occur during the initial interaction between PbI_2 and MAI. However, investigations of such film formation dynamics have been hampered by the fast interconversion dynamics of PbI_2 with MAI. In the study presented here, this process has been slowed down by depositing, through thermal evaporation, a thin layer of MAI on an existing layer of PbI_2 at

sufficiently low temperature to initially inhibit interdiffusion. After heating of the dual-layer film to room temperature, formation dynamics of $MAPbI_3$ in real time is investigated. By following the processes occurring first in vacuum it is identified that there is the formation of a nascent $MAPbI_3$ perovskite structure burdened with excess MAI that detriments the film's optoelectronic properties. The subsequent exposure of the film to ambient (humid) air initiates the disappearance of excess MAI and enhances crystallinity.

The films were prepared using a two-step thermal evaporation technique optimised to slow the reaction of PbI_2 and MAI during deposition. Lead iodide was evaporated on KBr, glass and z-cut quartz substrates held at 21°C which were then cooled to 0°C before MAI was evaporated onto the PbI_2 film. It was essential that both before and during the deposition of the MAI, the temperature of the substrate was kept at 0°C so that the diffusion of MAI into the PbI_2 layer was minimised prior to measurements commencing. Samples were subsequently investigated at room temperature, which initiated the intermixing of components. PL lifetimes and visible and IR absorption data were initially taken in vacuum to monitor the changes in the film in the absence ambient air. After 44 hours, the films were then exposed to air, which introduced moisture to the film. Since XRD measurements under vacuum were not possible in the system, the films were sealed with Kapton® polyimide sheets here to slow the exposure to ambient air. Further, more detailed experimental details can be found in Chapter 3.

4.2 Results and Discussion

Figure 4.1 displays the dynamic evolution of IR and visible absorption features of MAI/PbI_2 bilayers following the commencement of interdiffusion in vacuum and subsequent exposure to ambient air. Whilst the bilayers are in vacuum, the most dramatic changes occur in the visible absorbance spectrum (Figure 4.1A). Within the first 2 hours, the PbI_2 absorbance band edge (520nm) disappears, and the MAPbI3 band edge begins to establish itself near 750 nm. [135] These changes indicate that the MAI slowly diffuses across the PbI_2 layer and completely disrupts the layered arrays of I-Pb-I (where the stacking arrangement is in the form of a 2 hexagonal-polytype). [136] As a result, the formation of the three-dimensional (3D) $MAPbI_3$ perovskite structure is initiated. Even after the disappearance of PbI_2, however, the $MAPbI_3$ band edge continues to sharpen and red-shift, and overall absorption increases above the band edge. After 24 hours, the $MAPbI_3$ band edge is clearly defined, and no further spectral changes are observed. While changes in the content of PbI_2 and $MAPbI_3$ leave clear features in the UV/VIS absorption spectra, the presence of MAI cannot be as easily inferred because it does not feature significant absorption in this spectral region. IR spectroscopy (Figure 4.1C) provides valuable insight into the different chemical environments MAI experiences inside the 3D perovskite cage through the vibrational modes associated with the $CH_3NH_3^+$ (MA^+) bonds. [137]

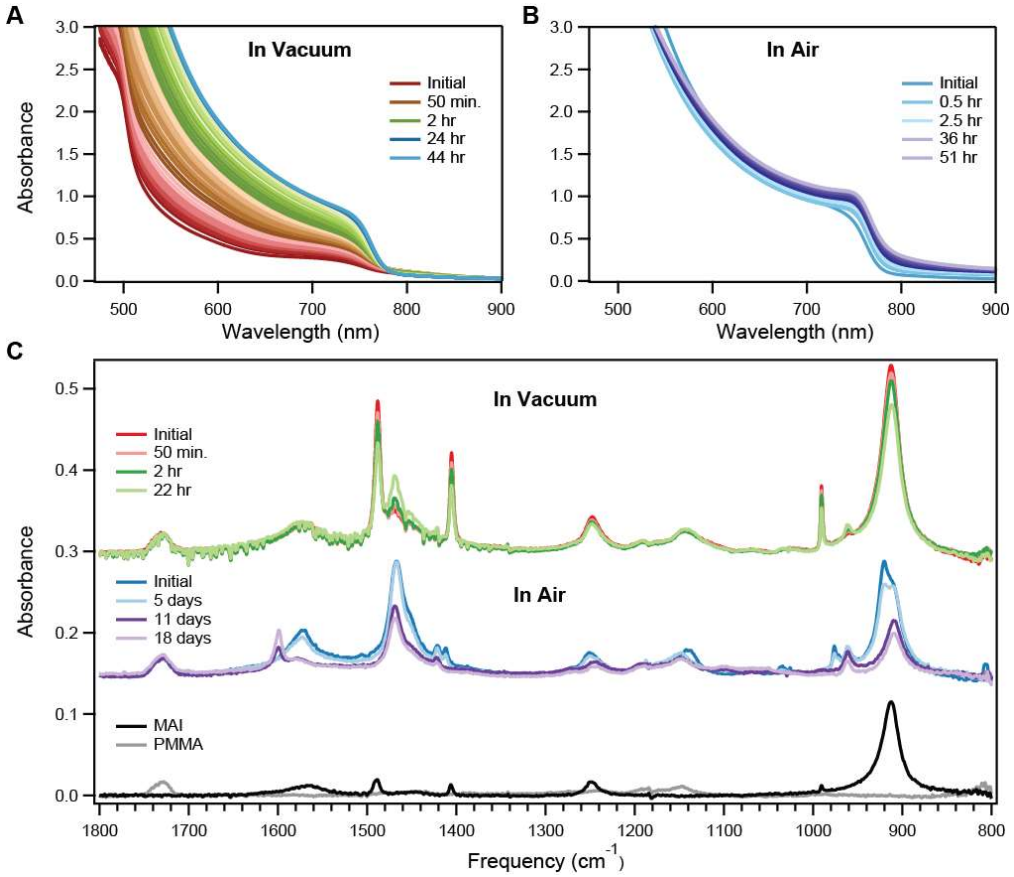


Figure 4.1. Visible and IR transmission spectra of an initially deposited bilayer MAI/PbI_2 as a function of time. Spectra were taken immediately following heating to room temperature (21°C±1°C) which initiates the formation of $MAPbI_3$ from MAI and PbI_2. **(A)** Changes in absorbance in the visible region for films under vacuum, taken for the initial bilayer MAI/PbI_2 (darkest red line), through the progression to a nascent $MAPbI_3$ perovskite structure over a period of 44 hours (lightest blue line). **(B)** Changes in absorbance in the visible region following the subsequent exposure of the film to ambient air. **(C)** IR transmission spectra for the bilayer MAI/PbI_2 (red line), the nascent $MAPbI_3$ perovskite structure formed in vacuum (light green line), and the more crystalline $MAPbI_3$ following exposure of the film to ambient air (blue line). Assignments of peaks in the IR spectra are provided in Table 1.

Initially, the IR spectrum closely resembles the spectrum for an evaporated film of MAI, and little change is observed in the first 50 minutes. After 50 minutes,

however, the incorporation of MAI into the $MAPbI_3$ structure becomes evident from changes in the IR signatures. The vibrations associated with the symmetric NH_3^+ and CH_3 bend (1490cm^{-1} and 1407cm^{-1}, respectively) in the MAI slowly decrease in intensity, and new peaks corresponding to the same vibrational modes in $MAPbI_3$ begin to form at 1468 cm^{-1} and 1422 cm^{-1} (Table 1). At higher energies, a similar transformation occurs: The C-N stretching vibration of MAI at 990 cm^{-1} decreases in intensity while the $MAPbI_3$ peak intensity at 960 cm^{-1} increases. Notably, not all of the initial vibrational modes associated with MAI shift. As can be seen in Table 1 the asymmetric (E) NH_3^+ bend and the NH_3^+ rocking vibrational modes occur at near identical frequencies in MAI and $MAPbI_3$. [138]

Comparison of IR modes				
Mode/ Symmetry	Classification	Frequency (cm^{-1})		
		MAI[a]	$MAPbI_3$[b]	Dihydrate
ν_9 / E	asym. NH_3^+ bend	1569	1574	1573
ν_3 / A_1	sym. NH_3^+ bend	1490	1468	1466
ν_{10} / E	asym. CH_3 bend	1450	1451	1453
ν_4 / A_1	sym. CH_3 bend	1407	1422	1413 1422
ν_{11} / E	NH_3^+/CH_3 rock	1251	1252	1255
ν_5 / A_1	C-N stretch	990	960	977
ν_{12} / E	NH_3^+/CH_3 rock	912	910	922

[a] Mode assignment were made using Reference[139].

[b] Mode assignments were made using Reference[137].

Table 1. Assignment of infrared (IR) active modes in MAI, $MAPbI_3$ and the dihydrate $(CH_3NH_3)_4PbI_6 \cdot 2H_2O$

After ~22 hours of interconversion in vacuum, no further changes are evident in either the IR spectrum (Figure 4.1C) or the UV/VIS absorbance spectra (Figure 4.1A). However, the IR signatures show that at this stage remnants of

MAI-specific peaks are still present, suggesting that a significant amount of MAI has not been incorporated into the $MAPbI_3$ perovskite structure, despite the 1:1 ratio of PbI_2:MAI in the initial bilayer film. This may indicate that there are local areas of excess of MAI within the film. Figure 4.2 shows the IR spectra of a film that was stored in pure nitrogen (<1ppm O2, <1ppm H2O) for 30 days.

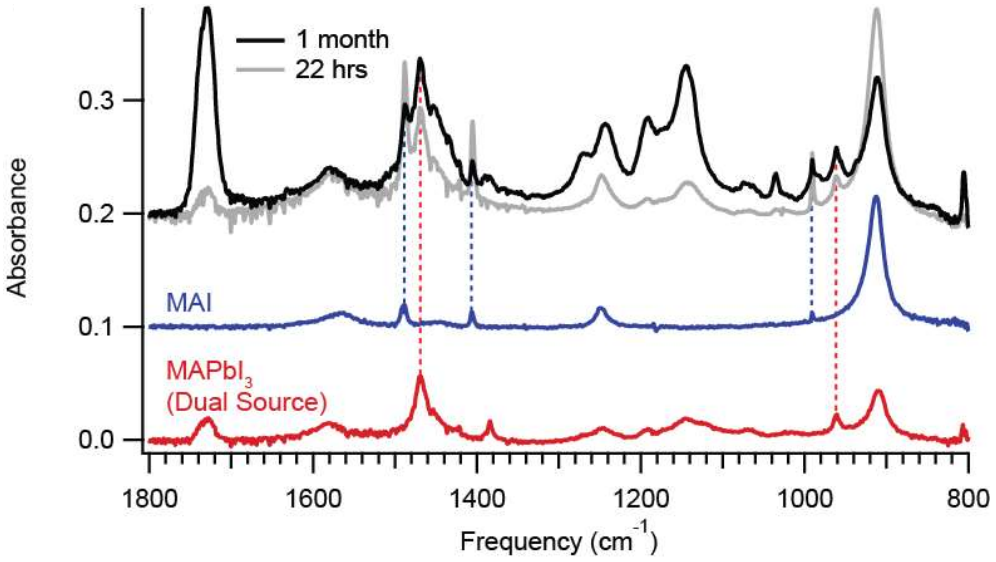


Figure 4.2. IR spectra of the bilayer films kept in vacuum for 22 hours compared with those for a bilayer film kept in a glovebox (<1 ppm O_2, <1 ppm H_2O) for 1 month. Minimal changes are observed, indicating that without a helper molecule such as H_2O, the final $MAPbI_3$ will not form.

There are still visible signs of MAI within the film, as can be seen by the presence of the C-N stretch mode at 990cm^{-1}, thus complete conversion to $MAPbI_3$ has not occurred. Therefore, it is clear that the composition of the film in vacuum is still in a nascent perovskite state despite the well-defined band edge in the visible spectrum and the complete disappearance of all PbI_2 spectral features. These results further support the notion proposed by Yang *et al.* that perovskite formation is accompanied by the complete breakdown of two

dimensional PbI_2 occurring as a result of MAI infiltration that is then followed by reorientation of MA^+ cations to consequently form the three-dimensional $MAPbI_3$ structure. [140]

To explore the role of moisture on the film formation and MAI content, films were exposed to ambient air (21°C±1°C, relative humidity=40%±10%) after they had reached a steady state under vacuum. As can be seen in Figure 4.1B, moisture only causes relatively subtle changes in absorption near the band edge, including a sharpening and slight red shift with time. As discussed below, these changes can be understood in terms of an enlargement of crystalline domains. The IR spectra, on the other hand, reveal significant rapid changes upon the exposure to moist air (Figure 4.1C). The peaks associated with the C-N stretch and the symmetric CH_3 and NH_3^+ in MAI ($990cm^{-1}$, $1450cm^{-1}$ and $1569cm^{-1}$ respectively) disappear, and only peaks associated with the MA^+ cation within the perovskite are observed, indicating that all of the MAI has rapidly converted. However, at the same time, additional peaks appear at $1415cm^{-1}$ and $975cm^{-1}$ near the symmetric (A_1) CH_3 bend and the C-N stretch which are known to be highly sensitive to hydrogen bonding of MA^+.[138,141]

Both monohydrate crystals ($CH_3NH_3PbI_3 \cdot H_2O$) and dihydrate films ($(CH_3NH_3)_4PbI_6 \cdot 2H_2O$) were synthesised to investigate the incorporation of water into the perovskite structure. [142,143] It was found that the dihydrate (Figure 4.4) exhibited similar IR features at $1415cm^{-1}$ and $975cm^{-1}$. The dihydrate forms through hydrogen bonding between water and the ammonium constituent of MAI, which causes a distorted NaCl-type crystal structure.[144] Furthermore dihydrates form readily in ambient conditions if there is an excess of MAI in the perovskite film[145] because of the hygroscopic nature of MAI.[146,147]

Therefore, it is proposed that the initial interdiffusion of PbI_2 and MAI in vacuum leads to the formation of nascent $MAPbI_3$ with remnant unreacted MAI. Upon exposure to air, moisture aids the ion diffusion of MAI leading to formation of $MAPbI_3$ and the dihydrate $(CH_3NH_3)_4PbI_6 \cdot 2H_2O$.

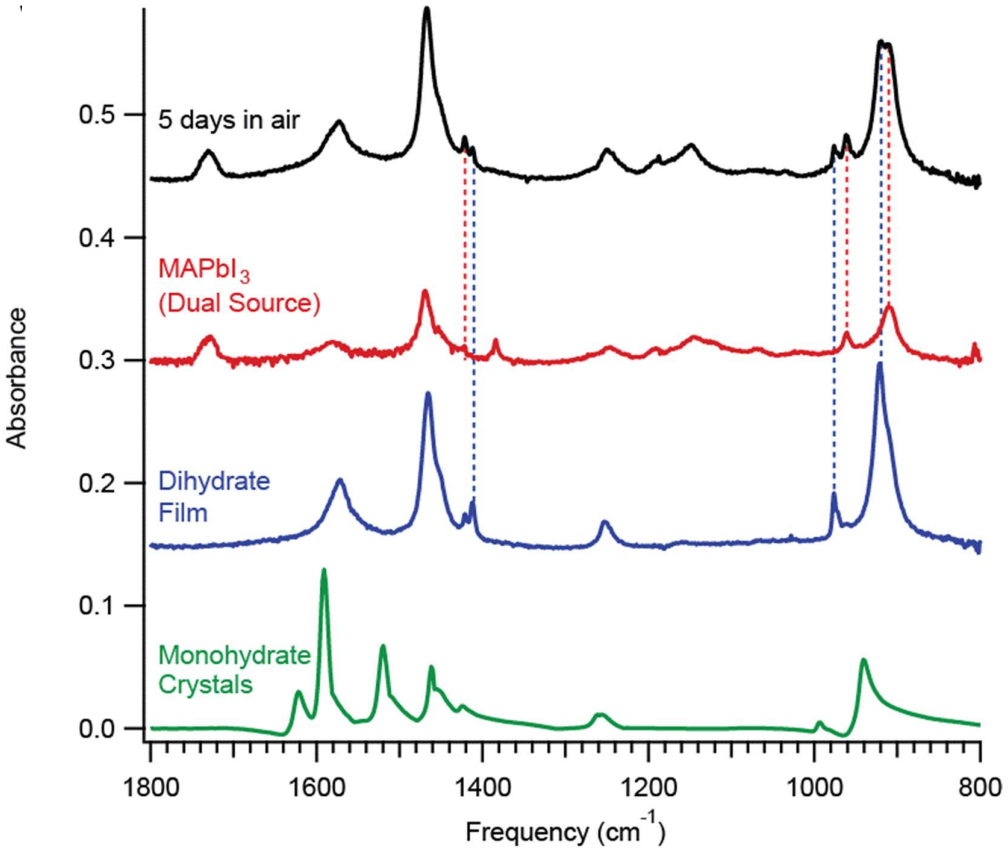


Figure 4.4 IR spectra used to assign vibrational modes associated with the dihydrate $(CH_3NH_3)_4PbI_6 \cdot 2H_2O$

However, perovskite formation proceeds further, and after 11 days, the dihydrate peaks are no longer visible. Once the MAI is consumed, the equilibrium, which is affected by humidity and other environmental factors, shifts to favor the exclusive formation of $MAPbI_3$ without dihydrate inclusions.[130,142,148] Furthermore, the shift in equilibrium leads to dissociation of H_2O into the film, which initiates the degradation of the $MAPbI_3$ (Figure 4.5).

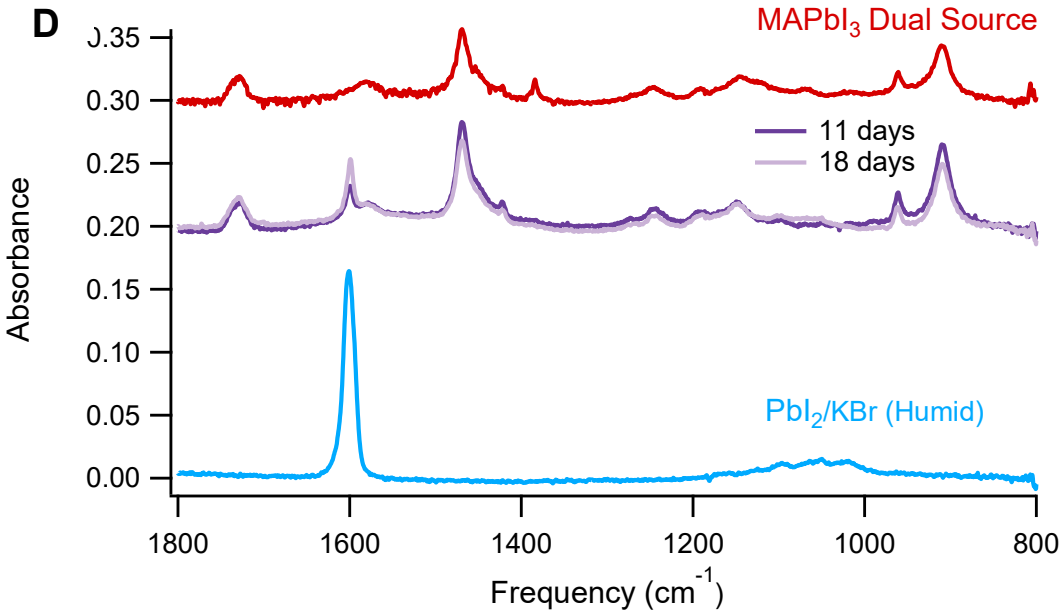


Figure 4.5 IR spectra to show the initiation of degradation

To confirm the occurrence of these chemical and structural changes X-ray diffraction measurements were carried out. Figure 4.6 shows the changes in XRD spectra over a period of 30 hours as the bilayer MAI/PbI_2 film is converted into a $MAPbI_3$ film. It must be noted that because the encapsulated film is slowly being exposed to ambient air throughout the entire experiment, the film formation dynamics are somewhat different in this particular experiment, and therefore only a qualitative comparison with the IR, visible, and PL measurements is possible. XRD measurements show that as expected, a significant quantity of PbI_2 (2θ =12.6°) and MAI (2θ =19.7°) is initially present in the film, reflecting the initial bilayer structure created by thermal evaporation. There is also already a strong (110) reflection corresponding to $MAPbI_3$ (at 2θ=14.1°) due to the crystallisation of $MAPbI_3$ at the interface of the bilayers when the film is heated to room temperature. After 30 minutes, the

PbI_2 reflection (2θ =12.6°) disappears, while the MAI reflections persist, similar to the formation dynamics under vacuum discussed above.

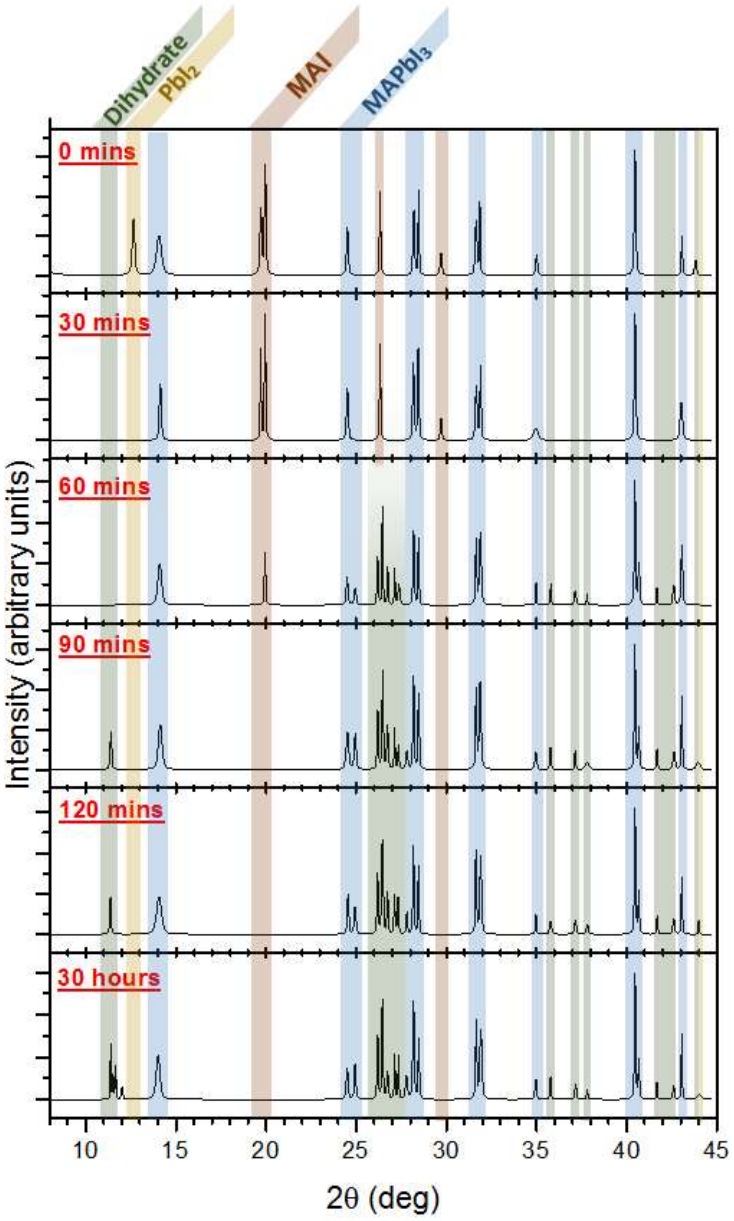


Figure 4.6. X-ray diffraction patterns following the evolution of $MAPbI_3$ from the initial bilayer MAI/PbI_2 films (0 minutes), to the nascent perovskite (30 minutes) and then finally $MAPbI_3$ film (90 minutes). After 90 minutes the dihydrate $(CH_3NH_3)_4PbI_6 \cdot 2H_2O$ is observed to form (2θ=11.4°, 11.5° and 11.6°). The films were sealed with Kapton® polyimide sheets to slow the exposure to ambient air.

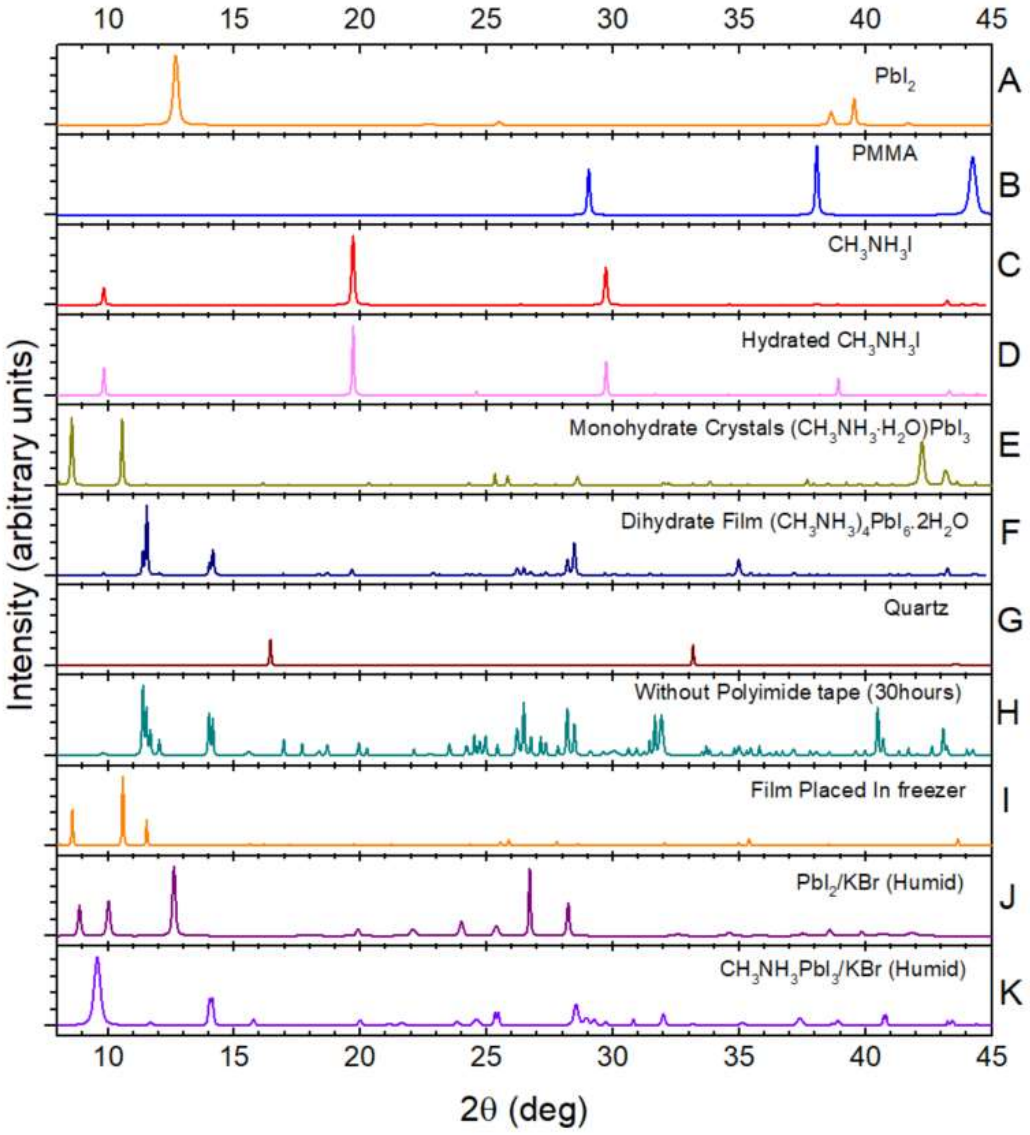


Figure 4.7. X-Ray diffraction patterns for precursors and derivative compounds associated with intermediates or degradation products of $MAPbI_3$.

Diffraction Pattern	Description
A PbI_2	A thermally evaporated 200nm thin film of PbI_2 with a strong reflection for the (001) plane at 2θ=12.6°
B PMMA	A spin coated thin film of Poly(methyl methacrylate)
C MAI	A thermally evaporated 200nm thin film of MAI
D Hydrated MAI	A thermally evaporated 200nm thin film of MAI after exposure to ambient air for 24 hours. Note the formation of peaks at 2θ=24.8° and 39°.
E Monohydrate crystals $(CH_3NH_3 \cdot H_2O)PbI_3$	Monohydrate crystals $(CH_3NH_3 \cdot H_2O)PbI_3$ grown from solution as described above. Characteristic peaks are visible at 2θ= 8.6° and 10.6°. There is also a weak peak at 2θ=11.6° corresponding to a dihydrate reflection indicating that the hydrates are in equilibrium with each other and the $MAPbI_3$
F Dihydrate $(CH_3NH_3)_4PbI_6 \cdot 2H_2O$	A thermally evaporated 350nm thin film of the dihydrate $(CH_3NH_3)_4PbI_6 \cdot 2H_2O$ with its characteristic peaks at 2θ=11.4°,11.5° and 11.6°
G Quartz	Z-cut quartz used as a substrate for all thin films for XRD measurements. The diffraction patterns were referenced against the standard 2θ=16.433°
H Without the polyimide tape	After 30 hours, a diffraction pattern of the characterized film in Figure 2 in the main text is taken without the polyimide tape, to show the clear formation of crystalline dihydrate along with crystalline $MAPbI_3$.
I Film placed in freezer	A thermally evaporated bilayer thin film of MAI/PbI_2 kept at -5°C in ambient air. There is clear formation of both the monohydrate and the dihydrate, and there are no perovskite peaks in the diffraction pattern. Furthermore, there are no PbI_2 or MAI peaks, indicating ion diffusion occurs at relatively low temperatures with the aid of moisture. It is also clear that the hydrates form strongly crystalline domains at relatively low temperatures.
J PbI_2/KBr (humid)	A thermally evaporated 200nm thin film of PbI_2 on a KBr window left in a humid environment. Peaks are formed at 2θ= 8.9° and 10.0° which are somewhat similar to that of the monohydrate
K $CH_3NH_3PbI_3$/KBr (humid)	The converted bilayer films used in the main study were left outside for two weeks in a humid environment. Peaks form at 2θ= 9.6° and 11.7°

Table 2. The descriptions of the various diffraction patterns in Figure 4.7

Unlike the reference spectra of the individual thin films in Figure 4.7, the spectra for the dynamic bilayer film show subtle differences. This can be attributed to the fact that the bilayer film has a mixture of PbI_2, MAI, and $MAPbI_3$. Sixty minutes after the disappearance of PbI_2, the MAI reflections also vanish, and a reflection of the dihydrate (at $2\theta = 11.6°$) appears, which is consistent with the theoretical pattern obtained for the dihydrate.[142] Furthermore, after 30 hours, due to the crystallisation of the dihydrate and the $MAPbI_3$, sharpening of the reflections of $MAPbI_3$ occur, reflecting its theoretical pattern,[149] and lower intensity reflections ($2\theta = 11.4°$ and $11.5°$) of the dihydrate appear.[149] This strongly indicates that the dihydrate and the $MAPbI_3$ form strong crystalline domains within the film. These XRD spectra hence present further evidence of the importance of moisture, and its role in aiding MAI to be more mobile. Monohydrates have previously been observed to form in $MAPbI_3$ in the presence of moisture, [142] the comparison with the diffraction pattern obtained from monohydrate crystals (Figure 4.7) suggest that the monohydrate species is insignificant here, with clear contributions only arising from the dihydrate.

Previous studies have shown that the crystal structure of $MAPbI_3$ is highly amenable to the inclusion of molecules of particular size and polarity, such as NH_3 and CH_3NH_2 which can form crystal structures similar to that of the dihydrate.[150,151] Accordingly, it can be observed that the dihydrate is soluble in 2-propanol (IPA), which allows it to be washed from the film (Figure 4.8) indicating that it is similar in solubility to MAI. The observations help to explain why removal of excess organic component has proven to be beneficial in solar cell efficiencies.[152,153] It is clear that to achieve the highest quality $MAPbI_3$ films,

unreacted MAI needs to be solvated by a solvent of suitable polarity and molecular size which infiltrates the crystal lattice and ensures either that a proper crystal structure forms, or unwanted molecules such as dihydrates are removed. These hydrates could potentially be detrimental as they can eventually decompose to form liquid water and PbI_2 which causes $MAPbI_3$ film degradation.[142,148]

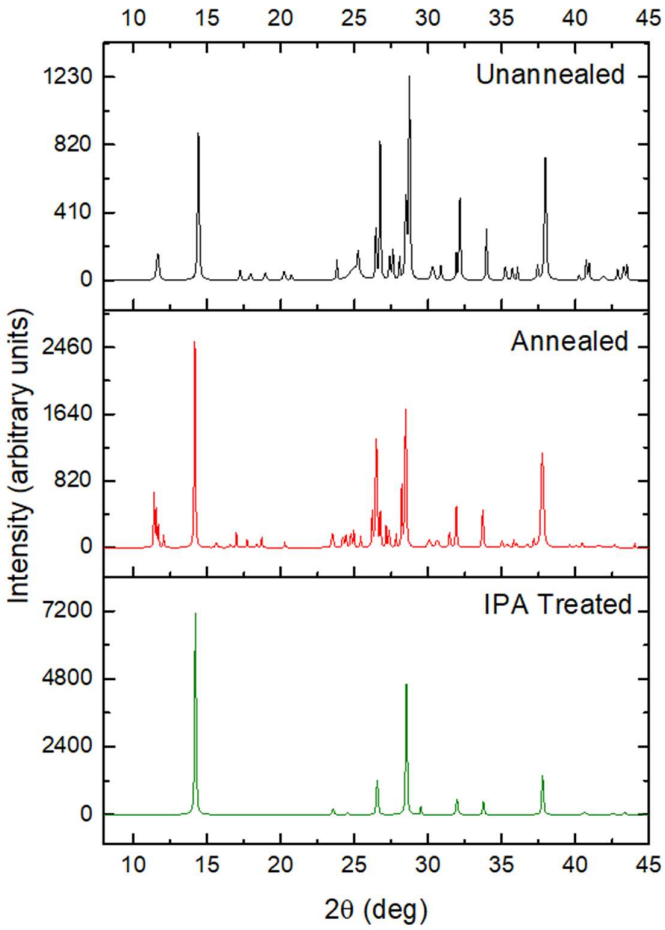


Figure 4.8 XRD patterns for a $MAPbI_3$ film fabricated via dual source evaporation on Fluorine doped Tin Oxide (FTO). A dihydrate $(CH_3NH_3)_4PbI_6 \cdot 2H_2O$ is formed after the bilayer film is exposed to ambient air immediately after the fabrication on the film. After annealing in ambient air, the dihydrate peaks remain. Spin coating IPA on the films clearly shows the removal of the dihydrate and a more crystalline film.

With the complex chemical changes identified, it is important to analyse how these changes affect the optoelectronic properties of the film. Here, the photoluminescence lifetimes τ_{av} and band edge absorption features during film formation (Figure 4.9), which are sensitive probes of charge-carrier trap density and film crystallinity, are examined. The first few hours of PbI_2/MAI bilayer interdiffusion in vacuum are marked by high trap densities and fluctuations: τ_{av} varies erratically (Figure 4.9A) and the absorption onset is considerably broadened (Figure 4.9C). These fluctuations are unsurprising considering that the greatest amount of ion movement occurs during this time period, which creates considerable disorder in the crystalline domains.[154] As a result, this intermediate phase of perovskite formation is associated with a high density of sub-gap trap states, as indicated by short photoluminescence lifetimes (Figure 4.9A) and considerable absorbance at 800nm, just below the band gap onset (Figure 4.9B). Over the ensuing 7 hours in vacuum, this sub-gap absorbance then decreases, coinciding with the stabilisation of the PL lifetimes, in accordance with a decrease in trap density as the film forms. Over the initial 10 hours in vacuum, the band edge of the as-formed $MAPbI_3$ continuously red shifts and sharpens (Figure 4.9C,D) indicating that mass diffusion of MAI is followed by the formation of nucleation sites and then the crystallisation of $MAPbI_3$, in analogy with crystallisation dynamics reported from real-time XRD.[155] Following this initial period of rapid film transformation, the progression of changes begins to slow. PL lifetimes continue to increase, and the band edge continues to red shift and sharpen as the overall crystallinity of the film improves and larger crystalline domains form.

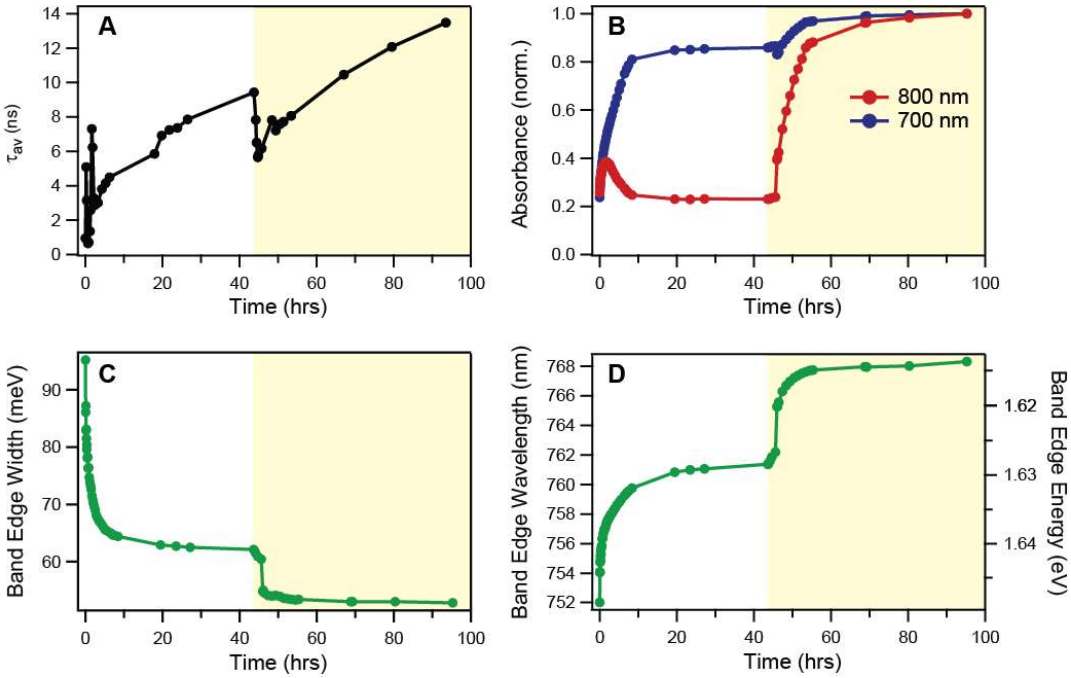


Figure 4.9 (A) Time resolved PL lifetime as a function of time from the initial deposition of the MAI/PbI_2 bilayer to the formation of $MAPbI_3$, both in vacuum (white) and after exposure to ambient air (yellow shading). **(B)** Changes in absorbance at wavelengths of 700 nm and 800 nm derived from the initial absorption spectra (Figure 4.1A & 4.1B). **(C)** Width of the band edge absorption onset determined from the full-width half-maximum of a Gaussian fit to the derivative spectrum. **(D)** Band edge wavelength and energy obtained from Gaussian fits to the differential absorption spectra. Values correspond approximately to the midpoint of the band gap absorption feature. *Photoluminescence lifetime measurements were carried out by Adam D. Wright.*

The subsequent exposure to air triggers further changes in optoelectronic properties. Figure 4.9A shows that the PL lifetimes initially decrease sharply suggesting that exposure to moisture initially leads to the formation of further trap states. This effect is attributed to the organic species becoming more mobile through exposure to moisture which again temporarily disrupts the crystal structure. The matching IR and XRD measurements discussed above suggest

that exposure to ambient air leads to an increase in MAI diffusion and a faster crystallisation process.[156] After about 5 hours, however, these rapid transformations settle, and the PL lifetime increases substantially in accordance with improved material quality. Concomitantly, the width of the band edge sharpens (Figure 4.9C) and the band edge shifts to the red (Figure 4.9D). These changes hence result from moisture-driven enhancement of material crystallinity that leads to larger domain sizes, [157] in analogy to previous studies correlating grain- and crystal-size with changes in absorption onset in $MAPbI_3$.[155] While the nominal absorbance below the bandgap (800nm, Figure 4.9B) appears to increase during this crystallisation phase, this is most likely caused by enhanced light scattering effects, which become stronger as smaller (sub wavelength) crystalline domains combine to form larger domains.

4.3 Summary

In summary, through careful control of substrate temperature during growth, the real time the chemical transformations evolving as MAI diffuses into PbI_2 to form a $MAPbI_3$ perovskite film have been monitored. The changes occurring in either vacuum or ambient air shed light on key parameters that need to be controlled to create a high-quality perovskite film. Clear evidence is presented from visible and IR transmission spectra that in vacuum MAI and PbI_2 interdiffuse to form a nascent $MAPbI_3$ perovskite structure. However ambient air is required to fully crystallise $MAPbI_3$ and remove excess MAI. The hygroscopic nature of MAI allows it to absorb moisture, making it more mobile and allowing for better intermixing of PbI_2 and MAI. It is, however, found to be essential that no excess MAI remains within the film, as the unreacted MAI

absorbs moisture to form the dihydrate $(CH_3NH_3)_4PbI_6 \cdot 2H_2O$, which is a relatively stable crystalline material. Furthermore, after a certain period, chemical and optoelectronic changes with exposure to moisture cease, and therefore any further moisture absorption is likely to be detrimental. These dynamic material changes are further correlated with the corresponding evolution of charge-carrier lifetimes and absorption features, identifying dynamic periods of high ion motion and high trap densities and observing the effect of moisture in driving crystallisation. These findings provide fundamental insight into the dynamics of perovskite formation. Importantly, they also highlight the role that moisture has to play in ensuring the complete reaction of the precursor materials, thus leading to the formation of strong crystalline $MAPbI_3$, which is crucial for optimal solar cell performance.

Chapter 5

Interface Morphology in Perovskite Photovoltaic Devices

In the study presented in this chapter, a single batch of vapour-deposited $CH_3NH_3PbI_3$ ($MAPbI_3$) on a range of device architectures is used to show that the cause of hysteresis in planar heterojunction $MAPbI_3$ solar cells originates from the interface between the perovskite and the electron transport layer, and that interface engineering can be used to eliminate hysteresis in these devices. Furthermore, using transmission electron microscopy (TEM) and scanning transmission electron microscopy (STEM) show that under identical growth conditions the interface affects perovskite morphology and crystallinity.

5.1 Introduction

Planar heterojunction solar cells based on both vapour-deposited and solution processed $MAPbI_3$ have been reported to exhibit significant hysteresis in their J-V characteristics.[158–160]

Vapour-deposited perovskite solar cells are used in the study presented in this chapter to investigate the origin of hysteresis, as vapour deposition allows the simultaneous deposition of perovskite films on multiple devices with different planar architectures under identical conditions. Vapour deposition involves heating precursor solids in high vacuum, allowing the sublimed material to uniformly condense on a substrate.[161] While vapour deposition is currently less commonly used compared with solution processing, it considerably reduces the amount of independent variables, leading to highly uniform and pin-hole free thin films on a consistent basis.[91] As a technique widely used in industry for organic light emitting diodes and inorganic semiconductors, thermal vapour deposition has also shown to have a high rate of batch to batch reproducibility.[13] There are two main methods to create a $MAPbI_3$ thin film by thermal vapour deposition: co-evaporation, by which the precursor materials methyl ammonium iodide (MAI) and lead iodide (PbI_2) are evaporated simultaneously[162] and a two-step evaporation, whereby the precursors are deposited sequentially.[89] This study focuses on films produced by dual source thermal co-evaporation.

5.2 Results and Discussion

To establish a link between device J-V hysteresis and architecture statistics from 186 planar heterojunction solar cells produced from 17 deposition batches are presented, where deposition parameters and annealing conditions were optimised for the particular architecture. In order to understand the underlying cause of hysteresis the investigation will then concentrate on a subset of architectures where the perovskite was deposited in the same vapour deposition run, without any post-growth thermal annealing.

A clear link between J-V hysteresis and device architecture can be seen by examining **Figure 5.1** which summarises the performance of 500 devices with four common device architectures labelled A-D. For types A-C the $MAPbI_3$ perovskite layer was evaporated onto an electron transport layer (ETL), a geometry that is common for most published perovskite solar cells and which will be referred to as a "regular" device architecture.[163] The ETLs for types A, B and C were TiO_2, C_{60}, [6,6]-phenyl C_{61} butyric acid methyl ester (PCBM) respectively, while the hole transport layer (HTL) was 2,2',7,7'-Tetrakis-(N,N-di-4-methoxyphenylamino)-9,9'-spirobifluorene (Spiro-OMeTAD). In contrast, for the type D, which will be referred to as an "inverted" device architecture, the PCBM ETL was deposited after the $MAPbI_3$ was evaporated on a poly(4-butylphenyl-diphenyl-amine) (PolyTPD) HTL.[164]

Figure 5.1a shows the J-V characteristics of the champion devices for each architecture type A-D. For the type A (c-TiO_2 ETL) a clear hysteresis can be seen between the forward and reverse J-V sweep. While the standard method to determine the PCE of a solar cell is based on analysis of the J-V curve,[165] it

has been proposed that an alternate method measuring the "stabilised power output" (SPO) may be more appropriate in assessing the working efficiency of hysteretic cells.[158] In this method PCE is measured as a function of time, by holding the device at a load corresponding to the maximum power point.

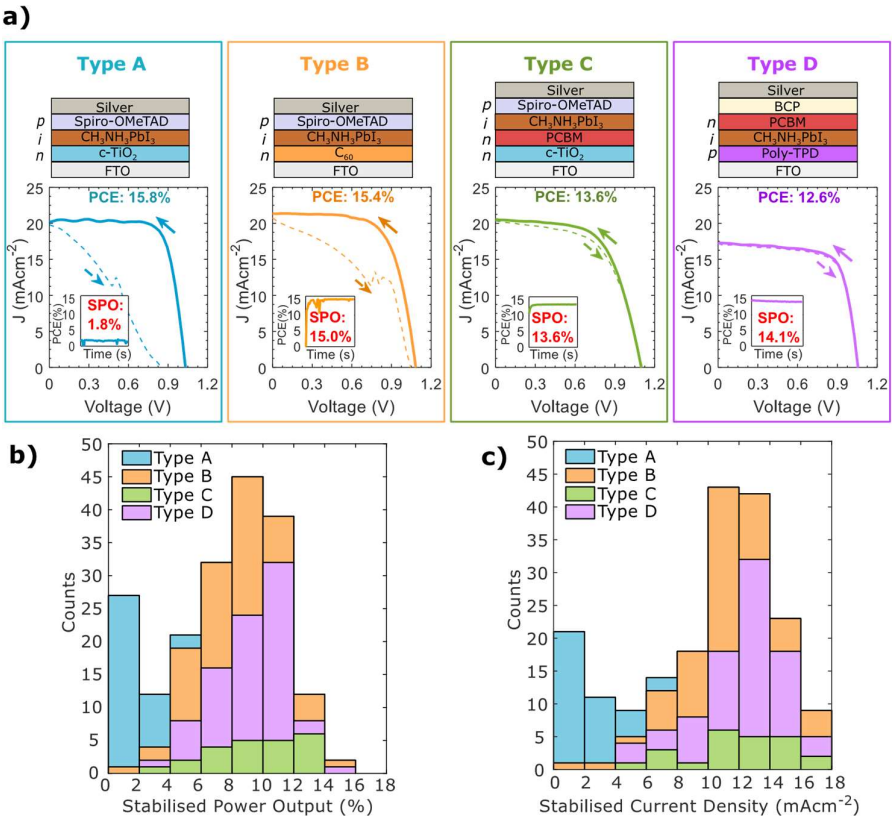


Figure 5.1. a) Schematics for different planar heterojunction device architectures with varying n-type layers (type A-C) and an inverted device architecture (type D), with the corresponding current-voltage (J-V) curves for the champion devices. The arrows denote the scan direction of the J-V sweep. The inset in each J-V curve shows the stabilised power output (SPO) after 50 seconds under a constant bias. Histograms showing the statistical variation for the different device types b) Stabilised power output (SPO) c) Stabilised current density (Jmpp). Type A devices (blue) have very poor stabilised currents and efficiencies compared to devices which use n-type layers used in the device types B (orange), C (green) and D (purple). Type B devices shows hysteresis, yet the stabilised device parameters are significantly higher compared to type A devices.

Maintaining the device at constant bias more closely simulates the operation of a solar cell under load, thus measurements of SPO and stabilised current density at maximum power point (J_{mpp}) can be more representative indicators of the true device efficiency.

The type A device utilises the wide band gap semiconductor compact TiO_2 (c-TiO_2). It has been implemented in metal-halide perovskite devices as an ETL, largely due to its historic use in dye-sensitised solar cells.[166] The type A device represented in Figure 5.1a shows a PCE (measured by reverse J-V sweep) of 15.8%, which is an order of magnitude higher than the SPO (1.8%). In fact, all c-TiO_2 devices tested under a constant bias showed significantly lower SPO (<6%) and J_{mpp} (<8 $mAcm^{-2}$) as shown by the statistics in **Figure 5.1b** and **5.1c** (blue columns)**.**

All other architectures, B-C, show a good agreement between the PCE and SPO. Interestingly for the type B device, in which the c-TiO_2 ETL was entirely replaced by $C_{60,}$ there is significant J-V hysteresis yet a good agreement between PCE (15.4%) and SPO (15.0%). Type C devices, which incorporate a layer of PCBM on top of c-TiO_2 as ETL, show minimal hysteresis. Finally, the inverted device (type D) shows no observable hysteresis with again the SPO being representative of the PCE. This is in good agreement with previous results, where inverted devices employing evaporated $MAPbI_3$ thin films show no hysteresis.[167]

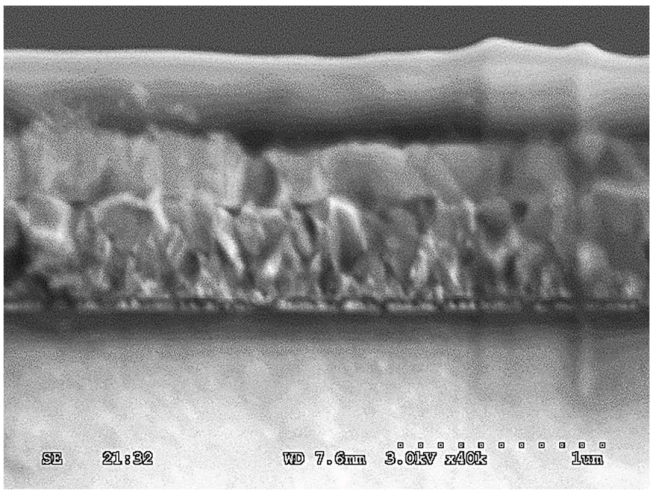


Figure 5.2 Scanning electron microscopy images of the type B device, showing that the perovskite makes direct contact with the FTO

The improved SPO after changing the ETL from c-TiO_2 (type A) to C_{60} (type B) is consistent with C_{60} being a more effective electron extraction material.[105] Furthermore the hysteresis observed in the type B devices, can be attributed to formation of pin holes in the spin coated C_{60} thin films, due to its low solubility in solvents.[168] In the pinhole regions of type B devices the $MAPbI_3$ makes direct contact with FTO (as shown in **Figure 5.2**). It has been shown previously that devices with FTO/$MAPbI_3$ interfaces exhibits severe hysteresis and poor SPO.[159] The good SPO and J_{mpp} for type B devices can thus be attributed to steady-state photocurrent being shunted around these pin-hole regions. However, to achieve devices with both high SPO and low J-V hysteresis it is important to ensure that $MAPbI_3$ does not make direct contact with the FTO.

The statistics of SPO and J_{mpp} for all devices of the four architectures are shown in **Figure 5.1b** and **5.1c** respectively. The spread in stabilised efficiencies can be attributed to both batch-to-batch variations, as a result of the deposition optimisation process, and also to variations in the quality of the spin coated

ETLs and HTLs. Further details of the comparison between the SPO of regular and inverted devices are provided in **Figure 5.3**, and evidence that the HTL, Spiro-OMeTAD, does not contribute to the drop in the SPO is also presented in Figure 5.3**.** Thus, by assessing such a large number of devices, this can be confidently attribute to the discrepancy that arise between the PCE and SPO in $MAPbI_3$ planar heterojunction solar cells to the choice of the ETL.

Having established that device SPO is affected by the ETL and its charge extraction efficiency the study now focuses on the origins of the hysteresis effect. A set of devices with different ETLs in which the $MAPbI_3$ layer was deposited in the same deposition run. This enables studying the interface and its effect on the perovskite independent of the perovskite composition or batch variations.

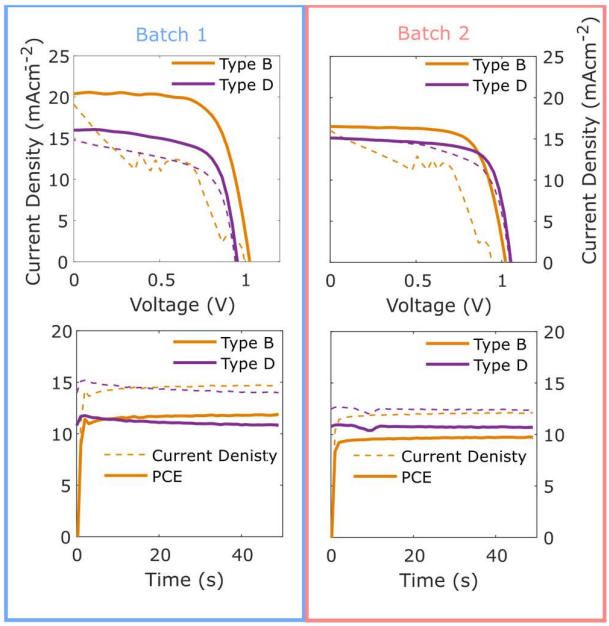


Figure 5.3. Current voltage characteristics to show the hysteresis on Type B and D devices grown in the in the same batch. The dashed lines represent the forward sweep from J_{sc} to V_{oc} .The stabilised PCE and current density of the two types of devices.

Figure 5.4 presents a single batch of devices with identical perovskite layers and the differing ETLs, enabling the direct to comparison the effect of different charge extraction layers. The specific ETL for each device was, c-TiO_2 for type A; both c-TiO_2 and a 50nm layer of PCBM for type C_{50nm}; both c-TiO_2 and a 100nm layer of PCBM for type C_{100}; and only a 50nm layer of PCBM for type E. **Figure 5.4a** shows a cross sectional scanning electron micrograph (SEM) of a type A device, where only c-TiO_2 is employed as an ETL. It reveals that the interface between c-TiO_2 and $MAPbI_3$ includes dark regions as detected by the secondary electron detector in the SEM. The inhomogeneous ETL along the interface leads to poor charge collection efficiency, extensive charge recombination, and is likely to result in device hysteresis via an electrical capacitive effect across the amorphous region.[169,170] In contrast, with the introduction of a 50nm layer of PCBM in between the c-TiO_2 and $MAPbI_3$ (type C_{50nm}), as has been previously employed in solution processed perovskite solar cells,[171,172] there is a considerably improved interface between the $MAPbI_3$ and PCBM as shown in **Figure 5.4b**. However, the coverage of PCBM over the rough c-TiO_2 surface is not complete, hence regions of direct contact between the c-TiO_2 and $MAPbI_3$ exist. Consequently, the J-V characteristics show some hysteresis even though the SPO is representative of the PCE. As shown before in Figure 5.4a, c-TiO_2/$MAPbI_3$ is not an ideal ETL for the $MAPbI_3$.

Doubling the thickness of the PCBM layer to 100nm creates a pinhole-free layer which eliminates any regions of amorphous $MAPbI_3$ resulting from direct contact between $MAPbI_3$ and TiO_2. Hence an excellent interface is created for efficient electron extraction, and thus negligible hysteresis is observed (**Figure 5.4c**). Since the PCBM is deposited before the $MAPbI_3$, and there was no post

growth annealing of these devices, it is unlikely that PCBM infiltrates between the grains. This indicates that the reduction in hysteresis, caused by PCBM, is a result of modifying the interface, rather than passivation of grain boundaries throughout the bulk.

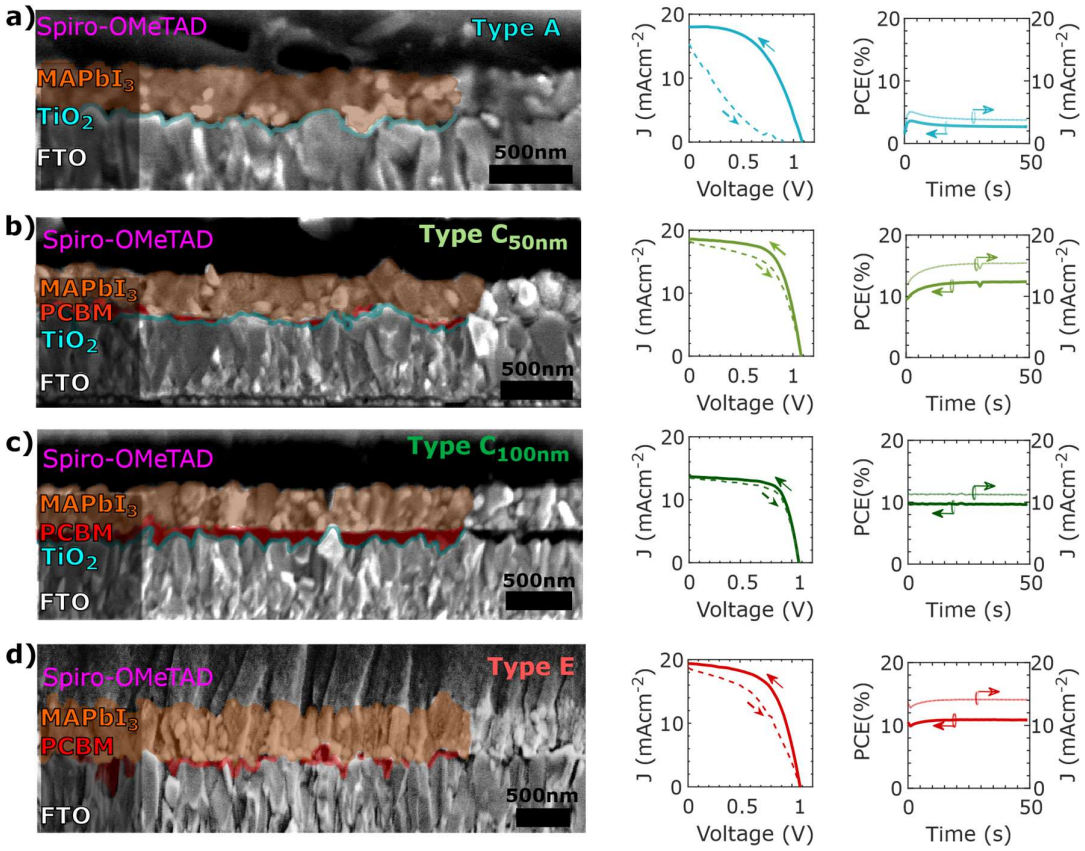


Figure 5.4. SEM images, J-V curves and stabilised power output over 50 seconds of operation for; **a)** Type A **b)** Type C_{50nm} **c)** Type C_{100nm} **d)** Type E. Devices were made with thermally evaporated $MAPbI_3$ in the same deposition, ensuring that the composition, thickness and conditions are the same for each device. There was no post deposition post annealing of the thin films. This allows the systematic attribution to the causes of the difference between the J-V characteristics of each device architectures. Type C_{50nm} and E have a thin 50nm layer of PCBM, whereas type C_{100nm} has a thick 100nm PCBM layer.

Therefore, to suppress hysteresis the ETL/$MAPbI_3$ interface incorporates an efficient electron extraction material that is free of pinholes. The features are exemplified in the type C_{100nm} devices, whilst the 100nm PCBM film is uniform and pinhole free it is too thick to enable efficient device operation. This is evident by its considerably lower J_{sc} (**Figure 5.4d**). Other studies have shown that the optimum PCBM thickness is around 10nm.[167] The reason why PCBM needs to be so thin is not clear, since its electron mobility is at least as high as the hole-mobility in Spiro-OMeTAD. It is likely however that it requires n-type doping in order to operate efficiently at thicknesses >10nm.

	PCE [%]	J_{sc} [mAcm^{-2}]	V_{oc} [V]	FF	SPO [%]	SJ [mAcm^{-2}]
Type A	10.0 *(8.4)*	18.0 *(16.8)*	1.07 *(1.06)*	0.52 *(0.47)*	2.7 *(2.4)*	3.7 *(3.5)*
Type C_{50nm}	12.8 *(11.6)*	18.6 *(17.9)*	1.07 *(1.07)*	0.65 *(0.61)*	12.4 *(11.8)*	15.4 *(14.6)*
Type C_{100nm}	10.2 *(8.5)*	13.7 *(13.1)*	1.07 *(1.04)*	0.68 *(0.62)*	9.7 *(9.2)*	11.2 *(11.1)*
Type E	12.4 *(11.6)*	19.4 *(18.3)*	1.07 *(1.07)*	0.60 *(0.59)*	10.9 *(11.0)*	14.6 *(13.4)*

Table 5.1 Showing the devices performance of the devices shown in Figure 5.4 Where the numbers in the brackets represent a mean average of at least 6 devices from the batch in study.

Markedly, whilst the reverse sweep J-V characteristics may not always represent the performance of the device under load, it always shows the potential of the device PCE and more specifically the $MAPbI_3$ thin film. Simply inserting a PCBM layer in the type A device to create a type C_{50nm} device is a clear example of this. The type A devices show a reverse scan PCE of 10% and SPO of 2.7% (**Table 5.1**). On the other hand, type C_{50nm} shows an improved SPO of 12.4%, which closely represents the reverse sweep of the type A device. This is essential for troubleshooting the cause of low SPO and hysteresis observed in many perovskite devices. Modification of the interface rather than the

perovskite itself should achieve a hysteresis free device with a SPO representative of the PCE.

To characterise the thickness and the conformity both the TiO_2 and the PCBM, TEM, high angle annular dark field (HAADF) imaging in STEM mode and energy dispersive X-ray spectroscopy (EDX) were carried out on the type A and type C_{100nm} devices. HAADF imaging is especially sensitive to atomic number (Z) contrast because heavier elements will scatter electrons at the high angles subtended by the HAADF detector. Consequently, bright regions will result from higher Z elements and in addition to denser regions while dark regions correspond to light elements and low-density regions.

Whilst TEM, has proven useful to characterise the inorganic and organic semiconductors, the technique has proven to be difficult to characterise metal-halide perovskite devices. This is predominantly the case for inorganic-organic metal-halide perovskites, as a high electron beam dosage, or prolonged exposure to the primary electron beam will cause the perovskite to convert into PbI_2.[173] Therefore it is important to ensure that the electron dosage is recorded and is low enough to obtain TEM images that represent the perovskite and not PbI_2. However, the transport layers are far more resilient than the hybrid metal-halide perovskites and thus can be examined using TEM.

Figures 5.5a and **5.5d** show HAADF images of the type A and C_{100nm} devices respectively. The main difference between the two is a dark contrast region between the $MAPbI_3$ and the FTO/c-TiO_2 layers in the C_{100nm}. EDX maps of the corresponding HAADF regions are shown in **Figures 5.5b** and **5.5e** with a composite false colour image of the elements Pb (green), C (red) and Sn (blue).

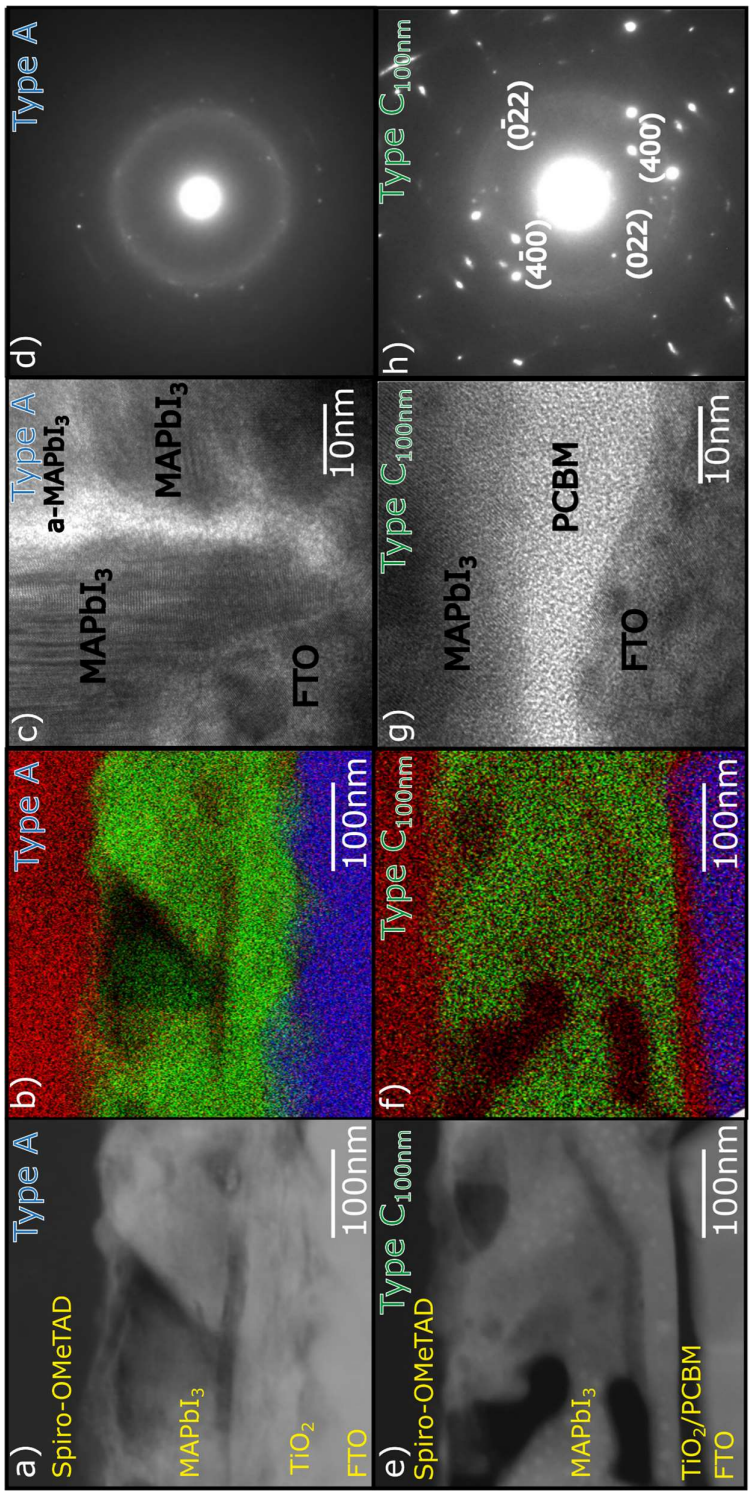


Figure 5.5. a) HAADF Image of a type A device. **b)** A composite EDX map of the type A interface with carbon (red), lead (green) and tin (blue) **c)** HRTEM image of the interface in type A devices **d)** electron diffraction pattern of the perovskite **e)** HAADF Image of a type C_{100nm} device **f)** A composite EDX map of the type C_{100nm} interface with carbon (red), lead (green) and tin (blue) **g)** HRTEM of the interface in a type C_{100nm} device **h)** electron diffraction pattern from the perovskite region. *TEM, EDX and electron diffraction was carried out by Jenny Wong-leung*

The HRTEM image (Figure 5.5d) of the interface clearly shows the perovskite layer and the FTO/c-TiO_2 layer interlaced with amorphous regions of the PCBM, to back up the SEM images in Figure 5.4.

The presence of Ti from the thin layer of c-TiO_2 is shown in Figure 5.6. In the case of the type C_{100nm} (Figure 5.5e), the darker contrast observed in the HAADF image at the interface between the FTO and $MAPbI_3$ layers corresponds to a C rich layer, observed in the EDX map, which represents the continuous conformal PCBM layer (**Figure 5.5f**).

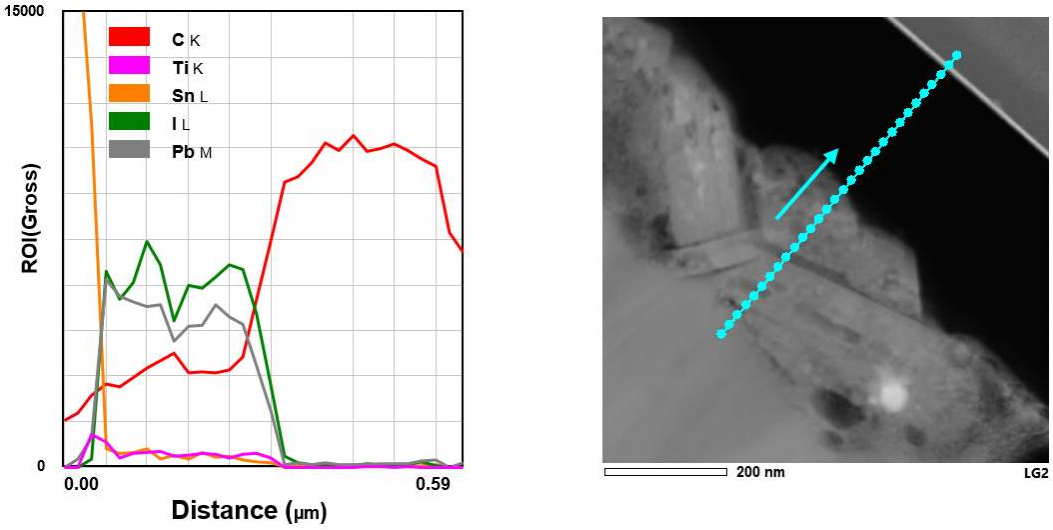


Figure 5.6 a) Plot showing the integrated counts for the ROI of different elements in a line scan performed on the sample. **b)** corresponding HAADF image showing the linescan and its direction. *The TEM and EDX, was carried out by Jenny Wong-leung*

It is also clear that with the presence of a conformal PCBM layer with good electrical contact to a high-quality perovskite layer, there is little to no hysteresis with a high SPO, as shown by the type C_{100nm} devices. While hysteresis observed in perovskites based devices has previously shown to be a

combination of ion migration and the presence of interfacial trap states,[95,109,159,174,175] it is clear from this particular study that interface morphology of the perovskite plays a significant role in J-V hysteresis.

5.3 Summary

In conclusion, an important advantage of the vapour deposition technique has been utilised, whereupon a single batch of perovskite thin films have the same stoichiometry and thickness, to probe which interface is the cause of the hysteresis and deficient SPOs. The results show that the quality of the interface between ETL/$MAPbI_3$, and the choice of ETL, is critical in suppressing hysteresis and reduced SPOs. It is hypothesised that the poor electrical properties of the corresponding interface are a significant contributing factor affecting the device hysteresis. Therefore, the key to eliminating hysteresis from $MAPbI_3$ planar heterojunction solar cells is to develop a well-engineered interface between the perovskite layer and the (n-type) electron transport layer (ETL). Ideally, the ETL should be an efficient electron extraction material with no pinholes, while the $MAPbI_3$ at the interface should be both homogenous and crystalline, such hysteresis-free devices have stabilised power outputs matching the power conversion efficiencies from single sweep J-V measurements and are promising for large-area renewable energy generation.

Chapter 6

Photocurrent Spectroscopy of Perovskite Photovoltaic Devices

In this chapter the device characteristics of the prototypical perovskite solar cells based on methylammonium lead triiodide ($CH_3NH_3PbI_3$) over a broad temperature range from 15 K to 350 K (-252°C to 77°C) are assessed. For these devices, there is a peak in the short-circuit current density and open-circuit voltage at 200 K (-73°C) with decent operation maintained up to 350 K. A clear signature of crystalline PbI_2 contributing directly to the low-temperature photocurrent spectra is identified, showing that PbI_2 plays an active role (beyond passivation) in $CH_3NH_3PbI_3$ solar cells. Finally, it is observed that a blue-shift in the photocurrent spectrum occurs with respect to the absorption spectrum at low temperature (15 K), allowing the extraction of a lower limit on the exciton binding energy of 9.1 meV for $CH_3NH_3PbI_3$.

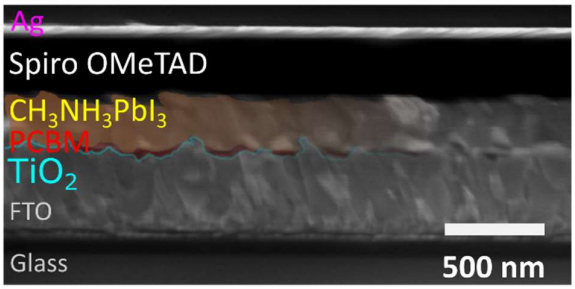
6.1 Introduction

High-performance solar cells are sought after for power generation in extreme environments such as space. However, to be suitable for use e.g. on satellites, solar cells must be able to operate over a wide temperature range typically from -100°C to 125°C (173 K – 398 K).[104] An in-depth understanding of perovskite solar cell operation over a wide range of temperatures is therefore crucial for the evaluation of their use in such locations.

The sensitive technique of Fourier transform photocurrent spectroscopy (FTPS) combined with current-voltage (J-V) measurements and absorption spectroscopy has been utilised to assess the viability of $MAPbI_3$ solar cells over a temperature range from 15 K to 350 K. The device characteristics, short-circuit current density and open-circuit voltage, was optimal at 200 K, and devices operated well up to 350 K. However, a dramatic drop in photocurrent was observed for temperatures lower than 200 K, with photo-currents and -voltages dropping rapidly towards very low temperatures (15 K). Interestingly, at low temperatures it is observed that a characteristic contribution of PbI_2 in the $MAPbI_3$ device photocurrent spectra, which is identified by comparison with a PbI_2-only device with the same architecture. Moreover, there is a discrepancy between the spectral onset of absorption and photocurrent (i) at low temperature, owing to the formation of excitons (ii) around the orthorhombic-tetragonal phase transition, as a result of mixed phases and (iii) at high temperature, because of enhanced collection of charge-carriers generated by longer wavelength light.

6.2 Results and Discussion

Figure 6.1 shows a cross-sectional scanning electron microscopy image of the device structure used for this study. The device was fabricated on a fluorinated-tin-oxide (FTO) coated glass substrate. It consisted of a dual TiO_2-PCBM electron extraction layer upon which the perovskite $MAPbI_3$ was deposited via co-evaporation of MAI and PbI_2. A hole extraction layer of Spiro OMeTAD was spin-coated over the perovskite prior to thermal evaporation of a silver contact. Previously it was shown that this architecture produces high quality perovskite thin films and devices with minimal current-voltage hysteresis and high stabilised power output.[90] The devices were slowly cooled down to 4 K and then characterised as the temperature was increased incrementally. For all measurements, a tungsten halogen lamp was used as the light source.



PCE (%)	J_{sc} (mAcm^{-2})	V_{oc} (V)	FF
10.92	17.86	1.07	0.57

Figure 6.1. SEM image showing the device structure used in this study, with the current-voltage characteristics measured under 1 sun illumination (AM 1.5G, 100 mW cm^{-2}).

To assess the device characteristics as a function of temperature, in-situ short-circuit current density (J_{sc}) and open-circuit voltage (V_{oc}) of the $MAPbI_3$ device

were measured between 15 K and 350 K, with the results shown in Figure 6.2a and 6.2b respectively. The temperature dependence of the V_{oc} incorporates two different regimes, one above and one below 200 K, as observed previously when $MAPbI_3$ based devices had been cooled to 80 K.[176–180] The V_{oc} increases with temperature from 15 K and peaks at a value of 1.13 V at 200 K. The $J_{sc,}$ shows an even steeper increase in over 5 orders of magnitude with temperature, also peaking at 200 K. For temperatures higher than 200 K, the V_{oc}, decreases again, similar to observations made for in silicon and organic solar cells,[27,28,181,182] for which the effect has been attributed to the quasi-Fermi levels of the Boltzmann–like electron and hole populations moving closer together as the temperature is increased.[27,29,183]

In order to evaluate the effect of temperature-mediated changes in the structural disorder of the $MAPbI_3$ perovskite layer, the Urbach energy (E_u) was extracted from the photocurrent spectra.[31,43,184] Figure 6.2c shows the dependence of E_u (and hence disorder) as a function of temperature. To allow correlation with structural changes, it is indicated with the shaded bars the temperature regions where $MAPbI_3$ is known to undertake structural phase transitions, i.e. from orthorhombic to tetragonal at 140-160 K and from tetragonal to cubic near 310-330 K.[103,185,186] In the temperature region for which $MAPbI_3$ exists in the tetragonal crystal structure, E_u exhibits a minimum value of 12.1 meV at 135 K, which rises to a maximum value of E_u =19.1 meV at 200 K and then decreases again to E_u = 16.7 meV at room temperature (290 K). In the cubic phase, the Urbach energy was found to be near 16 meV and insensitive

to temperature. It was not possible to obtain E_u in the orthorhombic phase owing to the co-existence of small tetragonal domains.[186]

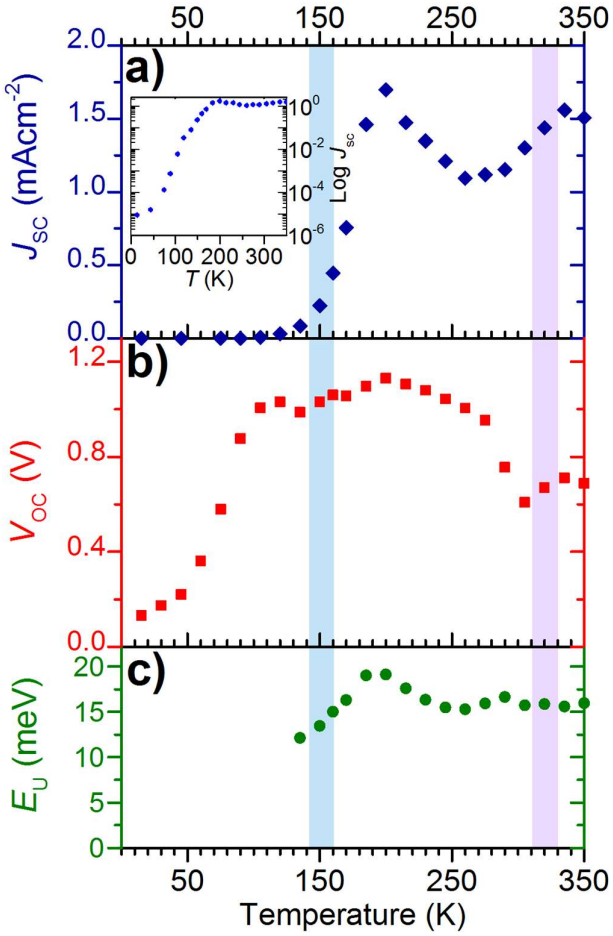


Figure 6.2. a) The temperature dependence of the short-circuit current density for the $MAPbI_3$ device, with the inset showing the J_{sc} in a semi-logarithmic scale. **b)** The temperature dependence of the open-circuit voltage for the same device **c)** The temperature dependence of the Urbach energy (E_u) for the device derived from fits to external quantum efficiency spectra (as described in the SI). In-situ temperature-dependent measurements were carried out using a tungsten halogen lamp with a light intensity of 0.29 sun. The shaded blue area shows the low-temperature phase transition from an orthorhombic to a tetragonal crystal structure.[103,186] The shaded lilac area shows the high-temperature phase transition from the tetragonal to the cubic perovskite crystal structure.[103,185]

While thermal energy can play a direct role in dynamic structural disorder,[42,187] the non-monotonic trend in E_u indicates that this is unlikely to be the major cause of the energetic broadening of the photocurrent onset here. Rather it seems that additional changes with temperature, as for example strain, contribute to disorder. It is also interesting to note that the temperature dependence of the device J_{sc} and V_{oc} is not well correlated with the temperature dependence of the Urbach energy, indicating that disorder in the perovskite layer is unlikely to be the main factor limiting the low-temperature J_{sc} and V_{oc} of $MAPbI_3$ solar cells. The pronounced temperature variation in the J_{sc} and V_{oc} may in part be attributed to factors unrelated to the $MAPbI_3$ layer, such as the charge-extraction performance of the electron- and hole-extractor layers. Hybrid perovskites such as $MAPbI_3$ have been found to exhibit enhanced charge-carrier mobilities with lower temperature,[103] as a result of reduced electron-phonon coupling,[188] compatible with band transport within a large-polaron picture.[65] However, charge-transport in organic semiconductors and amorphous solids, such as the TiO_2, PCBM and Spiro OMeTAD materials typically used for charge-extraction for perovskite devices, is typically governed by hopping transport that may be thermally activated.[189,190] Jacobsson *et al.* observed a significant increase in series resistance from current-voltage scans, as the temperature decreased, confirming that the reduction in the conductivity of the organic charge transport layers leads to a decrease in J_{sc}.[178] Therefore, the sharp drop in J_{sc}, as the temperature is lowered past 150 K (Fig. 6.2a) may potentially be partly remediated by use of alternative charge-extraction materials that exhibit band-transport at low temperatures, similar to $MAPbI_3$. Temperature-dependent measurements of photocurrent spectra is used to elucidate the role

of excess of PbI_2 in the performance of $MAPbI_3$ solar cells. A slight excess of PbI_2 in such devices has been shown previously to enhance the PCE.[191,192] It has been postulated that PbI_2 provides a crystalline framework which increases the crystal quality of $MAPbI_3$.[193] Furthermore, the presence of PbI_2 at grain boundaries has been found to be beneficial for device PCE.[194] However, the contribution of PbI_2 in to overall opto-electronic properties of the solar cell is still unclear. Room temperature measurements aimed to detect the photocurrent generated by PbI_2 have proven to be difficult as the high absorption coefficient of $MAPbI_3$ at the 2.35 eV photon energy[89] (λ=528 nm) masks any contribution from PbI_2.[195] The presence of remnant crystalline PbI_2 in our $MAPbI_3$ layers is also supported by X-ray diffraction pattern in Figure 6.3.

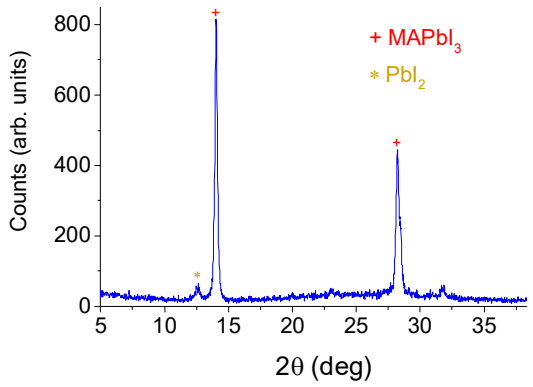


Figure 6.3 X-ray diffraction pattern for a vapour-deposited perovskite thin film on glass. The parameters used for the growth of this film are identical to those used for the devices.

Figures 6.4 a-c) show snapshots of the photocurrent spectra of the $MAPbI_3$ device at 15 K, 150 K and 290 K (blue solid lines). The spectra clearly show an energetic narrowing of the $MAPbI_3$ photocurrent onset from 290 K to 15 K as a result of reduced electron-phonon coupling (thermal broadening).[188]

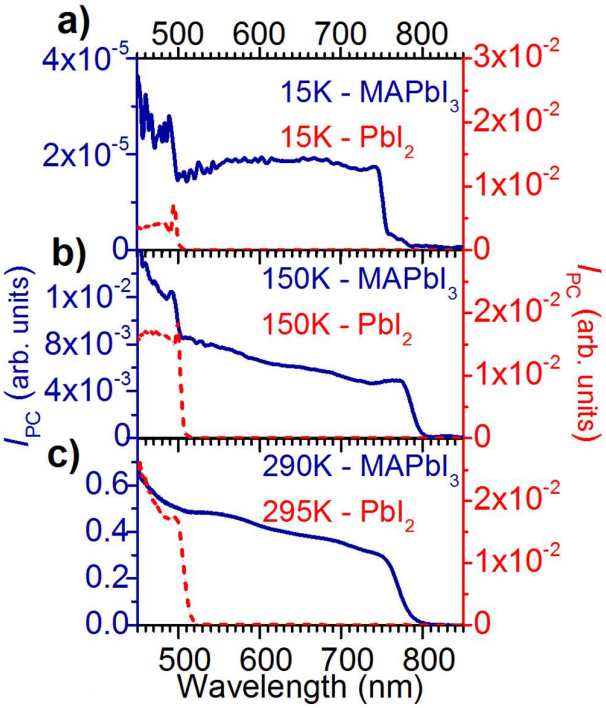


Figure 6.4. **a-c)** Photocurrent spectra of a $MAPbI_3$ device as shown in Figure 1a (blue) and a PbI_2 device (red-dashed) which has the same architecture as the one shown in Figure 1a except that $MAPbI_3$ is replaced with PbI_2 at a) 15 K, **b)** 150 K and **c)** 290 K. The $MAPbI_3$ device at 15 K and 150 K shows significant PbI_2 contribution to the photocurrent (I_{PC}), between 507 nm and 526 nm. Notably, the $MAPbI_3$ photocurrent increases by 4 orders of magnitude from 15 K to 290 K, whereas the increase of PbI_2 photocurrent is smaller.

In addition, the magnitude of the photocurrent I_{PC} increases substantially as the temperature is increased, in agreement with the already discussed behavior of the total current density, J_{sc}, observed in the current-voltage device characteristics (Figure 6.2). Interestingly, at low temperatures (15 K) an additional, sharp onset in photocurrent can be observed at 507 nm in the photocurrent spectra for the $MAPbI_3$ device (Figure 6.4a). This onset exhibits a red-shift with increasing temperature, reaching 510 nm at 150 K as shown in Figure 3b. The spectral position of the onset and the red-shift are comparable to those reported for the absorption onset of PbI_2.[187] Therefore, to verify that this

contribution to the photocurrent indeed originates from PbI_2, a device was fabricated for which the $MAPbI_3$ layer was replaced by a PbI_2 layer. The photocurrent spectra of the PbI_2-only device at 15 K, 150 K and 295 K are shown in Figure 3a-c as red dashed lines. The rise in photocurrent from the PbI_2 devices (red dashed lines) exactly matches the onset seen in the $MAPbI_3$ devices (solid blue lines) at 507 nm and 510 nm in Figure 6.4a and 6.4b, confirming the origin from PbI_2. At room temperature (Figure 6.4c), there is no obvious signature of a PbI_2 photocurrent onset in the $MAPbI_3$ device (blue line), most likely because the PbI_2 photocurrent is overwhelmed by the much stronger perovskite photocurrent at this temperature. Indeed, our photocurrent spectra for the PbI_2-only device (Figure 6.4, red dashed lines) clearly show that it can sustain a decent photocurrent between room temperature and 150 K that decreases as the temperature is reduced towards 15 K.

Fabrication processes have shown that the perovskite thin films can be affected by any remnant precursors such as PbI_2 or MAI.[89,192] Recently, perovskite solar cells consisting of remnant PbI_2 in in the perovskite thin film, show excellent PCE of 21.6%.[192] These results show that any remnant PbI_2 in the $MAPbI_3$ is able to play an active photocurrent generation role, even under normal operating conditions. Importantly, the $MAPbI_3$ device incorporates significantly less PbI_2 than $MAPbI_3$, yet it shows a clear signature in the photocurrent spectra at 510 nm. As mentioned earlier, this may be due to the loss in functionality of the organic charge transport layer, due to an increase in series resistance at such low temperatures.[178]

Our observation of photogenerated current from PbI_2 networks within $MAPbI_3$ helps explain previous reports that $MAPbI_3$ with a slight excess of PbI_2 improves solar cell performance.[191–193,196] Furthermore, Shih *et al.* have shown that $MAPbI_3$ devices with excess PbI_2 perform better when the PbI_2 is on the surface of the $MAPbI_3$ perovskite grain.[197] Based on the collective data presented, there are two processes that could occur, either concurrently or separately to explain the PbI_2 signal shown in figure 6.4. Firstly, there could be a homogenous network of PbI_2, through which photogenerated charge-carriers can be transported and then collected at electron and hole selective layers, which is possible as shown by the PbI_2-only device. Secondly as Holovský *et al.* have postulated, PbI_2 may create a type II heterojunction with the $MAPbI_3$, making it energetically more favourable for the holes to be transported into the $MAPbI_3$ and electrons to be transported into the PbI_2.[197,198] However, this process is thermally activated,[198] hence at low temperatures it will not be as effective. Our results imply that at low temperature, remnant PbI_2 in a $MAPbI_3$ device can produce photocurrent independent of $MAPbI_3$ and at room temperature PbI_2 is also capable of generating photocurrent. To understand the exact origin of the photocurrent observed of PbI_2 at different temperatures, in $MAPbI_3$ thin film devices, would require detailed investigation of the interface between $MAPbI_3$ and PbI_2.

Further analysis of the information on the operation of the $MAPbI_3$ photovoltaic device by contrasting the temperature-dependent photocurrent and absorption near their onsets (Figure 6.5). For this purpose, absorption spectra were taken of a film whose architecture resembles that of the device shown in Figure 6.1,

but without the silver electrode. There are three different regimes of contrasting behaviour.

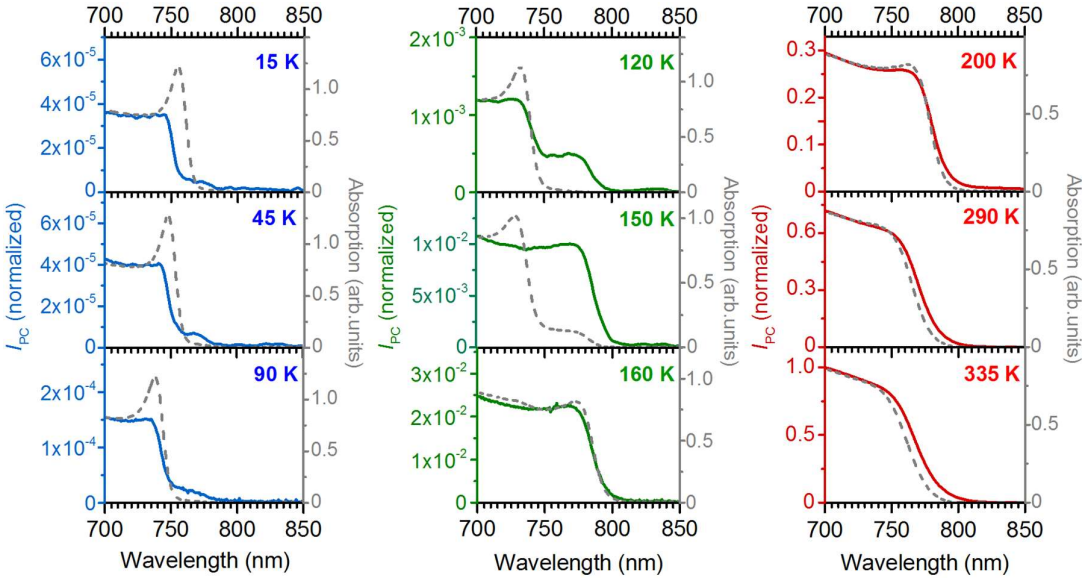


Figure 6.5. Temperature dependence of the photocurrent (I_{PC}) and absorption onset (dashed line) of the $MAPbI_3$ device. Here the reflection corrected absorption is of the full device architecture shown in Figure 6.1 without the Ag electrode. The photocurrent spectra were spectrally corrected using a calibrated silicon solar cell and normalised with respect to the 335 K spectrum. All measurements were made using a tungsten halogen light source.

Over the temperature range of 120-160 K (Figure 6.5b), there is significant blue-shift in the absorption spectrum which is characteristic of the tetragonal to orthorhombic phase transition in $MAPbI_3$, as previously observed in isolated $MAPbI_3$ films.[103] However, the photocurrent onset over this range shows that $MAPbI_3$ retains remnant tetragonal phase in the device that evidently supports an effective photocurrent. Even though the absorption spectra only indicate a small quantity of remnant tetragonal $MAPbI_3$, a significant amount of red-shifted photocurrent onset can be observed near the energy associated with the

band-gap of the tetragonal phase. Such remnants of the tetragonal phase $MAPbI_3$, must therefore be able to form a crystalline network that allows for photogenerated charges to be extracted at low temperatures. Figure 6.5a shows that in the temperature range from 15-90 K, the photocurrent onsets become dominated by a trade-off between free-charge and exciton formation. In this temperature range, there is a significant blue shift of the photocurrent onset compared to the absorption onset and the absorption onset shows notable excitonic absorption features. Therefore, in a device that is under no bias, i.e. under short circuit conditions, there would be negligible photocurrent contribution from dissociated excitons unless the thermal energy exceeds the exciton binding energy.[199]

Thus, by comparing the peak of the exciton and the onset of photocurrent at low temperature, as shown in Figure 6.6, an estimate of the lower bound on the exciton binding energy (E_B) at 15 K to be 9.1 meV, which is consistent with previous magneto-optical experiments which found a value of E_B =16 meV at 4 K.[199]

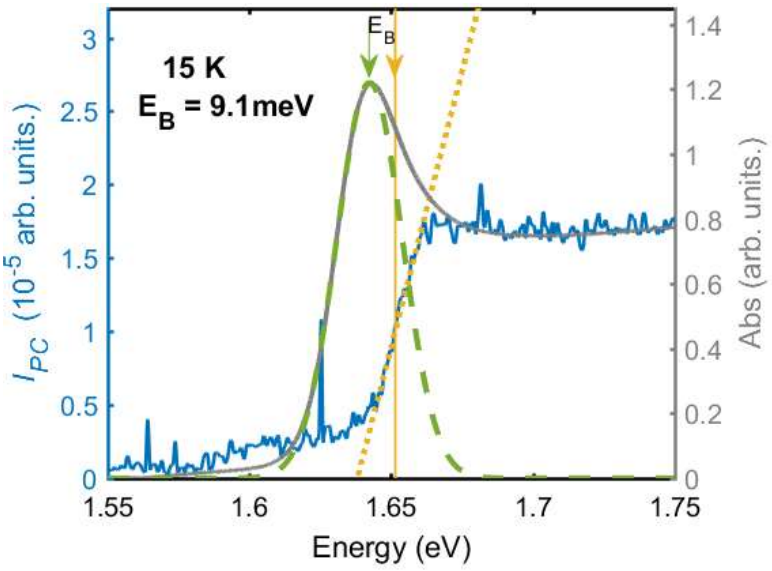


Figure 6.6) Photocurrent and absorption spectra of a $MAPbI_3$ device as depicted in Figure 4. A simple estimate of the lower bound of the exciton binding energy (E_B) was determined by the difference between midpoint of the photocurrent onset and the peak of the exciton in the absorption onset. The exciton was fitted with a Gaussian function using MATLAB. At 15 K, low thermal energy and zero applied bias ensure that most excitons will not dissociate (see figure S7) and hence will not contribute to the photocurrent. Therefore, the photocurrent onset represents the onset of the continuum states in the perovskite semiconductor. *The gaussian fit was carried out by both Jay Patel and Christopher Davies*

In contrast, for temperatures above 160 K, the photocurrent onset first overlaps with the absorption onset, then even shifts to slightly longer wavelength (Figure 4c). Hence in this temperature range, photoexcitation yields mostly free charges, as confirmed by our Saha-Langmuir analysis (presented in Figure 6.7).[200,201] At temperatures above 160 K, excitons have sufficient thermal energy to dissociate, allowing photocurrent to be collected from dissociated electrons and holes.

The equation used is

$$\frac{x^2}{1-x} = \frac{1}{n}\left(\frac{2\pi\mu k_B T}{h^2}\right)^{\frac{3}{2}} e^{-\frac{E_B}{k_B T}} \quad . \tag{6.1}$$

Where E_B is the exciton binding energy, k_B is the Boltzmann constant, T is the temperature, μ is the effective mass of the exciton, h is the Plank's constant, n is the total excitation density and x is the fraction of free charge-carriers over the total density of excitation.

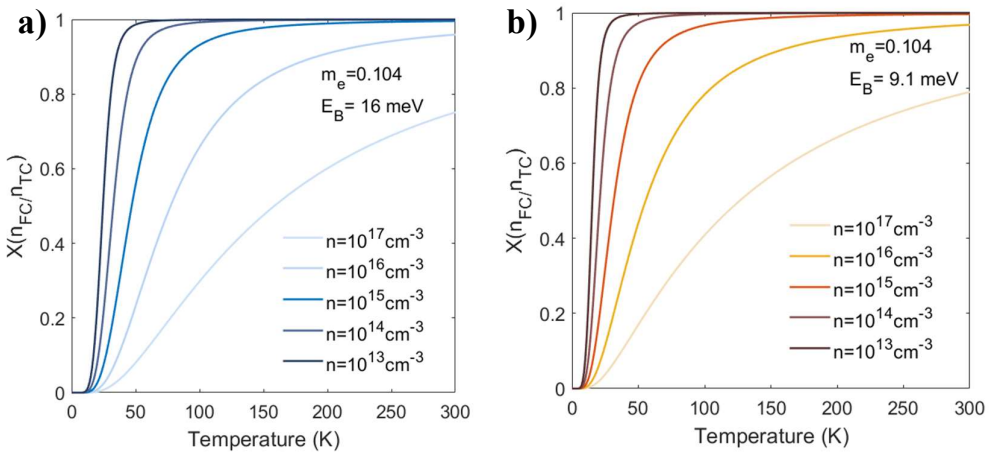


Figure 6.7) Simulation of the free charge fraction (X) over the total excitation density (n). The model is based on the method presented in Ref. [200]. The total excitation density at AM1.5, 1 sun is between 10^{13} and 10^{15} cm^{-3} (ref. [200]. The reduced mass of the exciton is 0.104 m_e (ref. [199]) and the exciton binding energy is **a)** based on magneto-optical experiments (ref. [199]) **b)** calculated from the spectra shown in Figure 6.6

Curiously, the onset of the photocurrent is slightly red-shifted in relation to the onset of the absorption for temperature above 290 K, which is attributed to an optical cavity effect within the perovskite multilayer device.[202–204] Because the absorption coefficient of $MAPbI_3$ is high for photons well above its bandgap, a high charge-carrier density is photogenerated mainly on the side of the perovskite layer closest to the semi-transparent contact (FTO).[202,205] However,

longer-wavelength photons near the band-edge will generate a much more uniform charge density profile through the $MAPbI_3$ layer, and it has been observed previously that uniform charge distributions can result in more effective collection of photocurrent in $MAPbI_3$ compared with when electron-hole generation is concentrated close to just one $MAPbI_3$ interface of a planar heterojunction device.[202,203,206] Thus, the photocurrent spectra exhibit an enhanced contribution towards the low-energy side of the perovskite bandgap. Therefore, the correlation between photocurrent and absorption spectra provides an illuminating insight into the mechanisms by which absorbed photons are converted to photocurrent.

6.3 Summary

In conclusion, the temperature-dependent J_{sc} and V_{oc} for a $MAPbI_3$ solar cell have been tracked from 15 K to 350 K. Both the J_{sc} and V_{oc} peak near 200 K, where after they deteriorate steeply at lower temperatures, but only decreasing gradually towards higher temperatures. By comparing photocurrent spectroscopy and absorption spectroscopy on the same solar cell architecture the exciton binding energy can be estimated for $MAPbI_3$ to be greater than 9.1 meV at low temperature, and show that at higher temperatures, low-energy photons that generate uniform charge-density profiles dominate the photocurrent onset. Furthermore, photocurrent spectroscopy has proven a vital tool for understanding the influence of remnant precursors in the perovskite to the total device photocurrent. PbI_2 may contribute to the total photocurrent of the device,

hinting at the role of remnant PbI_2 in the $MAPbI_3$ thin films. Overall, $MAPbI_3$ solar cells have shown optimal device parameters at -73° C, which shows that only small improvements may be required in the device architecture to render these solar cells a viable, cheaper alternative for space applications. With the advent of perovskite semiconductors consisting of many mixtures of cations, metals and halides, further investigation will be helpful to see how compositional differences, as well as changes in charge extraction layer materials, may affect the temperature-dependent device performance.

Chapter 7

The Effect of Ultraviolet Radiation on Organic Photovoltaic Devices

Whilst state of the art organic photovoltaics devices can be encapsulated to withstand air and moisture, they are currently still susceptible to light-induced degradation, leading to a decline in long-term efficiency of the devices. In this study, the role of ultraviolet (UV) radiation on a multilayer organic photovoltaic device is systematically uncovered. By applying long pass filters to remove different parts of the UV portion of the AM1.5G spectrum, it is found that two main photodegradation processes occur in the OPV devices.

7.1 Introduction

Currently, the most significant hurdle to the commercialisation of OPV devices is their long-term stability, which must be improved to ensure they are an effective technology to be used for lightweight, semi-transparent and portable photovoltaic devices. Ambient air, specifically moisture and oxygen, have been observed to impact the stability of OPV devices.[207–209] Exposure to moisture and oxygen during device processing can cause a significant change in the morphology of the BHJ interface, leading to a reduction in device performance.[207] Nevertheless, by processing devices in an inert atmosphere and through recent improvements in encapsulation techniques, the impact of ambient air on the degradation of OPV devices has been reduced.[208,210] Despite protection from air, OPV devices under constant light illumination show a sharp initial decrease, followed by a slower and steady decline in the power conversion efficiency (PCE). This initial period has been termed the 'burn-in period', during which devices show a decrease in current-voltage (*JV*) parameters such as the short circuit current density (J_{sc}), open-circuit voltage (V_{oc}), fill factor (FF) and power conversion efficiency (PCE).[210–212] The photoactivated changes that occur in encapsulated OPV devices affect the micromorphology of the BHJ and initiate unwanted chemical reactions of either the donor or acceptor, mainly affecting the short-circuit current density (J_{sc}) and the open-circuit voltage (V_{oc}).[211,213–218] It is well known that fullerenes form oligomers when exposed to light, causing the PCE to drop, as such fullerene oligomers exhibit shorter exciton diffusion lengths and lower charge carrier mobilities compared to the initial isolated fullerenes.[214,219] However, oligomerization can potentially be avoided by

ensuring that the BHJ comprises of crystalline fullerene domains forming a blend with the donor polymer.[215]

OPV's are excitonic at room temperature owing to the enhanced columbic interaction between the electrons and holes, resulting in an exciton binding energy (E_b) that is in the order of ~100meV.[220,221] At the interface between the acceptor and donor material, the acceptor material, usually fullerene based, has a higher electron affinity than the donor material, which creates an energy offset that allows electrons to overcome the exciton binding energy.[222] However, a proportion of dissociated charge-carriers may continue to interact with each across the interface such that frontier orbital overlap in the allowed electronic states between the highest occupied molecular orbital of the donor ($HOMO_{donor}$) and the lowest unoccupied molecular orbital of the acceptor ($LUMO_{acceptor}$) overlap.[189,223–227] Such interfacial charge transfer states (CT) are bound states formed between a hole residing on the donor polymer, and an electron on the acceptor. Random diffusion of a CT excitation in the vicinity of the interface, assisted by the internal field, will eventually lead to either charge separation or recombination.[228,229] The energy of the CT state, E_{CT}, can be deduced from absorption- and emission-based spectroscopic techniques,[230] however, the intensity of the photocurrent signal from the CT state is usually orders of magnitude lower than that associated with excitons residing on only the donor polymer.[231] An accurate assessment of such CT states is essential, because the choice of the donor and acceptor molecules and the morphology of the BHJ can significantly influence the spatial delocalisation of the CT state, which will alter the dissociation efficiency of electrons and holes into free carriers.[229,232–235]

A typical OPV device consists of a thin-film stack that includes the photoactive layer (PAL), the electrodes, and the charge-transport layers that ensure selective extraction of electrons and holes towards the opposing electrodes. An example of a typical hole transport material is PEDOT:PSS, notable for its transparency in the visible spectrum and its high electric conductivity.[236–238] Photodegradation, in particular ultraviolet (UV) induced photodegradation, may therefore affect a multitude of layers in an OPV device, rather than just the PAL. For example, Sapkota *et al*. observed that when OPV devices were exposed to UV radiation for 2000 hours, the electrical conductivity of the PEDOT:PSS hole transport layer was drastically reduced, while the PAL showed little degradation.[239,240] To combat UV induced photodegradation, UV-filters have been placed either within the device or as a filter on top, which resulted in a significant improvement in photostability of encapsulated OPV devices.[241,242] An investigation of light-induced photodegradation, with a particular focusing on the changes in the sub-bandgap photocurrent spectra during the burn-in period, has the potential to clarify how standard solar and UV-filtered solar light causes photodegradation in the different layers of an OPV device. Changes in the sub-bandgap photocurrent spectra can be indicative of effects on the micromorphology of the BHJ, whilst any degradation observed in the overall photocurrent spectra can elucidate macroscopic alterations of the charge transport layers.

This study utilises the highly sensitive technique of Fourier transform photocurrent spectroscopy (FTPS) to investigate spectral changes in the external quantum efficiency (EQE) induced in organic photovoltaic BHJ devices

during mid-term exposure to filtered and unfiltered light from a solar simulator. the photoinduced degradation in short-circuit current is tracked during the burn-in period while illuminating the device with an air mass 1.5 (AM1.5) spectrum continuously for 18 hours and periodically measuring the EQE spectra. By taking advantage of the sensitivity of FTPS, clear changes can be resolved in the sub-bandgap photocurrent during device aging with UV-filtered light. Using electroluminescence spectroscopy, CT state energy E_{CT} =1.31eV is identified and it is concluded that the observed changes in the sub-bandgap photocurrent originate from a mechanism coupled to the CT state, most likely oligomerization of the fullerenes. Furthermore, the exposure of unfiltered light leads to photodegradation that affects the whole photocurrent spectrum, which is attributed to degradation processes affecting the electrode materials.

7.2 Results and Discussion

Figure 7.1a illustrates the structure of the OPV devices investigated in this study. The donor material (PBTZT-stat-BDTT-8) is based on a conjugated polymer whose backbone consists of substituted thiophenes with side chains enhancing the solubility of the polymer.[243] The acceptor molecule is phenyl-C_{61}-butyric-acid-methyl-ester (PCBM), a functionalised fullerene that is commonly used in BHJ films because of its solubility in a wide range of solvents, suitable energetic alignment with the donor polymer, and a delocalised LUMO allowing for favorable electron mobilites.[115,244,245] The material combination used in the photoactive layer has previously been shown to be versatile in different solvent systems, device architectures and to yield OPV devices with power conversion

efficiencies (PCE) of 9.3%.[121] Electron and hole extraction layers were based on polymers PV ET002 and PEDOT:PSS.[121]

Characterisation of solar cells under illumination is based upon a light source that represents the spectral irradiance upon earth when the sun is 48.19° from the zenith. This so-called Air Mass 1.5G (AM1.5G) spectrum is corrected for solar irradiation that is absorbed or scattered when light travels through the earth's atmosphere. While the atmosphere absorbs a significant portion of the UV radiation from the sun, a small quantity still reaches the earth's surface (see Figure 3.5).[1,246] To investigate the effect of UV radiation on OPV devices, long pass (LP) filters are used to systematically block different categories of UV light from the simulated AM1.5G (AM1.5 light) spectrum generated by a solar simulator (Figure 3.5). ISO classification splits UV light into two distinct ranges within the AM1.5G solar spectrum, UVB ($280 \leq \lambda < 315$ nm) and UVA ($315 \leq \lambda < 400$ nm).[247] Two long-pass filters, LP 331 nm, which filters only UVB light, and LP 400 nm, were used, which filters both UVB and UVA from the simulated AM1.5 solar spectrum. Figure 3.5 shows the relative intensities of both the UVB and UVA components in the AM1.5G solar spectrum, together with the transmission functions of the long-pass filters.

To investigate the mechanism by which light causes device degradation, the changes in the EQE spectra as a function of illumination time over 18h is tracked, for the three scenarios of unfiltered, UVB filtered, and UVB+UVA filtered light. Figure 7.1b shows the mean initial and the final values of the integrated short circuit current densities (J_{sc}) extracted from the EQE spectra. Initial J_{sc} values vary between the three filtration conditions because of differences in the reduction of photon flux. When both UVB+UVA components

are eliminated from the spectrum, the initial J_{sc} is significantly lowered, while for filtration of only UVB, little change is evident compared with full AM1.5 exposure. These differences simply reflect the fact that there is a very small component of UVB light contained in the AM1.5G spectrum (see Figure 3.5) which will, in any case, also be partly absorbed by the glass substrate and the indium tin oxide electrode. As a result, the introduction of a 331-nm long-pass filter (to filter UVB) also does not significantly reduce the rate of device degradation, as evident from Figure 7.1b.

To illustrate how differences in spectral filtration of the incident light affect the photocurrent for different incident photon energies, Figure 7.1c-e shows the EQE spectra recorded for three devices, that were constantly illuminated by 0.7 sun (70 mW cm^{-2}) unfiltered AM1.5 light, only UVB filtered AM1.5 light, and both UVB+UVA filtered AM1.5 light. The slight difference in the spectral profile of the EQE between the devices is because the devices are in essence low finesse electro-optical cavities.[248] Hence, slight changes to the thickness of the photoactive layer will results in a different optical interference pattern within the device.[248] It is evident that under all three conditions, the EQE spectra shift downwards over the duration of the light exposure.

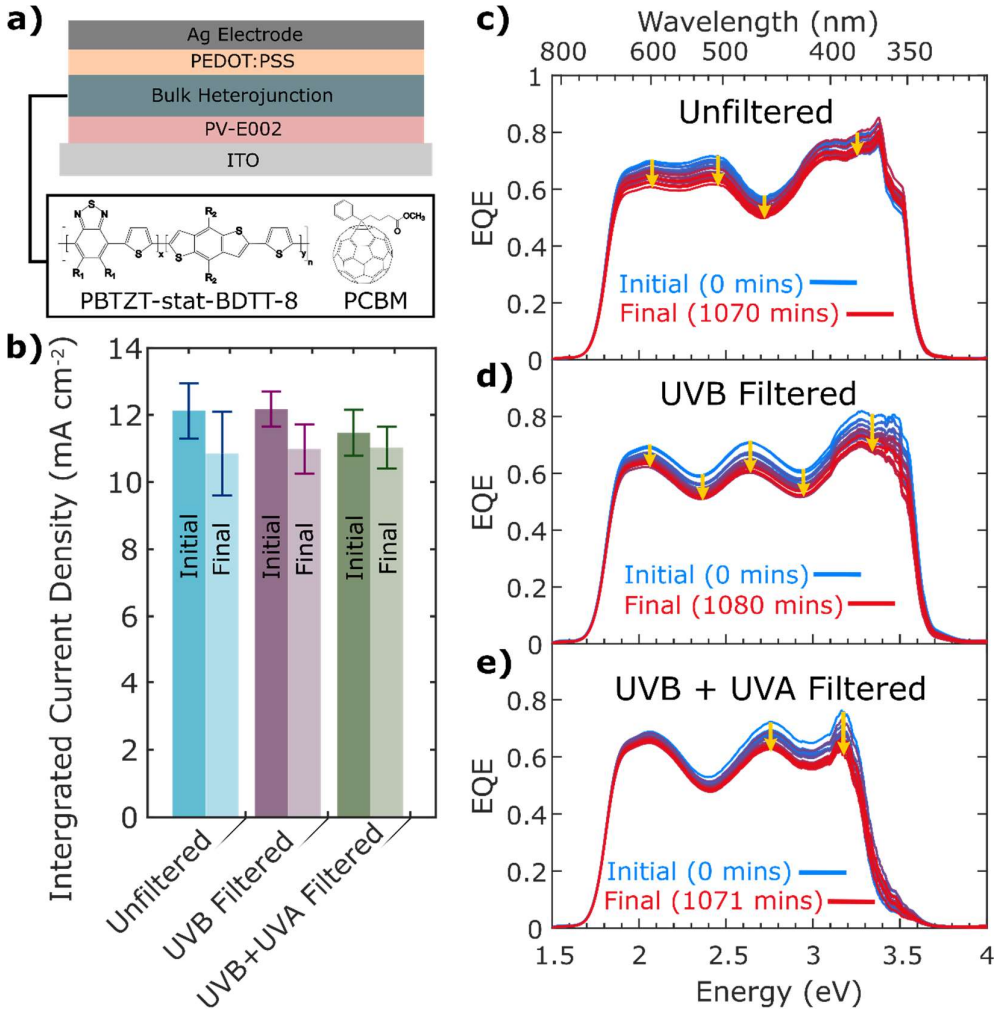


Figure 7.1 a) The device schematic for the OPV devices investigated in this study. The bulk heterojunction consists of the donor polymer PBTZT-stat-BDTT-8 and PCBM, and the electron and hole transport layers of polymer PV E002, and PEDOT:PSS, respectively, as described previously.[121] **b)** The mean short circuit current densities (J_{sc}) deduced from the initial EQE spectra and the final spectra after 1070 min of exposure to AM1.5 light with or without filters (averaged over three or more devices). **c-e) c)** Changes in external quantum efficiency (EQE) when the device is illuminated with AM1.5, 0.7 Sun (70mW cm-2) light that is **c)** Unfiltered **d)** UVB filtered ($280 \leq \lambda < 315$ nm) by long pass(LP) H-BaK7 glass 331nm (331-GY Comar Optics) ce) UVB+UVA filtered ($280 \leq \lambda < 400$ nm) with long pass (LP) Schott glass 400nm (GG-400 Thorlabs). The arrows highlight regions where significant reduction in EQE occurs. *The devices were fabricated by Priti Tiwana*

The device exposed to unfiltered AM1.5 light shows the largest decrease in EQE over 1070 minutes, with the device exposed to just UVB filtered light again showing very similar effects. However, for the device exposed to UVB+UVA filtered AM1.5 light degradation is much reduced. In addition, while both unfiltered and UVB-filtered light exposure results in an overall downwards shift in EQE across the *whole spectrum*, the device exposed to UVB+UVA filtered AM1.5 light, exhibits a larger decrease in EQE at higher photon energies, and a minimal reduction in EQE at photon energies below 2.5 eV. Therefore, it appears that light with wavelength shorter than 400nm triggers one UV-activated degradation mechanism that causes an overall reduction in EQE across the whole spectrum, while a second photodegradation process can occur in the presence of light even without a UV component, which leads to a decrease in EQE only at higher photon energies. The latter process is linked to dimerization of PCBM, and hence it mostly affects the EQE at photon energies above 2.25 eV (λ=550 nm) where PCBM absorbs.[249] Previous studies have shown that dimerization of PCBM will decrease the exciton diffusion length and charge-carrier mobility, leading to a reduction of device J_{sc}.[214,215,219,250,251] Therefore, such dimerization can significantly affect both light absorption in the PCBM spectral region and charge extraction from the device.

The temporal dynamic of device degradation is analysed by plotting the integrated J_{sc}, extracted from the EQE spectra, for the devices as they are exposed to unfiltered AM1.5 and UVB+UVA filtered AM1.5 light over 18 hours (**Figure 7.2**). The study now focuses on these two conditions only, because the

filtration of only UVB light was shown to result in little change compared with exposure to unfiltered AM1.5 light.

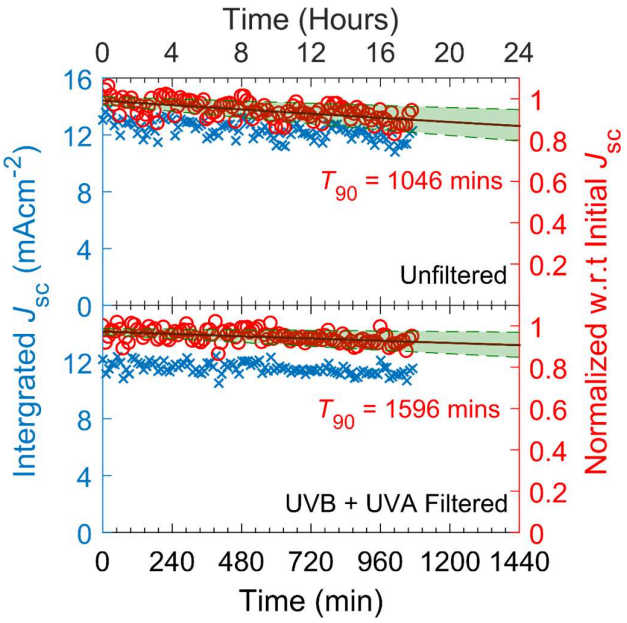


Figure 7.2. Change in spectrally integrated current density (J_{sc}), blue crosses, calculated from integration of the EQE spectra (Figure 7.1) and the J_{sc} normalized with respect to the initial J_{sc} , red circles, for OPV devices exposed to unfiltered and UVB+UVA filtered AM1.5 light. The normalised data are fitted with the expression Ae^{-Bt}, with A and B as fitting parameters. The values T_{90} indicate the time taken for the devices to reach 90% of the initial J_{sc}, as extracted from the fits. The green shaded region indicates 98% confidence interval of the fit.

Figure 7.2 shows that the rate of photoinduced degradation is slowed when UVB and UVA light is filtered from the AM1.5 spectrum. While both devices exhibit the typical[211,252,253] burn-in period of OPV devices within the first 10 hours, the decrease in J_{sc} proceeds at different rates, similar to trends previously observed in power conversion efficiencies.[250,254] To obtain numerical values for the degradation rates, an exponential function was fitted to the integrated J_{sc}, and extracted the time T_{90} taken for the J_{sc} to reach 90% of its initial value.[209,255] It

was found that for UVB+UVA filtered AM1.5 light, the device exhibits a T_{90} lifetime of ~1600 mins, 53% longer than for the device exposed to unfiltered AM1.5 light (~1050min). Therefore, whilst the addition of a long pass 400-nm filter reduces the initial J_{sc} through the reduction of photon flux, this detrimental effect is largely compensated after the first ~18h because of the reduced rate of burn-in degradation. To explore further why UVB+UVA filtered light may still cause a sizeable amount of degradation to the devices, the spectral changes occurring in EQE as a result of such illumination are closely examined. Figure 7.1c already demonstrated that the device exposed to UVB+UVA filtered AM1.5 light displayed a reduction in EQE at higher photon energies where PCBM absorbs, suggesting a link with changes in this component. To examine whether this reduction in EQE is caused by the oligomerization of PCBM, any additional changes that may occur below the band gap E_g, where CT state photocurrent features may contribute is investigated.[189,223,224] Because the CT state arises from an overlap between the frontier molecular orbitals of the acceptor and the donor, even a minute change in the morphology of the heterojunction, caused e.g. by the oligomerization of PCBM, will affect the number of free charges generated from the CT state.

Figure 7.3 displays the sub-band gap EQE of the initial and final EQE spectra of devices exposed to unfiltered AM1.5 light, and alternatively to UVB+UVA filtered AM1.5 light. A notable difference in the initial and final photocurrent spectra recorded under the two illumination conditions can be clearly seen above the noise floor once the spectra are plotted on a semi-logarithmic scale, between the ranges of 1.2 eV and 1.6 eV. While the device exposed to UVB+UVA filtered

AM1.5 light suffers a reduction in sub-bandgap photocurrent after 1070 min, the device exposed to unfiltered AM1.5 light shows no change.

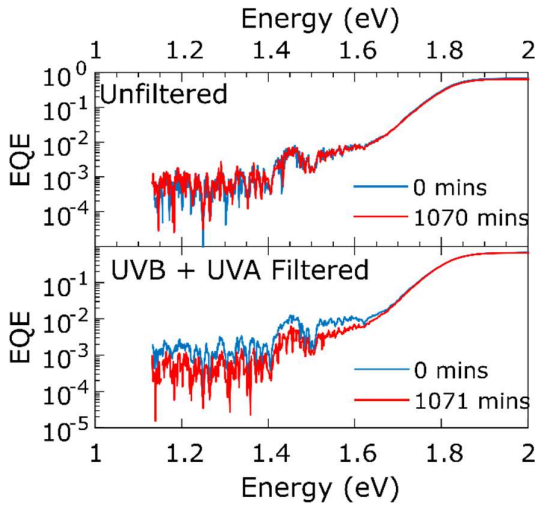


Figure 7.3. Sub-bandgap changes in the EQE, as evident when spectra shown in Figure 7.1c are plotted on a semi-logarithmic scale. A reduction in photocurrent from the sub-bandgap region is evident when the device is exposed to UVB+UVA filtered AM1.5 light (bottom), while no change is found when the device is exposed to unfiltered AM1.5 light (top).

To confirm whether the observed sub-bandgap photocurrent is indeed generated by dissociated charges from the CT state, the electroluminescence (EL) spectra was recorded for a device, thereafter the recorded features were correlated with features observed in the EQE spectra.[256] During EL, electrons are injected from the electrodes into the $LUMO_{acceptor}$ and holes into the $HOMO_{donor}$ levels, leading to a gradual population of the available density of states, starting with the lowest-energy states.[257,258] Under forward bias applied to the device, charges will diffuse towards the heterojunction where they may be captured into CT states through which they may radiatively recombine.

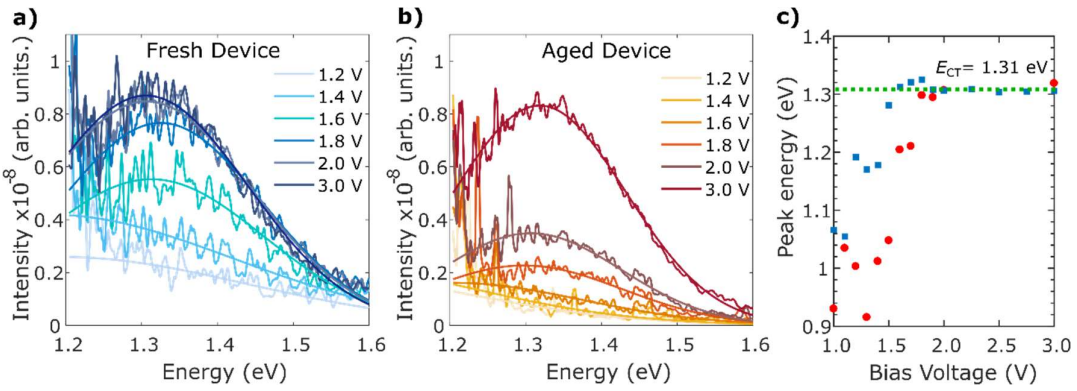


Figure 7.4. Electroluminescence spectra and the corresponding Gaussian fits, for an OPV device under different bias voltages recorded for the case that the device was **a)** fresh, i.e. without any aging **b)** aged under UVB+UVA filtered AM1.5 light for 1070 minutes. **c)** The peak energy of the EL versus the applied bias, extracted from Gaussian fits to the EL spectra, for the fresh device (blue) and the aged device (red).

The EL spectrum generated at low biases will represent the distribution of states that correspond to the charge transfer state, where the peak will represent the energy E_{CT} of the CT state.[256] **Figure 7.4** shows the bias-dependent EL spectra recorded for both a fresh device and an aged device, which had been illuminated for 1070 minutes with a UVB+UVA filtered AM1.5 light. As the voltage is increased, more charge-carriers are injected into the device leading to an increase in radiative recombination events and hence an observed rise in EL intensity. To determine the difference in energy between the emitting excited state and the ground state, Gaussians were fitted to the EL spectra to determine the peak EL energy, with the resulting values shown in **Figure 7.4c** as a function of the bias voltage. As the bias voltage is increased from 1.0 to 1.5 V, the peak energy of the EL spectrum rises because minority tail states associated with the CT state are increasingly populated until they are filled. However, beyond a certain bias (1.6 V for the fresh and 1.8 V for the aged device)

the peak energy stabilises, and the only further change in the EL spectra (Figure 7.4a and 7.4b) is a rise in peak intensity. Hence, at this point, the stabilised EL spectra can be attributed to the prominent CT state, which has a peak energy of E_{CT} = 1.31 eV, as apparent from the bias-independent regime shown by the dashed green line in Figure 7.4c.

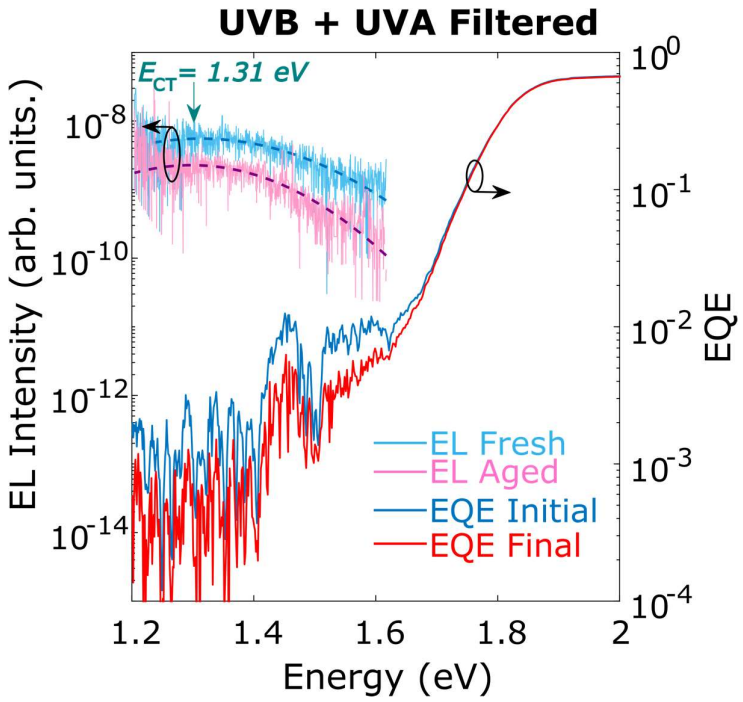


Figure 7.5. Electroluminescence (EL) spectra and solar cell EQE spectra displayed together on a semi-logarithmic scale. The blue lines represent the initial scan taken on a fresh device, and the red and pink lines represent the final spectra taken after the devices had been exposed to UVB+UVA filtered AM1.5 light for 1071 minutes. The EL of the fresh and aged device were taken for an injection current of ~17.5 mAcm^{-2} at stabilised conditions (1.6V for fresh and 1.8V for aged devices) and show peak luminescence near 1.31 eV and 1.30 eV respectively.

To correlate the extracted stabilised EL spectra with the EQE spectra, **Figure 7.5** displays spectra, both in the same graph, for a fresh device and after it has been aged under UVB+UVA filtered AM1.5 light for 1071 minutes. The graph

shows clear correlations, both in terms of the spectral positions of the features observed in the EL and sub-gap EQE, and the changes found upon aging. Both features are centered around the energy E_{CT}= 1.31 eV of the CT state, and both show a similar relative decline in signal intensity as the device is aged. It is therefore demonstrated that device aging under UVB+UVA filtered AM1.5 light has a direct effect on the CT state at the PBTZT-stat-BDTT-8:PCBM interface.

The above results suggest that there are two degradation mechanisms operating during the initial burn-in process, one which does not require a UV component of the light and affects mostly the high-energy end of the EQE spectrum, and another, which reduces the EQE across the spectrum in the presence of UV.

As mentioned above, the observed photodegradation in the presence of UVB+UVA filtered AM1.5 light is predominantly caused by changes in the PCBM component that also affect the CT states formed at the PBTZT-stat-BDTT-8:PCBM heterojunction. The cause of this is attributed to light-induced change to oligomerization of PCBM, which has been shown to reduce both exciton diffusion lengths and charge carrier mobilities,[213–215,219,250] lowering charge generation and extraction. Oligomerization of PCBM will also lead to a change in the micromorphology of the BHJ which may either reduce or enhance the interaction between the frontier molecular orbitals of the donor and acceptor materials, thus affecting the density of CT states.[235] In the case of the heterojunction investigated in this study, such effects are observed via the reduction in the sub-bandgap photocurrent after the device has been aged with UVB+UVA filtered AM1.5 light (Figure 7.3). Through parallel measurements of EL spectra (Figure 7.4) under forward bias, it is shown that the spectral shape

of the CT emission peak (E_{CT}=1.31eV) and changes in the intensity with aging correspond well with those observed in EQE, confirming the assignment of these features to a CT state. The overall reduction in EL intensity as the device is aged is consistent with an increase in non-radiative charge-carrier recombination caused by a degraded heterojunction.[256] Together with the reduction in EQE at higher photon energies attributed to PCBM[250] (Figure 7.1), the decline in photocurrent from the CT state demonstrates that such aging causes a change in the micromorphology of the heterojunction, most likely caused by the oligomerization of PCBM. Secondly, as devices are exposed to the full, unfiltered AM1.5 spectrum, which includes significant UVB+UVA components, additional degradation pathways are observed. As shown in Figure 7.2, UV the degradation rate of the J_{sc} becomes significantly more rapid, than for devices exposed to UVB+UVA filtered AM1.5 light. Moreover, exposure to unfiltered AM1.5 causes an overall decrease in EQE over the whole spectrum (Figure 7.1c).

Taken together, these observations suggest that an additional mechanism becomes operational that broadly affects light absorption or extraction relatively independently of the energy of the absorbed photons. Such a mechanism could therefore be linked to changes rendering either the main light absorber (PBTZT-stat-BDTT-8), the hole extractor (PEDOT:PSS), or the electron extractor (PV E002) layer less effective. Since there are no significant changes in the transmission spectra for a thin film of only the photoactive layer (PBTZT-stat-BDTT-8:PCBM, Figure 7.6) upon exposure to light, it is likely that

photobleaching of this layer is unlikely to be the cause of the reduction in photocurrent.

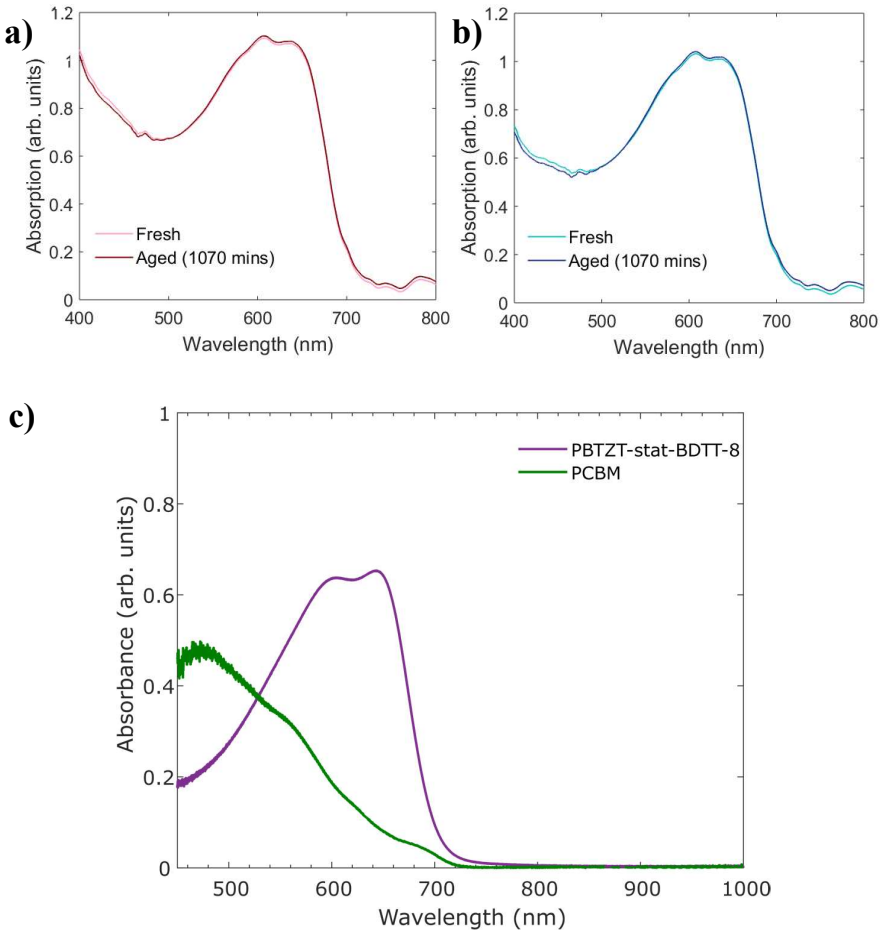


Figure 7.6. Ultraviolet-visible absorption spectra of the bulk heterojunction films containing PBTZT-stat-BDTT-8 and PCBM when illuminated with **a)** unfiltered **b)** UVB + UVA filtered AM 1.5 light before (fresh) and after 1070 mins (Aged). **c)** Absorption spectra of PBTZT-stat-BDTT-8 and PCBM on Quartz.

Therefore, the broadband decrease in the EQE spectra observed when devices are exposed to UV radiation, most likely arises from the photodegradation of the transport layer closest to the transparent electrode. Encapsulated OPV devices have previously exhibited significant J_{sc} losses when exposed to UV light,[239]

which was shown to be primarily caused by a drop in electric conductivity of the PEDOT:PSS hole transport layer incorporated into the inverted device architecture used. By convention of this thesis, an inverted device architecture employs the hole transport layer at the front of the device (closest to the transparent electrode) whereas a normal device architecture employs an electron transport layer at the front. Since most polymers have a high absorption coefficient in the UV, polymer-based charge transport layers close to the transparent electrode are much more susceptible to UV-induced degradation than those further at the back of the device. The device architecture employed in this study also uses PEDOT:PSS, however in a normal device configuration, meaning that PEDOT:PSS is protected by the photoactive and electron transport layers, which will UV-filter the light. However, the electron transport layer (polymer PV E002) is the first to face the incident light and will be susceptible to degradation under UV.[259,260] Such effects are prominent in polymeric semiconductors: Street *et al.* have shown that in conjugated polymers, UV radiation induces hydrogen-related defects 50 times faster than UV-filtered light.[261,262] Therefore, to prevent the photodegradation of polymeric transport layers closest to the front of the device, UV filtration, as shown in Figure 7.2, would be a simple but effective method to decrease the degradation during the burn in period. The long-pass filter with 400-nm cut-off, employed here, effectively filters all UV radiation, and yields a 53% increase in the T_{90} lifetime of the device (Figure 7.2).

For the case of device exposure to unfiltered AM1.5 light (Figure 7.3) for 18h, there is no substantial change observed in the sub-band gap photocurrent. This

is most likely the result of two counteracting effects on the sub-gap electronic states that roughly cancel over the observation period. Exposure of an OPV device to UV light results in the breaking of C-H bonds and the formation of C dangling bonds,[259,263] which has been found to create new trap states at the donor/acceptor interface.[210,259–261] Therefore, the reduction in the CT state photocurrent cause oligomerization of PCBM is most likely masked by simultaneous formation of sub-bandgap electronically allowed states following exposure to additional UV light.

In summary, UV protection of polymer-based charge transport layers that prominently face the sun light, and prevention of PCBM oligomerization, will both be necessary for the realisation of long-life organic solar cells. Full replacement of fullerenes as the electron acceptor may be a viable strategy to address the former issue, given that significant advances have recently been made in the design of new non-fullerene acceptor materials.[215,245,264–266] The study also demonstrates the need for photostability assessments of solar cells based on new photoactive materials both under unfiltered and UV-filtered AM1.5 light, to thoroughly analyse suitability of any material system for long-term use.

7.3 Summary

A systematic investigation has been conducted to probe the effect of light exposure on OPV devices by employing the sensitive technique of Fourier transform photocurrent spectroscopy, focusing on the first 18 hours of the burn-in process. Blocking both UVB and UVA components significantly slows down

the rate of degradation of the short-circuit current, with the device's T_{90} lifetime increased by 53%. The analysis of the changes in EQE spectra reveals two degradation process that occur during the burn-in period. The first photodegradation mechanism is initiated in the presence of UV light and causes a significant reduction of EQE over the whole solar spectrum, which can be attributed to UV-activated chemical changes in the polymer-based transport layer closest to the transparent electrode. The second observed photodegradation route is activated even in the presence of UV-filtered solar light, and manifests through a reduction in EQE predominantly at high photon energies. Analysis of the changes in sub-gap EQE and EL, suggests that there is oligomerization of PCBM, which leads to a change in the micromorphology of the BHJ. Overall, the analysis suggests that placement of a UV-filter in front of the OPV device and replacement of fullerenes with more photostable electron acceptor molecules may allow OPV devices to progress towards the long-term stability required for commercialisation.

Chapter 8

Conclusions and Outlook

This thesis has predominantly investigated hybrid metal-halide thin films fabricated using vapour deposition. The first investigation reveals the dynamic changes that occur when a bilayer thin-film of CH_3NH_3I and PbI_2 mix to form $MAPbI_3$ via solid-state diffusion and clearly elucidates the role of moisture in the crystallisation process. Vapour deposition was shown to be the ideal fabrication method to reveal the role of moisture, as the technique requires no use of solvents and the substrate temperature can be significantly cooled down. In vacuum, absorption measurements displayed a clear transition of the film changing from PbI_2 to $MAPbI_3$ when the thin-films were heated to room temperature, indicative of CH_3NH_3I diffusion into PbI_2. However, there was little to no observable change in the IR spectra, indicating that the perovskite had not completely formed. When the films were exposed to air, the C-H and N-H bond vibrations shifted towards the frequencies that corresponded with C-H and N-H bond vibrations in a $MAPbI_3$ thin film, signalling that the bilayer film had completely crystallised into a $MAPbI_3$ thin film.

The novel method to stop solid-state diffusion by cooling a bilayer film during the deposition process is significant. Currently the most efficient perovskite-based photovoltaic devices incorporate perovskite compositions that encompass a variety of different anions and cations. Following the diffusion of a variety of

precursors will allow for a greater understanding in the formation dynamics of complex perovskite compositions. Additionally, extraction of diffusion rates from absorption spectroscopy may help determine the origins of the thermal or environmental instability that may arise from incorporating new ions.

The experiments in Chapter 5 focus on co-evaporated thin films of $MAPbI_3$, that were incorporated in seven different device architectures. The results of the device characterisation showed that the devices incorporating only TiO_2 as the electron transport layer exhibit far more *J-V* hysteresis than those incorporating PCBM. High-resolution transmission microscopy images showed that there was significantly more amorphous perovskite at the interface with TiO_2 and a crystalline perovskite interface with PCBM. The results make it clear that for vapour-deposited solar cells, the substrate the perovskite is grown upon is very important in preventing amorphous perovskite at the interface, as this will cause *J-V* hysteresis. Further investigations to elucidate the role of the substrate would involve depositing ultra-thin films (<10nm). For example, wettability on different substrates or the influence of lattice mismatch between the perovskite and the interface material may change the crystallisation mechanism. Such an investigation will be very important to identify which surfaces induce crystalline perovskite. Identification of the reason fullerenes create an ideal surface for crystallisation of perovskite is essential to aid in designing an alternative, more photostable, material than fullerenes.

Examination of vapour-deposited $MAPbI_3$ devices with the sensitive technique of Fourier transform photocurrent spectroscopy has shown the effects of low temperature on device photocurrent spectra. The temperature dependence of J_{sc} and V_{oc} show that below 200 K these parameters drop significantly.

Interestingly, the photocurrent spectra at low temperatures (below 150 K) showed a PbI_2 photocurrent onset. The presence of PbI_2 photocurrent shows that PbI_2 plays an active role in generating photocurrent and that it exists in the film most likely as a crystalline semiconductor with a percolation pathway from one transport layer to another. Moreover, the photocurrent spectrum at 15 K was considerably blue shifted with respect to the absorption spectrum at the same temperature. The shift in the spectra allowed the estimation of the exciton binding energy of 9.1 meV. Further investigations could implement inorganic transport layers and investigate the device *J-V* characteristics at low temperature to establish whether a high photocurrent can be extracted at lower temperatures.

The investigation has proven that vapour deposition is a powerful fabrication technique that can be utilised to understand, in detail, the formation dynamics of hybrid metal-halide perovskites and elucidate the implications of the substrate material on the final quality of hybrid metal-halide perovskite thin films. Overall, vapour deposition shows excellent promise to be the dominant technique to fabricate hybrid metal-halide perovskite thin film for photovoltaic applications in industry.

Chapter 9

References

(1) Gueymard, C. A. The Sun's Total and Spectral Irradiance for Solar Energy Applications and Solar Radiation Models. *Sol. Energy* **2004**, *76* (4), 423–453.

(2) Bloomberg New Energy Finance. *The Sustainable Energy in America 2017 Factbook*; 2017.

(3) Ran, F.; Feldman, D.; Margolis, R.; Woodhouse, M.; Ardani, K.; National Center for Photovoltaics. *U.S. Solar Photovoltaic System Cost Benchmark: Q1 2017*; 2017.

(4) REN21. *Renewables 2018 Global Status Report*; 2018.

(5) International Renewable Energy Agency. *Renewable Power Generation Costs in 2014*; 2015.

(6) Bhandari, K. P.; Collier, J. M.; Ellingson, R. J.; Apul, D. S. Energy Payback Time (EPBT) and Energy Return on Energy Invested (EROI) of Solar Photovoltaic Systems: A Systematic Review and Meta-Analysis. *Renew. Sustain. Energy Rev.* **2015**, *47*, 133–141.

(7) (Mariska) de Wild-Scholten, M. J. Energy Payback Time and Carbon Footprint of Commercial Photovoltaic Systems. *Sol. Energy Mater. Sol. Cells* **2013**, *119*, 296–305.

(8) International Renewable Energy Agency. Solar PV Costs 2010-2015 http://resourceirena.irena.org (accessed Aug 16, 2018).

(9) Kojima, A.; Teshima, K.; Shirai, Y.; Miyasaka, T. Organometal Halide Perovskites as Visible-Light Sensitizers for Photovoltaic Cells. *J. Am. Chem. Soc.* **2009**, *131* (17), 6050–6051.

(10) Lee, M. M.; Teuscher, J.; Miyasaka, T.; Murakami, T. N.; Snaith, H. J. Efficient Hybrid Solar Cells Based on Meso-Superstructured Organometal Halide Perovskites. *Science (80-.).* **2012**, *338* (6107), 643–647.

(11) Burschka, J.; Pellet, N.; Moon, S.-J.; Humphry-Baker, R.; Gao, P.; Nazeeruddin, M. K.; Grätzel, M. Sequential Deposition as a Route to High-Performance Perovskite-Sensitized Solar Cells. *Nature* **2013**, *499* (7458), 316–319.

(12) Ball, J. M.; Lee, M. M.; Hey, A.; Snaith, H. J. Low-Temperature Processed Meso-Superstructured to Thin-Film Perovskite Solar Cells. *Energy Environ. Sci.* **2013**, *6* (6), 1739.

(13) Mattox, D. M. *Handbook of Physical Vapor Deposition (PVD) Processing*; William Andrew, 2010.

(14) Liu, M.; Johnston, M. B.; Snaith, H. J. Efficient Planar Heterojunction Perovskite Solar Cells by Vapour Deposition. *Nature* **2013**, *501* (7467), 395–398.

(15) Momblona, C.; Gil-Escrig, L.; Bandiello, E.; Hutter, E. M.; Sessolo, M.; Lederer, K.; Blochwitz-Nimoth, J.; Bolink, H. J. Efficient Vacuum Deposited P-i-n and n-i-p Perovskite Solar Cells Employing Doped Charge Transport Layers. *Energy Environ. Sci.* **2016**, *9* (11), 3456–3463.

(16) Sahli, F.; Werner, J.; Kamino, B. A.; Bräuninger, M.; Monnard, R.; Paviet-Salomon, B.; Barraud, L.; Ding, L.; Diaz Leon, J. J.; Sacchetto, D.; et al. Fully Textured Monolithic Perovskite/Silicon Tandem Solar Cells with 25.2% Power Conversion

Efficiency. *Nat. Mater.* **2018**.
(17) https://www.nrel.gov/pv/. NREL Efficiency Chart-July 2018.
(18) Atkins, P. W.; De Paula, J. *Elements of Physical Chemistry*, 7th ed.; Oxford University Press: Oxford, 2017.
(19) Atkins, P.; de Paula, J. *Atkins' Physical Chemistry*, 9th editio.; OUP Oxford: Oxford, 2009.
(20) Banwell, C. N.; McCash, E. M. *Fundamentals of Molecular Spectroscopy*, 4th rev.; McGraw-Hill: Maidenhead, 1994.
(21) Griffiths, P. R.; De Haseth, J. A.; Winefordner, J. D. *Fourier Transform Infrared Spectrometry*, 2nd ed.; Chemical Analysis: A Series of Monographs on Analytical Chemistry and Its Applications; Wiley: Hobeken, 2007.
(22) Morales, C. M.; Thompson, W. H. Molecular-Level Mechanisms of Vibrational Frequency Shifts in a Polar Liquid. *J. Phys. Chem. B* **2011**, *115* (23), 7597–7605.
(23) Badger, R. M.; Bauer, S. H. Spectroscopic Studies of the Hydrogen Bond. II. The Shift of the O–H Vibrational Frequency in the Formation of the Hydrogen Bond. *J. Chem. Phys.* **1937**, *5* (11), 839–851.
(24) Smart, L. E.; Moore, E. A. *Solid State Chemistry: An Introduction, Third Edition*, Third.; Taylor & Francis: Boca raton, 2005.
(25) Cox, P. A. *The Electronic Structure And Chemistry Of Solids*, First.; Oxford University Press: New York, 1987.
(26) Nelson, J. *The Physics of Solar Cells*; Imperial College Press, 2003.
(27) Varshni, Y. P. Temperature Dependence of the Energy Gap in Semiconductors. *Physica* **1967**, *34* (1), 149–154.
(28) Löper, P.; Pysch, D.; Richter, A.; Hermle, M.; Janz, S.; Zacharias, M.; Glunz, S. W. Analysis of the Temperature Dependence of the Open-Circuit Voltage. *Energy Procedia* **2012**, *27*, 135–142.
(29) Garcia-Belmonte, G. Temperature Dependence of Open-Circuit Voltage in Organic Solar Cells from Generation–recombination Kinetic Balance. *Sol. Energy Mater. Sol. Cells* **2010**, *94* (12), 2166–2169.
(30) Gao, F.; Tress, W.; Wang, J.; Inganäs, O. Temperature Dependence of Charge Carrier Generation in Organic Photovoltaics. *Phys. Rev. Lett.* **2015**, *114* (12), 128701.
(31) Urbach, F. The Long-Wavelength Edge of Photographic Sensitivity and of the Electronic Absorption of Solids. *Phys. Rev.* **1953**, *92* (5), 1324–1324.
(32) Kurik, M. V. Urbach Rule. *Phys. Status Solidi* **1971**, *8* (1), 9–45.
(33) Cody, G. D. Urbach Edge of Crystalline and Amorphous Silicon: A Personal Review. *J. Non. Cryst. Solids* **1992**, *141* (C), 3–15.
(34) Thomas, D. G.; Hopfield, J. J.; Power, M. Excitons and the Absorption Edge of Cadmium Sulfide. *Phys. Rev.* **1960**, *119* (2), 570–574.
(35) Mahan, G. D. Phonon-Broadened Optical Spectra: Urbach's Rule. *Phys. Rev.* **1966**, *145* (2), 602–608.
(36) Dunn, D. Urbach's Rule in an Electron-Phonon Model. *Phys. Rev.* **1968**, *174* (3), 855–858.
(37) Grein, C. H.; John, S. Temperature Dependence of the Urbach Optical Absorption Edge: A Theory of Multiple Phonon Absorption and Emission Sidebands. *Phys. Rev. B* **1989**, *39* (2), 1140–1151.
(38) Johnson, S. R.; Tiedje, T. Temperature Dependence of the Urbach Edge in GaAs. *J. Appl. Phys.* **1995**, *78* (9), 5609–5613.
(39) Antonioli, G.; Bianchi, D.; Franzosi, P. Intrinsic Urbach Rule and Electron—Phonon Interaction in GaAs and Related III-V Compounds. *Phys. status solidi* **1981**, *106* (1), 79–84.
(40) Gokmen, T.; Gunawan, O.; Todorov, T. K.; Mitzi, D. B. Band Tailing and Efficiency

Limitation in Kesterite Solar Cells. *Appl. Phys. Lett.* **2013**, *103* (10), 103506.
(41) Studenyak, I.; Kranj, M.; Kurik, M. Urbach Rule in Solid State Physics. *Int. J. Opt. Appl.* **2014**, *4* (3), 76–83.
(42) Cody, G. D.; Tiedje, T.; Abeles, B.; Brooks, B.; Goldstein, Y. Disorder and the Optical-Absorption Edge of Hydrogenated Amorphous Silicon. *Phys. Rev. Lett.* **1981**, *47* (20), 1480–1483.
(43) Cody, G. D. Chapter 2 The Optical Absorption Edge of A-Si: H. *Semicond. Semimetals* **1984**, *21*, 11–82.
(44) Martienssen, W. Über Die Excitonenbanden Der Alkalihalogenidkristalle. *J. Phys. Chem. Solids* **1957**, *2* (4), 257–267.
(45) Kranjčec, M.; Studenyak, I. P.; Kurik, M. V. On the Urbach Rule in Non-Crystalline Solids. *J. Non. Cryst. Solids* **2009**, *355* (1), 54–57.
(46) Skumanich, A.; Frova, A.; Amer, N. M. Urbach Tail and Gap States in Hydrogenated A-SiC and a-SiGe Alloys. *Solid State Commun.* **1985**, *54* (7), 597–601.
(47) Studenyak, I. P.; Kranjčec, M.; Bilanchuk, V. V.; Kokhan, O. P.; Orliukas, A. F.; Kezionis, A.; Kazakevicius, E.; Salkus, T. Temperature and Compositional Behaviour of Electrical Conductivity and Optical Absorption Edge in Cu7Ge(S1−xSex)5I Mixed Superionic Crystals. *Solid State Ionics* **2010**, *181* (35–36), 1596–1600.
(48) Zametin, V. I. Absorption Edge Anomalies in Polar Semiconductors and Dielectrics at Phase Transitions. *Phys. status solidi* **1984**, *124* (2), 625–640.
(49) Zakis, Y. R.; Moskalionov, A. V. No Title. *Uchenie Zap. Latv. Gos. Univi* **1975**, *231* (61).
(50) Godmanis, I. T.; Trukhin, A. N.; Hübner, K. Exciton–phonon Interaction in Crystalline and Vitreous SiO2. *Phys. status solidi* **1983**, *116* (1), 279–287.
(51) Kranjčec, M.; Studenyak, I. P.; Kurik, M. V. On the Urbach Rule in Non-Crystalline Solids. *J. Non. Cryst. Solids* **2009**, *355* (1), 54–57.
(52) Weber, D. $CH_3NH_3PbX_3$, Ein Pb(II)-System Mit Kubischer Perowskitstruktur / $CH_3NH_3PbX_3$, a Pb(II)-System with Cubic Perovskite Structure. *Zeitschrift für Naturforsch. B* **1978**, *33* (12), 1443–1445.
(53) Yamada, K.; Hayashi, T.; Umehara, T.; Okuda, T.; Ichiba, S. 81 Br NQR and 119 Sn Mössbauer Spectra for SnBr 3 − Anions. *Bull. Chem. Soc. Jpn.* **1987**, *60* (12), 4203–4207.
(54) Yamada, K.; Nose, S.; Umehara, T.; Okuda, T.; Ichiba, S. 81 Br NQR and 119 Sn Mössbauer Study for $MSnBr_3$ (M=Cs and CH_3NH_3). *Bull. Chem. Soc. Jpn.* **1988**, *61* (12), 4265–4268.
(55) Yamada, K.; Matsui, T.; Tsuritani, T.; Okuda, T.; Ichiba, S. 127I-NQR, 119 Sn Mössbauer Effect, and Electrical Conductivity of $MSnI_3$ (M = K, NH_4 , Rb, Cs, and CH_3NH_3). *Zeitschrift für Naturforsch. A* **1990**, *45* (3–4).
(56) Mitzi, D. B. Synthesis, Crystal Structure, and Optical and Thermal Properties of $(C_4H_9NH_3)_2MI_4$ (M = Ge, Sn, Pb). *Chem. Mater.* **1996**, *8* (3), 791–800.
(57) Mitzi, D. B.; Wang, S.; Feild, C. A.; Chess, C. A.; Guloy, A. M. Conducting Layered Organic-Inorganic Halides Containing <110>-Oriented Perovskite Sheets. *Science (80-.).* **1995**, *267* (5203), 1473–1476.
(58) Mitzi, D. B.; Feild, C. A.; Harrison, W. T. A.; Guloy, A. M. Conducting Tin Halides with a Layered Organic-Based Perovskite Structure. *Nature* **1994**, *369* (6480), 467–469.
(59) Mitzi, D. B.; Feild, C. A.; Schlesinger, Z.; Laibowitz, R. B. Transport, Optical, and Magnetic Properties of the Conducting Halide Perovskite $CH_3NH_3SnI_3$. *J. Solid State Chem.* **1995**, *114* (1), 159–163.
(60) Kagan, C. R.; Mitzi, D. B.; Dimitrakopoulos, C. D. Organic-Inorganic Hybrid

Materials as Semiconducting Channels in Thin-Film Field-Effect Transistors. *Science (80-.).* **1999**, *286* (5441), 945–947.

(61) Heo, J. H.; Im, S. H.; Noh, J. H.; Mandal, T. N.; Lim, C.-S.; Chang, J. A.; Lee, Y. H.; Kim, H.; Sarkar, A.; Nazeeruddin, M. K.; et al. Efficient Inorganic–organic Hybrid Heterojunction Solar Cells Containing Perovskite Compound and Polymeric Hole Conductors. *Nat. Photonics* **2013**, *7* (6), 486–491.

(62) Wehrenfennig, C.; Eperon, G. E.; Johnston, M. B.; Snaith, H. J.; Herz, L. M. High Charge Carrier Mobilities and Lifetimes in Organolead Trihalide Perovskites. *Adv. Mater.* **2014**, *26* (10), 1584–1589.

(63) Stranks, S. D.; Eperon, G. E.; Grancini, G.; Menelaou, C.; Alcocer, M. J. P.; Leijtens, T.; Herz, L. M.; Petrozza, A.; Snaith, H. J. Electron-Hole Diffusion Lengths Exceeding 1 Micrometer in an Organometal Trihalide Perovskite Absorber. *Science (80-.).* **2013**, *342* (6156).

(64) Johnston, M. B.; Herz, L. M. Hybrid Perovskites for Photovoltaics: Charge-Carrier Recombination, Diffusion, and Radiative Efficiencies. *Acc. Chem. Res.* **2016**, *49* (1), 146–154.

(65) Herz, L. M. Charge-Carrier Mobilities in Metal Halide Perovskites: Fundamental Mechanisms and Limits. *ACS Energy Lett.* **2017**, *2* (7), 1539–1548.

(66) Herz, L. M. Charge-Carrier Dynamics in Organic-Inorganic Metal Halide Perovskites. *Annu. Rev. Phys. Chem.* **2016**, *67* (1), 65–89.

(67) Manser, J. S.; Christians, J. A.; Kamat, P. V. Intriguing Optoelectronic Properties of Metal Halide Perovskites. *Chem. Rev.* **2016**, *116* (21), 12956–13008.

(68) Wehrenfennig, C.; Liu, M.; Snaith, H. J.; Johnston, M. B.; Herz, L. M. Charge-Carrier Dynamics in Vapour-Deposited Films of the Organolead Halide Perovskite $CH_3NH_3PbI_{3-x}Cl_x$. *Energy Environ. Sci.* **2014**, *7* (7), 2269.

(69) Ng, A.; Ren, Z.; Shen, Q.; Cheung, S. H.; Gokkaya, H. C.; Bai, G.; Wang, J.; Yang, L.; So, S. K.; Djurišić, A. B.; et al. Efficiency Enhancement by Defect Engineering in Perovskite Photovoltaic Cells Prepared Using Evaporated PbI_2 /CH_3NH_3I Multilayers. *J. Mater. Chem. A* **2015**, *3* (17), 9223–9231.

(70) Jung, M.-C.; Raga, S. R.; Qi, Y. Properties and Solar Cell Applications of Pb-Free Perovskite Films Formed by Vapor Deposition. *RSC Adv.* **2016**, *6* (4), 2819–2825.

(71) Lin, Q.; Armin, A.; Nagiri, R. C. R.; Burn, P. L.; Meredith, P. Electro-Optics of Perovskite Solar Cells. *Nat. Photonics* **2014**, *9* (2), 106–112.

(72) Malinkiewicz, O.; Yella, A.; Lee, Y. H.; Espallargas, G. M.; Graetzel, M.; Nazeeruddin, M. K.; Bolink, H. J. Perovskite Solar Cells Employing Organic Charge-Transport Layers. *Nat. Photonics* **2013**, *8* (2), 128–132.

(73) Wang, S.; Ono, L. K.; Leyden, M. R.; Kato, Y.; Raga, S. R.; Lee, M. V.; Qi, Y. Smooth Perovskite Thin Films and Efficient Perovskite Solar Cells Prepared by the Hybrid Deposition Method. *J. Mater. Chem. A* **2015**, *3* (28), 14631–14641.

(74) Li, Y.; Xu, X.; Wang, C.; Wang, C.; Xie, F.; Yang, J.; Gao, Y. Investigation on Thermal Evaporated $CH_3NH_3PbI_3$ Thin Films. *AIP Adv.* **2015**, *5* (9), 097111.

(75) Gil-Escrig, L.; Miquel Sempere, A.; Sessolo, M.; Bolink, H. J. Mixed Iodide-Bromide Methylammonium Lead Perovskite Based Diodes for Light-Emission and Photovoltaics. *J. Phys. Chem. Lett.* **2015**, 150902174604003.

(76) Zhao, D.; Ke, W.; Grice, C. R.; Cimaroli, A. J.; Tan, X.; Yang, M.; Collins, R. W.; Zhang, H.; Zhu, K.; Yan, Y. Annealing-Free Efficient Vacuum-Deposited Planar Perovskite Solar Cells with Evaporated Fullerenes as Electron-Selective Layers. *Nano Energy* **2015**.

(77) Fan, P.; Gu, D.; Liang, G.; Chen, J.; Luo, J.; Xie, Y.; Zheng, Z.; Zhang, D. Growth of High Quality $CH_3NH_3PbI_3$ Thin Films Prepared by Modified Dual-Source Vapor Evaporation. *J. Mater. Sci. Mater. Electron.* **2015**.

(78) Su, Z.; Hou, F.; Jin, F.; Wang, L.; Li, Y.; Zhu, J.; Chu, B.; Li, W. Hole Transporting Material-Free and Annealing-Free Thermal Evaporated Planar Perovskite Solar Cells with an Ultra-Thin $CH_3NH_3PbI_{3-X}Cl_X$ Layer. *Org. Electron.* **2015**, *26*, 104–108.

(79) Teuscher, J.; Ulianov, A.; Müntener, O.; Grätzel, M.; Tétreault, N. Control and Study of the Stoichiometry in Evaporated Perovskite Solar Cells. *ChemSusChem* **2015**, *8* (22), 3847–3852.

(80) Gil-Escrig, L.; Miquel Sempere, A.; Sessolo, M.; Bolink, H. J. Mixed Iodide-Bromide Methylammonium Lead Perovskite Based Diodes for Light-Emission and Photovoltaics. *J. Phys. Chem. Lett.* **2015**, *6* (18), 150902174604003.

(81) Borchert, J.; Boht, H.; Fränzel, W.; Csuk, R.; Scheer, R.; Pistor, P. Structural Investigation of Co-Evaporated Methyl Ammonium Lead Halide Perovskite Films during Growth and Thermal Decomposition Using Different PbX2 (X=I,Cl) Precursors. *J. Mater. Chem. A* **2015**.

(82) Gao, C.; Liu, J.; Liao, C.; Ye, Q.; Zhang, Y.; He, X.; Guo, X.; Mei, J.; Lau, W. Formation of Organic–inorganic Mixed Halide Perovskite Films by Thermal Evaporation of $PbCl_2$ and CH_3NH_3I Compounds. *RSC Adv.* **2015**, *5* (33), 26175–26180.

(83) Yang, D.; Yang, Z.; Qin, W.; Zhang, Y.; Liu, S. F.; Li, C. Alternating Precursor Layer Deposition for Highly Stable Perovskite Films towards Efficient Solar Cells Using Vacuum Deposition. *J. Mater. Chem. A* **2015**, *3* (18), 9401–9405.

(84) Chen, C.; Kang, H.; Hsiao, S.; Yang, P.; Chiang, K.; Lin, H. Effi Cient and Uniform Planar-Type Perovskite Solar Cells by Simple Sequential Vacuum Deposition. *Adv. Mater.* **2014**, *26* (38), 6647–6652.

(85) Kim, B.-S.; Kim, T.-M.; Choi, M.-S.; Shim, H.-S.; Kim, J.-J. Fully Vacuum–processed Perovskite Solar Cells with High Open Circuit Voltage Using MoO3/NPB as Hole Extraction Layers. *Org. Electron.* **2015**, *17*, 102–106.

(86) Wehrenfennig, C.; Liu, M.; Snaith, H. J.; Johnston, M. B.; Herz, L. M. Charge-Carrier Dynamics in Vapour-Deposited Films of the Organolead Halide Perovskite $CH_3NH_3PbI_{3-x}Cl_x$. *Energy Environ. Sci.* **2014**, *7* (7), 2269.

(87) Yoon, W.; Boercker, J. E.; Lumb, M. P.; Tischler, J. G.; Jenkins, P. P.; Walters, R. J. Vapor Deposition of Organic-Inorganic Hybrid Perovskite Thin-Films for Photovoltaic Applications. In *2014 IEEE 40th Photovoltaic Specialist Conference (PVSC)*; IEEE, 2014; pp 1577–1580.

(88) Patel, J. B.; Lin, Q.; Zadvorna, O.; Davies, C. L.; Herz, L. M.; Johnston, M. B. Photocurrent Spectroscopy of Perovskite Solar Cells Over a Wide Temperature Range from 15 to 350 K. *J. Phys. Chem. Lett.* **2018**, *9* (1), 263–268.

(89) Patel, J. B.; Milot, R. L.; Wright, A. D.; Herz, L. M.; Johnston, M. B. Formation Dynamics of $CH_3NH_3PbI_3$ Perovskite Following Two-Step Layer Deposition. *J. Phys. Chem. Lett.* **2016**, *7* (1), 96–102.

(90) Patel, J. B.; Wong-Leung, J.; Van Reenen, S.; Sakai, N.; Wang, J. T. W.; Parrott, E. S.; Liu, M.; Snaith, H. J.; Herz, L. M.; Johnston, M. B. Influence of Interface Morphology on Hysteresis in Vapor-Deposited Perovskite Solar Cells. *Adv. Electron. Mater.* **2017**, *3* (2), 1600470.

(91) Liu, M.; Johnston, M. B.; Snaith, H. J. Efficient Planar Heterojunction Perovskite Solar Cells by Vapour Deposition. *Nature* **2013**, *501* (7467), 395–398.

(92) Eperon, G. E.; Habisreutinger, S. N.; Leijtens, T.; Bruijnaers, B. J.; van Franeker, J. J.; deQuilettes, D. W.; Pathak, S.; Sutton, R. J.; Grancini, G.; Ginger, D. S.; et al. The Importance of Moisture in Hybrid Lead Halide Perovskite Thin Film Fabrication. *ACS Nano* **2015**, *9* (9), 9380–9393.

(93) Schulz, P.; Edri, E.; Kirmayer, S.; Hodes, G.; Cahen, D.; Kahn, A. Interface Energetics in Organo-Metal Halide Perovskite-Based Photovoltaic Cells. *Energy*

Environ. Sci. **2014**, *7* (4), 1377.
(94) Snaith, H. J.; Abate, A.; Ball, J. M.; Eperon, G. E.; Leijtens, T.; Noel, N. K.; Stranks, S. D.; Wang, J. T.-W.; Wojciechowski, K.; Zhang, W. Anomalous Hysteresis in Perovskite Solar Cells. *J. Phys. Chem. Lett.* **2014**, *5* (9), 1511–1515.
(95) van Reenen, S.; Kemerink, M.; Snaith, H. J. Modeling Anomalous Hysteresis in Perovskite Solar Cells. *J. Phys. Chem. Lett.* **2015**, *6* (19), 3808–3814.
(96) Calado, P.; Telford, A. M.; Bryant, D.; Li, X.; Nelson, J.; O'Regan, B. C.; Barnes, P. R. F. Evidence for Ion Migration in Hybrid Perovskite Solar Cells with Minimal Hysteresis. *Nat. Commun.* **2016**, *7*, 13831.
(97) Azpiroz, J. M.; Mosconi, E.; Bisquert, J.; De Angelis, F. Defect Migration in Methylammonium Lead Iodide and Its Role in Perovskite Solar Cell Operation. *Energy Environ. Sci.* **2015**, *8* (7), 2118–2127.
(98) Haruyama, J.; Sodeyama, K.; Han, L.; Tateyama, Y. First-Principles Study of Ion Diffusion in Perovskite Solar Cell Sensitizers. *J. Am. Chem. Soc.* **2015**, *137* (32), 10048–10051.
(99) Eames, C.; Frost, J. M.; Barnes, P. R. F.; O'Regan, B. C.; Walsh, A.; Islam, M. S. Ionic Transport in Hybrid Lead Iodide Perovskite Solar Cells. *Nat. Commun.* **2015**, *6* (1), 7497.
(100) Walsh, A.; Stranks, S. D. Taking Control of Ion Transport in Halide Perovskite Solar Cells. *ACS Energy Lett.* **2018**, 1983–1990.
(101) Li, C.; Tscheuschner, S.; Paulus, F.; Hopkinson, P. E.; Kießling, J.; Köhler, A.; Vaynzof, Y.; Huettner, S. Iodine Migration and Its Effect on Hysteresis in Perovskite Solar Cells.
(102) Stranks, S. D.; Wood, S. M.; Wojciechowski, K.; Deschler, F.; Saliba, M.; Khandelwal, H.; Patel, J. B.; Elston, S. J.; Herz, L. M.; Johnston, M. B.; et al. Enhanced Amplified Spontaneous Emission in Perovskites Using a Flexible Cholesteric Liquid Crystal Reflector. *Nano Lett.* **2015**, *15* (8), 4935–4941.
(103) Milot, R. L.; Eperon, G. E.; Snaith, H. J.; Johnston, M. B.; Herz, L. M. Temperature-Dependent Charge-Carrier Dynamics in $CH_3NH_3PbI_3$ Perovskite Thin Films. *Adv. Funct. Mater.* **2015**, *25* (39), 6218–6227.
(104) Pisacane, V. L. *Fundamentals of Space Systems*; Oxford University Press, 2005.
(105) Wojciechowski, K.; Leijtens, T.; Siprova, S.; Schlueter, C.; Hörantner, M. T.; Wang, J. T.-W.; Li, C.-Z.; Jen, A. K.-Y.; Lee, T.-L.; Snaith, H. J. C_{60} as an Efficient N-Type Compact Layer in Perovskite Solar Cells. *J. Phys. Chem. Lett.* **2015**, *6* (12), 2399–2405.
(106) Wojciechowski, K.; Stranks, S. D.; Abate, A.; Sadoughi, G.; Sadhanala, A.; Kopidakis, N.; Rumbles, G.; Li, C.-Z.; Friend, R. H.; Jen, A. K.-Y.; et al. Heterojunction Modification for Highly Efficient Organic–Inorganic Perovskite Solar Cells. *ACS Nano* **2014**, *8* (12), 12701–12709.
(107) Xu, J.; Buin, A.; Ip, A. H.; Li, W.; Voznyy, O.; Comin, R.; Yuan, M.; Jeon, S.; Ning, Z.; McDowell, J. J.; et al. Perovskite–fullerene Hybrid Materials Suppress Hysteresis in Planar Diodes. *Nat. Commun.* **2015**, *6*, 7081.
(108) Jeng, J. Y.; Chiang, Y. F.; Lee, M. H.; Peng, S. R.; Guo, T. F.; Chen, P.; Wen, T. C. $CH_3NH_3PbI_3$ Perovskite/Fullerene Planar-Heterojunction Hybrid Solar Cells. *Adv. Mater.* **2013**, *25* (27), 3727–3732.
(109) Xu, J.; Buin, A.; Ip, A. H.; Li, W.; Voznyy, O.; Comin, R.; Yuan, M.; Jeon, S.; Ning, Z.; McDowell, J. J.; et al. Perovskite–fullerene Hybrid Materials Suppress Hysteresis in Planar Diodes. *Nat. Commun.* **2015**, *6*, 7081.
(110) Tang, C. W. Multilayer Organic Photovoltaic Elements. US Patent 4,164,431. 05/907361, May 18, 1979.
(111) Tang, C. W. Two-Layer Organic Photovoltaic Cell. *Appl. Phys. Lett.* **1986**, *48* (2),

183–185.
(112) Kippelen, B.; Brédas, J.-L. Organic Photovoltaics. *Energy Environ. Sci.* **2009**, *2* (3), 251.
(113) Yoo, S.; Domercq, B.; Kippelen, B. Efficient Thin-Film Organic Solar Cells Based on Pentacene/C_{60} Heterojunctions. *Appl. Phys. Lett.* **2004**, *85* (22), 5427–5429.
(114) Hiramoto, M.; Fujiwara, H.; Yokoyama, M. Three-Layered Organic Solar Cell with a Photoactive Interlayer of Codeposited Pigments. *Appl. Phys. Lett.* **1991**, *58* (10), 1062–1064.
(115) Yu, G.; Gao, J.; Hummelen, J. C.; Wudl, F.; Heeger, A. J. Polymer Photovoltaic Cells: Enhanced Efficiencies via a Network of Internal Donor-Acceptor Heterojunctions. *Science (80-.).* **1995**, *270* (5243), 1789–1791.
(116) Halls, J. J. M.; Walsh, C. A.; Greenham, N. C.; Marseglia, E. A.; Friend, R. H.; Moratti, S. C.; Holmes, A. B. Efficient Photodiodes from Interpenetrating Polymer Networks. *Nature* **1995**, *376* (6540), 498–500.
(117) Sariciftci, N. S.; Smilowitz, L.; Heeger, a J.; Wudl, F. Photoinduced Electron Transfer from a Conducting Polymer to Buckminsterfullerene. *Science* **1992**, *258* (5087), 1474–1476.
(118) Nelson, J. Organic Photovoltaic Films. *Curr. Opin. Solid State Mater. Sci.* **2002**, *6* (1), 87–95.
(119) Liu, X.; Zhang, C.; Duan, C.; Li, M.; Hu, Z.; Wang, J.; Liu, F.; Li, N.; Brabec, C. J.; Janssen, R. A. J.; et al. Morphology Optimization via Side Chain Engineering Enables All-Polymer Solar Cells with Excellent Fill Factor and Stability. *J. Am. Chem. Soc.* **2018**, *140* (28), 8934–8943.
(120) Zhao, W.; Li, S.; Yao, H.; Zhang, S.; Zhang, Y.; Yang, B.; Hou, J. Molecular Optimization Enables over 13% Efficiency in Organic Solar Cells. *J. Am. Chem. Soc.* **2017**, *139* (21), 7148–7151.
(121) Berny, S.; Blouin, N.; Distler, A.; Egelhaaf, H.-J.; Krompiec, M.; Lohr, A.; Lozman, O. R.; Morse, G. E.; Nanson, L.; Pron, A.; et al. Solar Trees: First Large-Scale Demonstration of Fully Solution Coated, Semitransparent, Flexible Organic Photovoltaic Modules. *Adv. Sci.* **2016**, *3* (5), 1500342.
(122) Köhler, A.; Bässler, H. *Electronic Processes in Organic Semiconductors: An Introduction*; Wiley, 2015.
(123) Sakai, N.; Pathak, S.; Chen, H.-W.; Haghighirad, A. A.; Stranks, S. D.; Miyasaka, T.; Snaith, H. J. The Mechanism of Toluene-Assisted Crystallization of Organic–inorganic Perovskites for Highly Efficient Solar Cells. *J. Mater. Chem. A* **2016**, *4* (12), 4464–4471.
(124) Wang, J. T.-W.; Wang, Z.; Pathak, S.; Zhang, W.; DeQuilettes, D. W.; Wisnivesky-Rocca-Rivarola, F.; Huang, J.; Nayak, P. K.; Patel, J. B.; Mohd Yusof, H. A.; et al. Efficient Perovskite Solar Cells by Metal Ion Doping. *Energy Environ. Sci.* **2016**, *9* (9), 2892–2901.
(125) NREL. NREL National Center for Photovoltaics http://www.nrel.gov/ncpv/ (accessed Jun 19, 2016).
(126) Dualeh, A.; Tétreault, N.; Moehl, T.; Gao, P.; Nazeeruddin, M. K.; Grätzel, M. Effect of Annealing Temperature on Film Morphology of Organic-Inorganic Hybrid Pervoskite Solid-State Solar Cells. *Adv. Funct. Mater.* **2014**, *24* (21), 3250–3258.
(127) Lin, Q.; Armin, A.; Nagiri, R. C. R.; Burn, P. L.; Meredith, P. Electro-Optics of Perovskite Solar Cells. *Nat. Photonics* **2014**, *9* (2), 106–112.
(128) You, J.; Yang, Y. (Michael); Hong, Z.; Song, T.-B.; Meng, L.; Liu, Y.; Jiang, C.; Zhou, H.; Chang, W.-H.; Li, G.; et al. Moisture Assisted Perovskite Film Growth for High Performance Solar Cells. *Appl. Phys. Lett.* **2014**, *105* (18), 183902.
(129) Gao, H.; Bao, C.; Li, F.; Yu, T.; Yang, J.; Zhu, W.; Zhou, X.; Fu, G.; Zou, Z.

Nucleation and Crystal Growth of Organic–Inorganic Lead Halide Perovskites under Different Relative Humidity. *ACS Appl. Mater. Interfaces* **2015**, *7* (17), 9110–9117.
(130) Christians, J. a.; Miranda Herrera, P. a.; Kamat, P. V. Transformation of the Excited State and Photovoltaic Efficiency of $CH_3NH_3PbI_3$ Perovskite upon Controlled Exposure to Humidified Air. *J. Am. Chem. Soc.* **2015**, *137* (4), 1530–1538.
(131) Ko, H.-S.; Lee, J.-W.; Park, N.-G. 15.76% Efficiency Perovskite Solar Cells Prepared under High Relative Humidity: Importance of PbI_2 Morphology in Two-Step Deposition of $CH_3NH_3PbI_3$. *J. Mater. Chem. A* **2015**, *3* (16), 8808–8815.
(132) Wu, C.-G.; Chiang, C.-H.; Tseng, Z.-L.; Nazeeruddin, M. K.; Hagfeldt, A.; Grätzel, M. High Efficiency Stable Inverted Perovskite Solar Cells without Current Hysteresis. *Energy Environ. Sci.* **2015**, *8* (9), 2725–2733.
(133) Gong, X.; Li, M.; Shi, X.-B.; Ma, H.; Wang, Z.-K.; Liao, L.-S. Controllable Perovskite Crystallization by Water Additive for High-Performance Solar Cells. *Adv. Funct. Mater.* **2015**, *25* (42), 6671–6678.
(134) Ahn, N.; Son, D.-Y.; Jang, I.-H.; Kang, S. M.; Choi, M.; Park, N.-G. Highly Reproducible Perovskite Solar Cells with Average Efficiency of 18.3% and Best Efficiency of 19.7% Fabricated via Lewis Base Adduct of Lead(II) Iodide. *J. Am. Chem. Soc.* **2015**, *137* (27), 8696–8699.
(135) Milot, R. L.; Eperon, G. E.; Snaith, H. J.; Johnston, M. B.; Herz, L. M. Temperature-Dependent Charge-Carrier Dynamics in $CH_3NH_3PbI_3$ Perovskite Thin Films. *Adv. Funct. Mater.* **2015**, *25* (39), 6218–6227.
(136) Beckmann, P. A. A Review of Polytypism in Lead Iodide. *Cryst. Res. Technol.* **2010**, *45* (5), 455–460.
(137) Pérez-Osorio, M. A.; Milot, R. L.; Filip, M. R.; Patel, J. B.; Herz, L. M.; Johnston, M. B.; Giustino, F. Vibrational Properties of the Organic–Inorganic Halide Perovskite $CH_3NH_3PbI_3$ from Theory and Experiment: Factor Group Analysis, First-Principles Calculations, and Low-Temperature Infrared Spectra. *J. Phys. Chem. C* **2015**, *119* (46), 25703–25718.
(138) Whalley, E. Infrared Spectra of the Methylammonium Halides: Effects of Orientational Disorder about One Axis. *J. Chem. Phys.* **1969**, *51* (9), 4040.
(139) Cabana, A.; Sandorfy, C. The Infrared Spectra of Solid Methylammonium Halides. *Spectrochim. Acta* **1962**, *18* (4), 843–861.
(140) Yang, S.; Zheng, Y. C.; Hou, Y.; Chen, X.; Chen, Y.; Wang, Y.; Zhao, H.; Yang, H. G. Formation Mechanism of Freestanding $CH_3NH_3PbI_3$ Functional Crystals: In Situ Transformation vs Dissolution–Crystallization. *Chem. Mater.* **2014**, *26* (23), 6705–6710.
(141) Mosconi, E.; Quarti, C.; Ivanovska, T.; Ruani, G.; De Angelis, F. Structural and Electronic Properties of Organo-Halide Lead Perovskites: A Combined IR-Spectroscopy and Ab Initio Molecular Dynamics Investigation. *Phys. Chem. Chem. Phys.* **2014**, *16* (30), 16137.
(142) Leguy, A. M. A.; Hu, Y.; Campoy-Quiles, M.; Alonso, M. I.; Weber, O. J.; Azarhoosh, P.; van Schilfgaarde, M.; Weller, M. T.; Bein, T.; Nelson, J.; et al. Reversible Hydration of $CH_3NH_3PbI_3$ in Films, Single Crystals, and Solar Cells. *Chem. Mater.* **2015**, *27* (9), 3397–3407.
(143) Manser, J. S.; Reid, B.; Kamat, P. V. Evolution of Organic–Inorganic Lead Halide Perovskite from Solid-State Iodoplumbate Complexes. *J. Phys. Chem. C* **2015**, *119* (30), 17065–17073.
(144) Vincent, B. R.; Robertson, K. N.; Cameron, T. S.; Knop, O. Alkylammonium Lead Halides. Part 1. Isolated PbI_6 4− Ions in $(CH_3NH_3PbI_3)_4$ PbI_6 •$2H_2O$. *Can. J. Chem.* **1987**, *65* (5), 1042–1046.
(145) Halder, A.; Choudhury, D.; Ghosh, S.; Subbiah, A. S.; Sarkar, S. K. Exploring

Thermochromic Behavior of Hydrated Hybrid Perovskites in Solar Cells. *J. Phys. Chem. Lett.* **2015**, *6* (16), 3180–3184.

(146) Zhou, H.; Chen, Q.; Li, G.; Luo, S.; Song, T. -b.; Duan, H.-S.; Hong, Z.; You, J.; Liu, Y.; Yang, Y. Interface Engineering of Highly Efficient Perovskite Solar Cells. *Science (80-.).* **2014**, *345* (6196), 542–546.

(147) Eperon, G. E.; Habisreutinger, S. N.; Leijtens, T.; Bruijnaers, B. J.; van Franeker, J. J.; DeQuilettes, D. W.; Pathak, S.; Sutton, R. J.; Grancini, G.; Ginger, D. S.; et al. The Importance of Moisture in Hybrid Lead Halide Perovskite Thin Film Fabrication. *ACS Nano* **2015**, *9* (9), 9380–9393.

(148) Imler, G. H.; Li, X.; Xu, B.; Dobereiner, G. E.; Dai, H.-L.; Rao, Y.; Wayland, B. B. Solid State Transformation of the Crystalline Monohydrate $(CH_3NH_3)PbI_3$ (H_2O) to the $(CH_3NH_3)PbI_3$ Perovskite. *Chem. Commun.* **2015**, *51* (56), 11290–11292.

(149) Baikie, T.; Fang, Y.; Kadro, J. M.; Schreyer, M.; Wei, F.; Mhaisalkar, S. G.; Graetzel, M.; White, T. J. Synthesis and Crystal Chemistry of the Hybrid Perovskite $(CH_3NH_3)PbI_3$ for Solid-State Sensitised Solar Cell Applications. *J. Mater. Chem. A* **2013**, *1* (18), 5628.

(150) Zhou, Z.; Wang, Z.; Zhou, Y.; Pang, S.; Wang, D.; Xu, H.; Liu, Z.; Padture, N. P.; Cui, G. Methylamine-Gas-Induced Defect-Healing Behavior of $CH_3NH_3PbI_3$ Thin Films for Perovskite Solar Cells. *Angew. Chemie Int. Ed.* **2015**, *54* (33), 9705–9709.

(151) Zhao, Y.; Zhu, K. Optical Bleaching of Perovskite $(CH_3NH_3)PbI_3$ through Room-Temperature Phase Transformation Induced by Ammonia. *Chem. Commun. (Camb).* **2014**, *50* (13), 1605–1607.

(152) Wakamiya, A.; Endo, M.; Sasamori, T.; Tokitoh, N.; Ogomi, Y.; Hayase, S.; Murata, Y. Reproducible Fabrication of Efficient Perovskite-Based Solar Cells: X-Ray Crystallographic Studies on the Formation of $CH_3NH_3PbI_3$ Layers. *Chem. Lett.* **2014**, *43* (5), 711–713.

(153) Wang, X.; Li, X.; Tang, G.; Zhao, L.; Zhang, W.; Jiu, T.; Fang, J. Improving Efficiency of Planar Hybrid $CH_3NH_3PbI_{3-x}Cl_x$ Perovskite Solar Cells by Isopropanol Solvent Treatment. *Org. Electron.* **2015**, *24*, 205–211.

(154) Pathak, S.; Sepe, A.; Sadhanala, A.; Deschler, F.; Haghighirad, A.; Sakai, N.; Goedel, K. C.; Stranks, S. D.; Noel, N.; Price, M.; et al. Atmospheric Influence upon Crystallization and Electronic Disorder and Its Impact on the Photophysical Properties of Organic–Inorganic Perovskite Solar Cells. *ACS Nano* **2015**, *9* (3), 2311–2320.

(155) Miyadera, T.; Shibata, Y.; Koganezawa, T.; Murakami, T. N.; Sugita, T.; Tanigaki, N.; Chikamatsu, M. Crystallization Dynamics of Organolead Halide Perovskite by Real-Time X-Ray Diffraction. *Nano Lett.* **2015**, *15* (8), 5630–5634.

(156) Bass, K. K.; McAnally, R. E.; Zhou, S.; Djurovich, P. I.; Thompson, M. E.; Melot, B. C. Influence of Moisture on the Preparation, Crystal Structure, and Photophysical Properties of Organohalide Perovskites. *Chem. Commun.* **2014**, *50* (99), 15819–15822.

(157) D'Innocenzo, V.; Grancini, G.; Alcocer, M. J. P.; Kandada, A. R. S.; Stranks, S. D.; Lee, M. M.; Lanzani, G.; Snaith, H. J.; Petrozza, A. Excitons versus Free Charges in Organo-Lead Tri-Halide Perovskites. *Nat. Commun.* **2014**, *5*, 3586.

(158) Snaith, H. J.; Abate, A.; Ball, J. M.; Eperon, G. E.; Leijtens, T.; Noel, N. K.; Stranks, S. D.; Wang, J. T.-W.; Wojciechowski, K.; Zhang, W. Anomalous Hysteresis in Perovskite Solar Cells. *J. Phys. Chem. Lett.* **2014**, *5* (9), 1511–1515.

(159) Zhang, Y.; Liu, M.; Eperon, G. E.; Leijtens, T. C.; McMeekin, D.; Saliba, M.; Zhang, W.; de Bastiani, M.; Petrozza, A.; Herz, L. M.; et al. Charge Selective Contacts, Mobile Ions and Anomalous Hysteresis in Organic–inorganic Perovskite Solar Cells. *Mater. Horiz.* **2015**, *2* (3), 315–322.

(160) Jeon, N. J.; Noh, J. H.; Yang, W. S.; Kim, Y. C.; Ryu, S.; Seo, J.; Seok, S. Il. Compositional Engineering of Perovskite Materials for High-Performance Solar Cells. *Nature* **2015**, *517* (7535), 476–480.

(161) Era, M.; Hattori, T.; Taira, T.; Tsutsui, T. Self-Organized Growth of PbI-Based Layered Perovskite Quantum Well by Dual-Source Vapor Deposition. *Chem. Mater.* **1997**, *9* (1), 8–10.

(162) Pérez-Osorio, M. A.; Milot, R. L.; Filip, M. R.; Patel, J. B.; Herz, L. M.; Johnston, M. B.; Giustino, F. Vibrational Properties of the Organic–Inorganic Halide Perovskite $CH_3NH_3PbI_3$ from Theory and Experiment: Factor Group Analysis, First-Principles Calculations, and Low-Temperature Infrared Spectra. *J. Phys. Chem. C* **2015**, *119* (46), 25703–25718.

(163) Zhang, W.; Eperon, G. E.; Snaith, H. J. Metal Halide Perovskites for Energy Applications. *Nat. Energy* **2016**, *1* (6), 16048.

(164) Wang, J. T.-W.; Wang, Z.; Pathak, S.; Zhang, W.; DeQuilettes, D. W.; Wisnivesky-Rocca-Rivarola, F.; Huang, J.; Nayak, P. K.; Patel, J. B.; Mohd Yusof, H. A.; et al. Efficient Perovskite Solar Cells by Metal Ion Doping. *Energy Environ. Sci.* **2016**, *9* (9), 2892–2901.

(165) Editorial. A Solar Checklist. *Nat. Photonics* **2015**, *9* (11), 703–703.

(166) Kamat, P. V. TiO 2 Nanostructures: Recent Physical Chemistry Advances. *J. Phys. Chem. C* **2012**, *116* (22), 11849–11851.

(167) Lin, Q.; Armin, A.; Nagiri, R. C. R.; Burn, P. L.; Meredith, P. Electro-Optics of Perovskite Solar Cells. *Nat. Photonics* **2014**, *9* (2), 106–112.

(168) Ruoff, R. S.; Tse, D. S.; Malhotra, R.; Lorents, D. C. Solubility of Fullerene (C_{60}) in a Variety of Solvents. *J. Phys. Chem.* **1993**, *97* (13), 3379–3383.

(169) Cojocaru, L.; Uchida, S.; Jayaweera, P. V. V.; Kaneko, S.; Nakazaki, J.; Kubo, T.; Segawa, H. Origin of the Hysteresis in *I-V* Curves for Planar Structure Perovskite Solar Cells Rationalized with a Surface Boundary-Induced Capacitance Model. *Chem. Lett.* **2015**, *44* (12), 1750–1752.

(170) Almora, O.; Zarazua, I.; Mas-Marza, E.; Mora-Sero, I.; Bisquert, J.; Garcia-Belmonte, G. Capacitive Dark Currents, Hysteresis, and Electrode Polarization in Lead Halide Perovskite Solar Cells. *J. Phys. Chem. Lett.* **2015**, *6* (9), 1645–1652.

(171) Tao, C.; Neutzner, S.; Colella, L.; Marras, S.; Srimath Kandada, A. R.; Gandini, M.; Bastiani, M. de; Pace, G.; Manna, L.; Caironi, M.; et al. 17.6% Stabilized Efficiency in Low-Temperature Processed Planar Perovskite Solar Cells. *Energy Environ. Sci.* **2015**, *8* (8), 2365–2370.

(172) Kim, H.-S.; Jang, I.-H.; Ahn, N.; Choi, M.; Guerrero, A.; Bisquert, J.; Park, N.-G. Control of $I-V$ Hysteresis in $CH_3NH_3PbI_3$ Perovskite Solar Cell. *J. Phys. Chem. Lett.* **2015**, *6* (22), 4633–4639.

(173) Rothmann, M. U.; Li, W.; Zhu, Y.; Liu, A.; Ku, Z.; Bach, U.; Etheridge, J.; Cheng, Y.-B. Structural and Chemical Changes to $CH_3NH_3PbI_3$ Induced by Electron and Gallium Ion Beams. *Adv. Mater.* **2018**, *30* (25), 1800629.

(174) Richardson, G.; O'Kane, S. E. J.; Niemann, R. G.; Peltola, T. A.; Foster, J. M.; Cameron, P. J.; Walker, A. B. Can Slow-Moving Ions Explain Hysteresis in the Current–voltage Curves of Perovskite Solar Cells? *Energy Environ. Sci.* **2016**, *9* (4), 1476–1485.

(175) Yuan, Y.; Huang, J. Ion Migration in Organometal Trihalide Perovskite and Its Impact on Photovoltaic Efficiency and Stability. *Acc. Chem. Res.* **2016**, *49* (2), 286–293.

(176) Zhang, H.; Qiao, X.; Shen, Y.; Moehl, T.; Zakeeruddin, S. M.; Grätzel, M.; Wang, M. Photovoltaic Behaviour of Lead Methylammonium Triiodide Perovskite Solar Cells down to 80 K. *J. Mater. Chem. A* **2015**, *3* (22), 11762–11767.

(177) Leong, W. L.; Ooi, Z.-E.; Sabba, D.; Yi, C.; Zakeeruddin, S. M.; Graetzel, M.; Gordon, J. M.; Katz, E. A.; Mathews, N. Identifying Fundamental Limitations in Halide Perovskite Solar Cells. *Adv. Mater.* **2016**, *28* (12), 2439–2445.

(178) Jacobsson, T. J.; Tress, W.; Correa-Baena, J.-P.; Edvinsson, T.; Hagfeldt, A. Room Temperature as a Goldilocks Environment for $CH_3NH_3PbI_3$ Perovskite Solar Cells: The Importance of Temperature on Device Performance. *J. Phys. Chem. C* **2016**, *120* (21), 11382–11393.

(179) Phuong, L. Q.; Nakaike, Y.; Wakamiya, A.; Kanemitsu, Y. Free Excitons and Exciton–Phonon Coupling in $CH_3NH_3PbI_3$ Single Crystals Revealed by Photocurrent and Photoluminescence Measurements at Low Temperatures. *J. Phys. Chem. Lett.* **2016**, *7* (23), 4905–4910.

(180) Wang, M.; Yim, W.-L.; Liao, P.; Shen, Y. Temperature Dependent Characteristics of Perovskite Solar Cells. *ChemistrySelect* **2017**, *2* (16), 4469–4477.

(181) Snaith, H. J.; Schmidt-Mende, L.; Grätzel, M.; Chiesa, M. Light Intensity, Temperature, and Thickness Dependence of the Open-Circuit Voltage in Solid-State Dye-Sensitized Solar Cells. *Phys. Rev. B* **2006**, *74* (4), 045306.

(182) Hörmann, U.; Kraus, J.; Gruber, M.; Schuhmair, C.; Linderl, T.; Grob, S.; Kapfinger, S.; Klein, K.; Stutzman, M.; Krenner, H. J.; et al. Quantification of Energy Losses in Organic Solar Cells from Temperature-Dependent Device Characteristics. *Phys. Rev. B* **2013**, *88* (23), 235307.

(183) Sze; S.M. Physics of Semiconductor Devices (2nd Edition). Wiley-Interscience,New York, NY 1981.

(184) Sumi, H.; Sumi, A. The Urbach-Martienssen Rule Revisited. *J. Phys. Soc. Japan* **1987**, *56* (6), 2211–2220.

(185) Brivio, F.; Frost, J. M.; Skelton, J. M.; Jackson, A. J.; Weber, O. J.; Weller, M. T.; Goñi, A. R.; Leguy, A. M. A.; Barnes, P. R. F.; Walsh, A. Lattice Dynamics and Vibrational Spectra of the Orthorhombic, Tetragonal, and Cubic Phases of Methylammonium Lead Iodide. *Phys. Rev. B* **2015**, *92*.

(186) Wehrenfennig, C.; Liu, M.; Snaith, H. J.; Johnston, M. B.; Herz, L. M. Charge Carrier Recombination Channels in the Low-Temperature Phase of Organic-Inorganic Lead Halide Perovskite Thin Films. *APL Mater.* **2014**, *2* (8), 081513.

(187) Gobinathan, R.; Hariharan, K.; Ramasamy, P. Electronic Absorption Spectra of Lead Iodide. *Krist. und Tech.* **1981**, *16* (12), 1435–1438.

(188) Wright, A. D.; Verdi, C.; Milot, R. L.; Eperon, G. E.; Pérez-Osorio, M. A.; Snaith, H. J.; Giustino, F.; Johnston, M. B.; Herz, L. M. Electron–phonon Coupling in Hybrid Lead Halide Perovskites. *Nat. Commun.* **2016**, *7*.

(189) Coropceanu, V.; Cornil, J.; da Silva Filho, D. A.; Olivier, Y.; Silbey, R.; Brédas, J.-L. Charge Transport in Organic Semiconductors. *Chem. Rev.* **2007**, *107* (4), 926–952.

(190) Pope, M.; Swenberg, C. E. *Electronic Processes in Organic Crystals and Polymers*; Oxford University Press, 1999.

(191) Roldán-Carmona, C.; Gratia, P.; Zimmermann, I.; Grancini, G.; Gao, P.; Graetzel, M.; Nazeeruddin, M. K. High Efficiency Methylammonium Lead Triiodide Perovskite Solar Cells: The Relevance of Non-Stoichiometric Precursors. *Energy Environ. Sci.* **2015**, *8* (12), 3550–3556.

(192) Jiang, Q.; Chu, Z.; Wang, P.; Yang, X.; Liu, H.; Wang, Y.; Yin, Z.; Wu, J.; Zhang, X.; You, J. Planar-Structure Perovskite Solar Cells with Efficiency beyond 21%. *Adv. Mater.* **2017**, 1703852.

(193) Jacobsson, T. J.; Correa-Baena, J.-P.; Halvani Anaraki, E.; Philippe, B.; Stranks, S. D.; Bouduban, M. E. F.; Tress, W.; Schenk, K.; Teuscher, J.; Moser, J.-E.; et al. Unreacted PbI_2 as a Double-Edged Sword for Enhancing the Performance of Perovskite Solar Cells. *J. Am. Chem. Soc.* **2016**, *138* (32), 10331–10343.

(194) Chen, Q.; Zhou, H.; Song, T.-B.; Luo, S.; Hong, Z.; Duan, H.-S.; Dou, L.; Liu, Y.; Yang, Y. Controllable Self-Induced Passivation of Hybrid Lead Iodide Perovskites toward High Performance Solar Cells. *Nano Lett.* **2014**, *14* (7), 4158–4163.

(195) Ahuja, R.; Arwin, H.; Ferreira da Silva, A.; Persson, C.; Osorio-Guillén, J. M.; Souza de Almeida, J.; Moyses Araujo, C.; Veje, E.; Veissid, N.; An, C. Y.; et al. Electronic and Optical Properties of Lead Iodide. *J. Appl. Phys.* **2002**, *92* (12), 7219–7224.

(196) Du, T.; Burgess, C. H.; Kim, J.; Zhang, J.; Durrant, J. R.; McLachlan, M. A. Formation, Location and Beneficial Role of PbI_2 in Lead Halide Perovskite Solar Cells. *Sustain. Energy Fuels* **2017**, *1* (1), 119–126.

(197) Shih, M.-C.; Li, S.-S.; Hsieh, C.-H.; Wang, Y.-C.; Yang, H.-D.; Chiu, Y.-P.; Chang, C.-S.; Chen, C.-W. Spatially Resolved Imaging on Photocarrier Generations and Band Alignments at Perovskite/PbI_2 Heterointerfaces of Perovskite Solar Cells by Light-Modulated Scanning Tunneling Microscopy. *Nano Lett.* **2017**, *17* (2), 1154–1160.

(198) Holovský, J.; De Wolf, S.; Werner, J.; Remeš, Z.; Müller, M.; Neykova, N.; Ledinský, M.; Černá, L.; Hrzina, P.; Löper, P.; et al. Photocurrent Spectroscopy of Perovskite Layers and Solar Cells: A Sensitive Probe of Material Degradation. *J. Phys. Chem. Lett.* **2017**, *8* (4), 838–843.

(199) Miyata, A.; Mitioglu, A.; Plochocka, P.; Portugall, O.; Wang, J. T.-W.; Stranks, S. D.; Snaith, H. J.; Nicholas, R. J. Direct Measurement of the Exciton Binding Energy and Effective Masses for Charge Carriers in Organic–inorganic Tri-Halide Perovskites. *Nat. Phys.* **2015**, *11* (7), 582–587.

(200) D'Innocenzo, V.; Grancini, G.; Alcocer, M. J. P.; Kandada, A. R. S.; Stranks, S. D.; Lee, M. M.; Lanzani, G.; Snaith, H. J.; Petrozza, A. Excitons versus Free Charges in Organo-Lead Tri-Halide Perovskites. *Nat. Commun.* **2014**, *5* (3), 3586.

(201) Saha, M. N. On a Physical Theory of Stellar Spectra. *Proc. R. Soc. A Math. Phys. Eng. Sci.* **1921**, *99* (697), 135–153.

(202) Lin, Q.; Armin, A.; Burn, P. L.; Meredith, P. Filterless Narrowband Visible Photodetectors. *Nat. Photonics* **2015**, *9* (10), 687–694.

(203) Johnston, M. B. Optoelectronics: Colour-Selective Photodiodes. *Nat. Photonics* **2015**, *9* (10), 634–636.

(204) Burkhard, G. F.; Hoke, E. T.; McGehee, M. D. Accounting for Interference, Scattering, and Electrode Absorption to Make Accurate Internal Quantum Efficiency Measurements in Organic and Other Thin Solar Cells. *Adv. Mater.* **2010**, *22* (30), 3293–3297.

(205) Crothers, T. W.; Milot, R. L.; Patel, J. B.; Parrott, E. S.; Schlipf, J.; Müller-Buschbaum, P.; Johnston, M. B.; Herz, L. M. Photon Reabsorption Masks Intrinsic Bimolecular Charge-Carrier Recombination in $CH_3NH_3PbI_3$ Perovskite. *Nano Lett.* **2017**, *17* (9), 5782–5789.

(206) Fang, Y.; Dong, Q.; Shao, Y.; Yuan, Y.; Huang, J. Highly Narrowband Perovskite Single-Crystal Photodetectors Enabled by Surface-Charge Recombination. *Nat. Photonics* **2015**, *9* (10), 679–686.

(207) Kawano, K.; Pacios, R.; Poplavskyy, D.; Nelson, J.; Bradley, D. D. C.; Durrant, J. R. Degradation of Organic Solar Cells Due to Air Exposure. *Sol. Energy Mater. Sol. Cells* **2006**, *90* (20), 3520–3530.

(208) Gevorgyan, S. A.; Madsen, M. V.; Roth, B.; Corazza, M.; Hösel, M.; Søndergaard, R. R.; Jørgensen, M.; Krebs, F. C. Lifetime of Organic Photovoltaics: Status and Predictions. *Adv. Energy Mater.* **2016**, *6* (2), 1501208.

(209) Jørgensen, M.; Norrman, K.; Gevorgyan, S. a.; Tromholt, T.; Andreasen, B.; Krebs, F. C. Stability of Polymer Solar Cells. *Adv. Mater.* **2012**, *24* (5), 580–612.

(210) Mateker, W. R.; McGehee, M. D. Progress in Understanding Degradation

Mechanisms and Improving Stability in Organic Photovoltaics. *Adv. Mater.* **2017**, *29* (10), 1603940.

(211) Peters, C. H.; Sachs-Quintana, I. T.; Mateker, W. R.; Heumueller, T.; Rivnay, J.; Noriega, R.; Beiley, Z. M.; Hoke, E. T.; Salleo, A.; McGehee, M. D. The Mechanism of Burn-in Loss in a High Efficiency Polymer Solar Cell. *Adv. Mater.* **2012**, *24* (5), 663–668.

(212) Huang, Y.; Kramer, E. J.; Heeger, A. J.; Bazan, G. C. Bulk Heterojunction Solar Cells: Morphology and Performance Relationships. *Chem. Rev.* **2014**, *114* (14), 7006–7043.

(213) Wang, N.; Tong, X.; Burlingame, Q.; Yu, J.; Forrest, S. R. Photodegradation of Small-Molecule Organic Photovoltaics. *Sol. Energy Mater. Sol. Cells* **2014**, *125*, 170–175.

(214) Burlingame, Q.; Tong, X.; Hankett, J.; Slootsky, M.; Chen, Z.; Forrest, S. R. Photochemical Origins of Burn-in Degradation in Small Molecular Weight Organic Photovoltaic Cells. *Energy Environ. Sci.* **2015**, *8* (3), 1005–1010.

(215) Heumueller, T.; Mateker, W. R.; Distler, A.; Fritze, U. F.; Cheacharoen, R.; Nguyen, W. H.; Biele, M.; Salvador, M.; von Delius, M.; Egelhaaf, H.-J.; et al. Morphological and Electrical Control of Fullerene Dimerization Determines Organic Photovoltaic Stability. *Energy Environ. Sci.* **2016**, *9* (1), 247–256.

(216) Inasaridze, L. N.; Shames, A. I.; Martynov, I. V.; Li, B.; Mumyatov, A. V.; Susarova, D. K.; Katz, E. A.; Troshin, P. A. Light-Induced Generation of Free Radicals by Fullerene Derivatives: An Important Degradation Pathway in Organic Photovoltaics? *J. Mater. Chem. A* **2017**, *5* (17), 8044–8050.

(217) Perez, M. D.; Borek, C.; Forrest, S. R.; Thompson, M. E. Molecular and Morphological Influences on the Open Circuit Voltages of Organic Photovoltaic Devices. *J. Am. Chem. Soc.* **2009**, *131* (26), 9281–9286.

(218) Chochos, C. L.; Leclerc, N.; Gasparini, N.; Zimmerman, N.; Tatsi, E.; Katsouras, A.; Moschovas, D.; Serpetzoglou, E.; Konidakis, I.; Fall, S.; et al. The Role of Chemical Structure in Indacenodithienothiophene- Alt -Benzothiadiazole Copolymers for High Performance Organic Solar Cells with Improved Photo-Stability through Minimization of Burn-in Loss. *J. Mater. Chem. A* **2017**, *5* (47), 25064–25076.

(219) Kim, T.; Younts, R.; Lee, W.; Lee, S.; Gundogdu, K.; Kim, B. J. Impact of the Photo-Induced Degradation of Electron Acceptors on the Photophysics, Charge Transport and Device Performance of All-Polymer and Fullerene–polymer Solar Cells. *J. Mater. Chem. A* **2017**, *5* (42), 22170–22179.

(220) Alvarado, S.; Seidler, P.; Lidzey, D.; Bradley, D. Direct Determination of the Exciton Binding Energy of Conjugated Polymers Using a Scanning Tunneling Microscope. *Phys. Rev. Lett.* **1998**, *81* (5), 1082–1085.

(221) Brédas, J.-L.; Cornil, J.; Heeger, A. J. The Exciton Binding Energy in Luminescent Conjugated Polymers. *Adv. Mater.* **1996**, *8* (5), 447–452.

(222) Nelson, J. Polymer:Fullerene Bulk Heterojunction Solar Cells. *Mater. Today* **2011**, *14* (10), 462–470.

(223) Brédas, J.-L.; Norton, J. E.; Cornil, J.; Coropceanu, V. Molecular Understanding of Organic Solar Cells: The Challenges. *Acc. Chem. Res.* **2009**, *42* (11), 1691–1699.

(224) Zheng, Z.; Tummala, N. R.; Fu, Y.-T.; Coropceanu, V.; Brédas, J.-L. Charge-Transfer States in Organic Solar Cells: Understanding the Impact of Polarization, Delocalization, and Disorder. *ACS Appl. Mater. Interfaces* **2017**, acsami.7b02193.

(225) Parkinson, P.; Lloyd-Hughes, J.; Johnston, M. B.; Herz, L. M. Efficient Generation of Charges via Below-Gap Photoexcitation of Polymer-Fullerene Blend Films Investigated by Terahertz Spectroscopy. *Phys. Rev. B* **2008**, *78* (11), 115321.

(226) Gong, J. Q.; Parkinson, P.; Kondratuk, D. V.; Gil-Ramírez, G.; Anderson, H. L.; Herz,

L. M. Structure-Directed Exciton Dynamics in Templated Molecular Nanorings. *J. Phys. Chem. C* **2015**, *119* (11), 6414–6420.

(227) Herz, L. .; Silva, C.; Phillips, R. .; Setayesh, S.; Müllen, K. Exciton Migration to Chain Aggregates in Conjugated Polymers: Influence of Side-Chain Substitution. *Chem. Phys. Lett.* **2001**, *347* (4–6), 318–324.

(228) Bässler, H.; Köhler, A. "Hot or Cold": How Do Charge Transfer States at the Donor–acceptor Interface of an Organic Solar Cell Dissociate? *Phys. Chem. Chem. Phys.* **2015**, *17* (43), 28451–28462.

(229) Athanasopoulos, S.; Tscheuschner, S.; Bässler, H.; Köhler, A. Efficient Charge Separation of Cold Charge-Transfer States in Organic Solar Cells Through Incoherent Hopping. *J. Phys. Chem. Lett.* **2017**, *8* (9), 2093–2098.

(230) Vandewal, K.; Albrecht, S.; Hoke, E. T.; Graham, K. R.; Widmer, J.; Douglas, J. D.; Schubert, M.; Mateker, W. R.; Bloking, J. T.; Burkhard, G. F.; et al. Efficient Charge Generation by Relaxed Charge-Transfer States at Organic Interfaces. *Nat. Mater.* **2014**, *13* (1), 63–68.

(231) Vandewal, K.; Gadisa, A.; Oosterbaan, W. D.; Bertho, S.; Banishoeib, F.; Van Severen, I.; Lutsen, L.; Cleij, T. J.; Vanderzande, D.; Manca, J. V. The Relation Between Open-Circuit Voltage and the Onset of Photocurrent Generation by Charge-Transfer Absorption in Polymer : Fullerene Bulk Heterojunction Solar Cells. *Adv. Funct. Mater.* **2008**, *18* (14), 2064–2070.

(232) Bakulin, A. A.; Rao, A.; Pavelyev, V. G.; van Loosdrecht, P. H. M.; Pshenichnikov, M. S.; Niedzialek, D.; Cornil, J.; Beljonne, D.; Friend, R. H. The Role of Driving Energy and Delocalized States for Charge Separation in Organic Semiconductors. *Science* **2012**, *335* (6074), 1340–1344.

(233) Shoaee, S.; Clarke, T. M.; Huang, C.; Barlow, S.; Marder, S. R.; Heeney, M.; McCulloch, I.; Durrant, J. R. Acceptor Energy Level Control of Charge Photogeneration in Organic Donor/Acceptor Blends. *J. Am. Chem. Soc.* **2010**, *132* (37), 12919–12926.

(234) Etzold, F.; Howard, I. A.; Mauer, R.; Meister, M.; Kim, T.-D.; Lee, K.-S.; Baek, N. S.; Laquai, F. Ultrafast Exciton Dissociation Followed by Nongeminate Charge Recombination in PCDTBT:PCBM Photovoltaic Blends. *J. Am. Chem. Soc.* **2011**, *133* (24), 9469–9479.

(235) Li, N.; Perea, J. D.; Kassar, T.; Richter, M.; Heumueller, T.; Matt, G. J.; Hou, Y.; Güldal, N. S.; Chen, H.; Chen, S.; et al. Abnormal Strong Burn-in Degradation of Highly Efficient Polymer Solar Cells Caused by Spinodal Donor-Acceptor Demixing. *Nat. Commun.* **2017**, *8*, 14541.

(236) Kim, Y. H.; Sachse, C.; Machala, M. L.; May, C.; Müller-Meskamp, L.; Leo, K. Highly Conductive PEDOT:PSS Electrode with Optimized Solvent and Thermal Post-Treatment for ITO-Free Organic Solar Cells. *Adv. Funct. Mater.* **2011**, *21* (6), 1076–1081.

(237) Groenendaal, L.; Jonas, F.; Freitag, D.; Pielartzik, H.; Reynolds, J. R. Poly(3,4-Ethylenedioxythiophene) and Its Derivatives: Past, Present, and Future. *Adv. Mater.* **2000**, *12* (7), 481–494.

(238) Huang, J.; Miller, P. F.; Wilson, J. S.; de Mello, A. J.; de Mello, J. C.; Bradley, D. D. C. Investigation of the Effects of Doping and Post-Deposition Treatments on the Conductivity, Morphology, and Work Function of Poly(3,4-Ethylenedioxythiophene)/Poly(Styrene Sulfonate) Films. *Adv. Funct. Mater.* **2005**, *15* (2), 290–296.

(239) Sapkota, S. B.; Fischer, M.; Zimmermann, B.; Würfel, U. Analysis of the Degradation Mechanism of ITO-Free Organic Solar Cells under UV Radiation. *Sol. Energy Mater. Sol. Cells* **2014**, *121*, 43–48.

(240) Elschner, A. The Spectral Sensitivity of PEDOT:PSS Films. *Sol. Energy Mater. Sol. Cells* **2011**, *95* (5), 1333–1338.
(241) Turkovic, V.; Engmann, S.; Tsierkezos, N.; Hoppe, H.; Madsen, M.; Rubahn, H.-G.; Ritter, U.; Gobsch, G. Long-Term Stabilization of Organic Solar Cells Using UV Absorbers. *J. Phys. D. Appl. Phys.* **2016**, *49* (12), 125604.
(242) Jeong, J.; Seo, J.; Nam, S.; Han, H.; Kim, H.; Anthopoulos, T. D.; Bradley, D. D. C.; Kim, Y. Significant Stability Enhancement in High-Efficiency Polymer:Fullerene Bulk Heterojunction Solar Cells by Blocking Ultraviolet Photons from Solar Light. *Adv. Sci.* **2016**, *3* (4), 1500269.
(243) Menelaou, C.; Tierney, S.; Blouin, N.; Mitchell, W.; Tiwana, P.; McKerracher, I.; Jagadish, C.; Carrasco, M.; Herz, L. M. Effect of Nanocrystalline Domains in Photovoltaic Devices with Benzodithiophene-Based Donor–Acceptor Copolymers. *J. Phys. Chem. C* **2014**, *118* (31), 17351–17361.
(244) Hummelen, J. C.; Knight, B. W.; LePeq, F.; Wudl, F.; Yao, J.; Wilkins, C. L. Preparation and Characterization of Fulleroid and Methanofullerene Derivatives. *J. Org. Chem.* **1995**, *60* (3), 532–538.
(245) Yan, C.; Barlow, S.; Wang, Z.; Yan, H.; Jen, A. K.-Y.; Marder, S. R.; Zhan, X. Non-Fullerene Acceptors for Organic Solar Cells. *Nat. Rev. Mater.* **2018**, *3*, 18003.
(246) Gueymard, C. A. Parameterized Transmittance Model for Direct Beam and Circumsolar Spectral Irradiance. *Sol. Energy* **2001**, *71* (5), 325–346.
(247) the International Organization for Standardization. ISO 21348 Definitions of Solar Irradiance Spectral Categories. *Environment* **2007**, No. section 5, 6–7.
(248) Armin, A.; Velusamy, M.; Wolfer, P.; Zhang, Y.; Burn, P. L.; Meredith, P.; Pivrikas, A. Quantum Efficiency of Organic Solar Cells: Electro-Optical Cavity Considerations. *ACS Photonics* **2014**, *1* (3), 173–181.
(249) Cook, S.; Ohkita, H.; Kim, Y.; Benson-Smith, J. J.; Bradley, D. D. C.; Durrant, J. R. A Photophysical Study of PCBM Thin Films. *Chem. Phys. Lett.* **2007**, *445* (4–6), 276–280.
(250) Liu, Q.; Toudert, J.; Liu, F.; Mantilla-Perez, P.; Bajo, M. M.; Russell, T. P.; Martorell, J. Circumventing UV Light Induced Nanomorphology Disorder to Achieve Long Lifetime PTB7-Th:PCBM Based Solar Cells. *Adv. Energy Mater.* **2017**, *7* (21), 1701201.
(251) Schroeder, B. C.; Li, Z.; Brady, M. A.; Faria, G. C.; Ashraf, R. S.; Takacs, C. J.; Cowart, J. S.; Duong, D. T.; Chiu, K. H.; Tan, C.-H.; et al. Enhancing Fullerene-Based Solar Cell Lifetimes by Addition of a Fullerene Dumbbell. *Angew. Chemie Int. Ed.* **2014**, *53* (47), 12870–12875.
(252) Heumueller, T.; Mateker, W. R.; Sachs-Quintana, I. T.; Vandewal, K.; Bartelt, J. A.; Burke, T. M.; Ameri, T.; Brabec, C. J.; McGehee, M. D. Reducing Burn-in Voltage Loss in Polymer Solar Cells by Increasing the Polymer Crystallinity. *Energy Environ. Sci.* **2014**, *7* (9), 2974–2980.
(253) Burlingame, Q.; Tong, X.; Hankett, J.; Slootsky, M.; Chen, Z.; Forrest, S. R. Photochemical Origins of Burn-in Degradation in Small Molecular Weight Organic Photovoltaic Cells.
(254) Voroshazi, E.; Ben Yaala, M.; Uytterhoeven, G.; Tait, J. G.; Andriessen, R. H. A. J. M.; Galagan, Y.; Cheyns, D. Light Stability of ITO-Free Semi-Transparent and Opaque Organic Photovoltaic Devices. In *2015 IEEE 42nd Photovoltaic Specialist Conference (PVSC)*; IEEE, 2015; pp 1–4.
(255) Reese, M. O.; Gevorgyan, S. A.; Jørgensen, M.; Bundgaard, E.; Kurtz, S. R.; Ginley, D. S.; Olson, D. C.; Lloyd, M. T.; Morvillo, P.; Katz, E. A.; et al. Consensus Stability Testing Protocols for Organic Photovoltaic Materials and Devices. *Sol. Energy Mater. Sol. Cells* **2011**, *95* (5), 1253–1267.

(256) Tvingstedt, K.; Vandewal, K.; Gadisa, A.; Zhang, F.; Manca, J.; Inganäs, O. Electroluminescence from Charge Transfer States in Polymer Solar Cells. *J. Am. Chem. Soc.* **2009**, *131* (33), 11819–11824.
(257) Holmes, A. B.; Bradley, D. D. C.; Brown, A. R.; Burn, P. L.; Burroughes, J. H.; Friend, R. H.; Greenham, N. C.; Gymer, R. W.; Halliday, D. A.; Jackson, R. W.; et al. Photoluminescence and Electroluminescence in Conjugated Polymeric Systems. *Synth. Met.* **1993**, *57* (1), 4031–4040.
(258) Friend, R. H.; Gymer, R. W.; Holmes, A. B.; Burroughes, J. H.; Marks, R. N.; Taliani, C.; Bradley, D. D. C.; Santos, D. A. Dos; Brédas, J. L.; Lögdlund, M.; et al. Electroluminescence in Conjugated Polymers. *Nature* **1999**, *397* (6715), 121–128.
(259) Fungura, F.; Lindemann, W. R.; Shinar, J.; Shinar, R. Carbon Dangling Bonds in Photodegraded Polymer:Fullerene Solar Cells. *Adv. Energy Mater.* **2017**, *7* (6), 1601420.
(260) Voroshazi, E.; Cardinaletti, I.; Conard, T.; Rand, B. P. Light-Induced Degradation of Polymer:Fullerene Photovoltaic Devices: An Intrinsic or Material-Dependent Failure Mechanism? *Adv. Energy Mater.* **2014**, *4* (18), 1400848.
(261) Street, R. A.; Davies, D. M. Kinetics of Light Induced Defect Creation in Organic Solar Cells. *Appl. Phys. Lett.* **2013**, *102* (4), 043305.
(262) Street, R. A.; Northrup, J. E.; Krusor, B. S. Radiation Induced Recombination Centers in Organic Solar Cells. *Phys. Rev. B* **2012**, *85* (20), 205211.
(263) Shah, S.; Biswas, R. Atomic Pathways Underlying Light-Induced Changes in Organic Solar Cell Materials. *J. Phys. Chem. C* **2015**, *119* (35), 20265–20271.
(264) Nielsen, C. B.; Holliday, S.; Chen, H.-Y.; Cryer, S. J.; McCulloch, I. Non-Fullerene Electron Acceptors for Use in Organic Solar Cells. *Acc. Chem. Res.* **2015**, *48* (11), 2803–2812.
(265) Lee, H. K. H.; Telford, A. M.; Röhr, J. A.; Wyatt, M. F.; Rice, B.; Wu, J.; de Castro Maciel, A.; Tuladhar, S. M.; Speller, E.; McGettrick, J.; et al. The Role of Fullerenes in the Environmental Stability of Polymer:Fullerene Solar Cells. *Energy Environ. Sci.* **2018**, *11* (2), 417–428.
(266) Hou, J.; Inganäs, O.; Friend, R. H.; Gao, F. Organic Solar Cells Based on Non-Fullerene Acceptors. *Nat. Mater.* **2018**, *17* (2), 119–128.